Opening New Perspectives in Nanotechnology: Symmetry Forbidden Interfaces, Vector Substrates, and Self-assembled Nanocrystals

Dissertation

der Mathematisch-Naturwissenschaftlichen Fakultät

der Eberhard Karls Universität Tübingen

zur Erlangung des Grades eines

Doktors der Naturwissenschaften

(Dr. rer. nat.)

vorgelegt von

Yu-Jung Wu

aus Chiayi, Taiwan

Tübingen

2024

Gedruckt mit Genehmigung der Mathematisch-Naturwissenschaftlichen Fakultät der Eberhard Karls Universität Tübingen.

Tag der mündlichen Qualifikation:	04.02.2025
Dekan:	Prof. Dr. Thilo Stehle
1. Berichterstatter:	Prof. Dr. Dieter Kölle
2. Berichterstatter:	Prof. Dr. Jochen Mannhart
3. Berichterstatter:	Prof. Dr. Hans Hilgenkamp

Dedicated to my family

Contents

Abstract

Oxide materials are widely used in current research due to their exceptional intrinsic properties, such as ferroelectricity, magnetism, and superconductivity. However, the strong bonding between oxide thin films and their rigid substrates limits flexibility, restricting their use in applications needing adaptable materials. In the last decade, advancements in freestanding membrane techniques have enabled the detachment of oxide thin films from their bulk substrates, providing greater flexibility and allowing for enhanced control over their properties. This thesis aims to leverage membrane techniques to bypass the boundaries imposed by epitaxial growth.

In this thesis, first, extensive research has been conducted on the fabrication of membranes from various materials, showing that the success of membrane transfer depends on optimizing deposition conditions, buffer layer thickness, and buffer layer material selection, which are crucial for advancing the technique. In this work, oxide films are grown using pulsed laser deposition (PLD), with the growth monitored in-situ using reflection high-energy electron diffraction (RHEED), and their crystalline structures characterized by X-ray diffraction (XRD).

The study then investigates the weak bonding between $SrTiO_3$ and $LaAlO_3$ membranes and sapphire substrates. By heating the membranes to high temperatures—below their melting points—thermally unstable oxide membranes self-assemble into crystalline nanostructures. Scanning transmission electron microscopy (STEM) analysis confirms that these nanostructures exhibit a highly crystalline nature, with well-defined facets and uniform chemical distribution. This level of quality and precision surpasses what can be achieved through conventional lithography techniques such as e-beam and optical lithography.

The thesis then introduces the concept of the "vector substrate," which overcomes conventional limitations of substrate design. In typical epitaxial growth, only the surface area of the substrate (around 10 nm thick) directly influences the growth, while the bulk substrate provides mundane properties such as mechanical support and thermal stability. In contrast, the vector substrate concept uses an oxide membrane as a template noted as a "vector" for subsequent growth, expanding the possible choice of substrates. This is achieved by transferring oxide membranes from reusable substrates onto substrates of choice. This approach is especially useful when conventional substrates are expensive or hard to get, for example, bicrystal substrates. The feasibility of this technique is demonstrated in this thesis by successfully fabricating Josephson junctions on bicrystal vector substrate, created by transferring bicrystalline $SrTiO_3$ membranes on sapphire substrates.

A major challenge in traditional epitaxy is the requirement for structural symmetry and lattice constant matching between the film and substrate, which severely limits material combinations. This challenge is also overcome by utilizing membrane techniques and post-transfer treatments. This work achieves atomically clean interfaces between threefold symmetric sapphire and fourfold symmetric $SrTiO_3$, which is epitaxially forbidden, featuring a novel moiré-type reconstruction. This paves the way for the creation of novel heterostructures. These studies overcome the limitations of traditional epitaxy by utilizing membrane techniques, unlocking new possibilities for material growth and expanding their practical applications. The thesis concludes with a discussion of future directions and potential applications of these innovative approaches.

Zusammenfassung

Oxidmaterialien werden aufgrund ihrer außergewöhnlichen intrinsischen Eigenschaften, wie Ferroelektrizität, Magnetismus und Supraleitfähigkeit, in der aktuellen Forschung häufig verwendet. Allerdings schränkt die starke Bindung zwischen Oxiddünnfilmen und starren Substraten die Flexibilität ein, was ihre Verwendung in Anwendungen, die anpassungsfähige Materialien erfordern, begrenzt. Im letzten Jahrzehnt haben Fortschritte in der Technik der freistehenden Membranen das Ablösen von Oxiddünnfilmen von ihren Substraten ermöglicht, was eine größere Flexibilität und eine verbesserte Kontrolle über ihre Eigenschaften bietet. Ziel dieser Arbeit ist es, Membrantechniken zu nutzen, um die durch epitaktisches Wachstum auferlegten Grenzen zu überwinden.

In dieser Arbeit wurde zunächst umfassend die Herstellung von Membranen aus verschiedenen Materialien erforscht, wobei gezeigt wurde, dass der Erfolg des Membrantransfers von der Optimierung der Abscheidungsbedingungen, der Dicke der Pufferschicht und der Auswahl des Pufferschichtmaterials abhängt, die für die Weiterentwicklung der Technik entscheidend sind. In dieser Arbeit werden Oxidfilme mittels pulsed laser deposition (PLD) hergestellt, wobei das Wachstum in-situ mittels reflection high-energy electron diffraction (RHEED) überwacht und ihre kristallinen Strukturen mittels X-ray diffraction (XRD) charakterisiert werden.

Die Studie untersucht dann die schwache Bindung zwischen $SrTiO_3$- und $LaAlO_3$-Membranen und Saphirsubstraten. Durch Erhitzen der Membranen auf hohe Temperaturen, knapp unterhalb ihrer Schmelzpunkte, ordnen sich thermisch instabile Oxidmembranen zu kristallinen Nanostrukturen selbst. Die Analyse mittels scanning transmission electron microscopy (STEM) bestätigt, dass diese Nanostrukturen eine hohe Kristallinität mit gut definierten Facetten und einer gleichmäßigen chemischen Verteilung aufweisen. Dieses Qualitäts- und Präzisionsniveau übertrifft das, was durch herkömmliche Lithografietechniken wie Elektronenstrahl- und optische Lithografie erreicht werden kann.

Anschließend führt die Arbeit das Konzept des „Vektorsubstrats“ ein, das konventionelle Beschränkungen des Substratdesigns überwindet. Beim typischen epitaktischen Wachstum beeinflusst nur die Oberfläche des Substrats (etwa 10 nm dick) direkt das Wachstum, während das Massesubstrat lediglich mechanische Unterstützung und thermische Stabilität bietet. Im Gegensatz dazu verwendet das Konzept des Vektorsubstrats eine Oxidmembran als Vorlage, die als „Vektor“ für das anschließende Wachstum dient und so die mögliche Auswahl an Substraten erweitert. Dies wird durch den Transfer von Oxidmembranen von wiederverwendbaren Substraten auf Wunschsubstrate erreicht. Dieser Ansatz ist besonders nützlich, wenn herkömmliche Substrate teuer oder schwer zu beschaffen sind, beispielsweise Bikristallsubstrate. Die Machbarkeit dieser Technik wird in dieser Arbeit durch die erfolgreiche Herstellung von Josephson-Kontakten auf einem Bikristall-Vektorsubstrat demonstriert, das durch den Transfer bikristalliner $SrTiO_3$-Membranen auf Saphirsubstrate geschaffen wurde.

Eine große Herausforderung bei der traditionellen Epitaxie ist die Notwendigkeit der strukturellen Symmetrie und des Gitterkonstantenabgleichs zwischen Film und Substrat, was die Materialkombinationen stark einschränkt. Diese Herausforderung wird auch durch die Verwendung von Membrantechniken und Nachbehandlungen nach dem Transfer überwunden. In dieser Arbeit werden atomar saubere Grenzflächen zwischen

dreifach symmetrischem Saphir und vierfach symmetrischem $SrTiO_3$ erreicht, was epitaktisch verboten ist und eine neuartige Moiré Rekonstruktion aufweist. Dies ebnet den Weg für die Schaffung neuartiger Heterostrukturen. Diese Studien überwinden die Einschränkungen der traditionellen Epitaxie durch den Einsatz von Membrantechniken, erschließen neue Möglichkeiten für das Materialwachstum und erweitern deren praktische Anwendungen. Die Arbeit schließt mit einer Diskussion über zukünftige Richtungen und mögliche Anwendungen dieser innovativen Ansätze.

Acknowledgements

This thesis would have been impossible to complete without the invaluable contributions, support, and guidance of many people.

First and foremost, I am deeply grateful to my supervisor, Professor Jochen Mannhart, for his exceptional mentorship throughout my Ph.D. at MPI-FKF. Your profound expertise, encouragement, and pushing me to think beyond conventional boundaries have been instrumental in shaping this journey. I have learned so much from your open-mindedness, genuine passion for research, and all the insightful scientific discussions.

I sincerely thank my supervisor at Tübingen University, Professor Dieter Kölle, and Professor Reinhold Kleiner, for their support and invaluable guidance throughout this journey. I would also like to extend my heartfelt thanks to my external advisor, Professor Reinhard Kremer, for his valuable insights and feedback during our annual meetings.

I am especially grateful to Varun Harbola, from whom I gained invaluable knowledge about membranes and physics. Your insights, commitment to research, and positive attitude have had a profound impact on me, sparking my own enthusiasm for learning and exploration. I deeply appreciate the support you have provided throughout this journey. Working with you has been a truly wonderful experience.

To my group members, especially Sanela Göres, thank you for being an incredibly supportive colleague and friend. You always offer me support not only at work but also in life. I am grateful to Thomas Whittles, Sarah Parks, and Felix Hensling for their help and assistance in the lab, and to Renate Zimmerman for handling administrative matters and offering warm help outside of work. Many thanks to Wolfgang Winter, Ingo Hagel, Sabine Seiffert, and Konrad Lazarus for their support with the PLD facilities and IT issues. I also like to thank to all the other current and former group members. I truly enjoyed being a part of this group.

Many thanks to Martin Hack, Katja Wurster, and Simon Koch for their collaboration on the Josephson junction project. Their expertise and efficiency made our work together a great experience. I am also thankful to Hongguang Wang, Ute Salzberger, and Peter van Aken for their expertise in STEM and the nice cooperation.

I would like to extend special thanks to the EU FLAG-ERA Project To2Dox, led by Professor Jacobo Santamaria, for their support. My sincere gratitude goes as well to Dr. Chengtian Lin for his constant support and care. I am grateful to the Nanostructuring Lab team, especially Thomas Reindl, Ulrike Waizmann, Marion Hagel, and Achim Güth, for their patience, readiness to help, and technical support with the NSL facilities. I also want to thank Helga Hoier for the assistance with XRD measurements.

I would like to thank my friend Yu-Mi for her company and support. You have always been there for me, offering help and encouragement whenever I needed it. The time spent in your company has been truly wonderful. To my friends Gabriele, Vivian, Chun-Chieh, and Uta, thank you for your companionship, support, and encouragement. Your presence has meant so much to me during this journey.

Finally, my deepest gratitude goes to my family for their unconditional support and never-ending love throughout this journey.

Chapter 1

Introduction

Epitaxy has enabled major breakthroughs in both research and practical applications. This progress has fueled innovations in electronics, optoelectronics, and nanotechnology. Despite the successes, epitaxial growth is limited by the need for lattice-matched, high-quality substrates, which are costly and rigid, restricting material choices and applications that require flexibility. The development of membrane techniques, which allow the separation of oxide films from their rigid bulk substrates, has opened up new possibilities for innovative material design and expanded applications. In this study, complex oxides were selected as the material class due to the intricate relationship between the structure and properties of perovskites. This relationship makes perovskites a captivating area of research, offering promising applications in advanced electronics, spintronics, and quantum devices.

1.1 Epitaxy

Film growth techniques using epitaxial growth have been successfully utilized to fabricate crystalline thin films and heterostructures, driving groundbreaking advancements across multiple fields. For instance, it has led to the discovery of the quantum Hall effect[1, 2], high-performance semiconductors[3], blue LEDs[4], and giant magnetoresistance[5], to name just a few. These achievements have had profound impacts on electronics, optoelectronics, and spintronics, driving innovations that have transformed industries and technologies.

However, despite its successes, epitaxial growths face certain limitations. One of the primary limitations is the requirement for lattice matching, which necessitates that the substrate and the deposited material have closely aligned crystal structures. This constraint often limits the choice of materials and can make the process restrictive. Additionally, epitaxy demands high-quality substrates, which are not only expensive but sometimes can also be difficult to acquire, particularly when dealing with large-scale applications or rare materials. Furthermore, the strong bonding between the thin films and the rigid bulk substrates limits the flexibility of the resulting structures, restricting their potential applications, especially in fields that require adaptable materials.

1.2 Complex oxides

To explore the boundary of epitaxy, complex oxides were chosen for this thesis as the material class of study. Transition-metal oxides exhibit an extraordinary range of functionalities, including electrical transport, magnetism, optical response, thermal conductivity, and superconductivity[6]. These diverse properties arise from the strong interplay between their charge, orbital, spin, and structural characteristics, enabling the creation of functional devices with capabilities that surpass those of standard semiconductors.

Perovskite materials, a prominent class of transition-metal oxides, are particularly noteworthy for their versatility. These materials have a general formula of ABO_3 and feature a distinctive crystal structure where the B-site cation, typically a transition metal, is surrounded by an octahedron of oxygen atoms. The A-site cation occupies the corners of the cubic unit cell (Figure 1.1). Distortion of oxygen octahedra can significantly alter the material's properties, offering a tunable parameter space for exploring various physical phenomena. External perturbations, such as pressure, strain, and temperature, can modify the relative positions of the transition metal and oxygen ions, influencing the interactions between electrons and spins. These changes can drive the material into new ground states, resulting in phenomena such as the Mott transition, where the material transitions from an insulator to a metal, governed by factors like the electron hopping rate and d-band filling[7].

Perovskites, e.g. $SrTiO_3$ and $LaAlO_3$, show fascinating intrinsic properties. At room temperature, $SrTiO_3$ exhibits a cubic perovskite structure($Pm\bar{3}m$) with a 3.905 Å lattice parameter, which transitions to a tetragonal phase at 105 K due to a rotation of the oxygen octahedra. It is an insulator with a 3.2 eV band gap, while doping with oxygen vacancies induces semiconducting properties and magnetic behavior, ranging from paramagnetic to ferromagnetic depending on vacancy concentration. $SrTiO_3$ also becomes superconducting when doped with Nb, La, or oxygen vacancies, with transition temperatures typically below 0.4 K. Moreover, its dielectric constant is remarkably high, varying from 300 at room temperature to ∼20000 at 4 K.

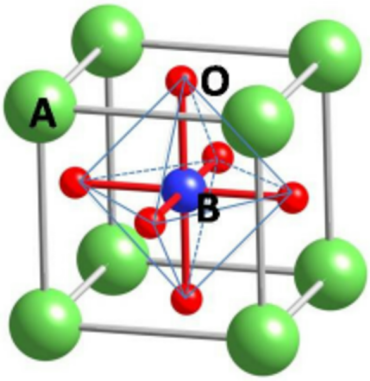

Figure 1.1: The general structure of perovskite oxides. Reproduced under terms of the CC-BY license.[12]

At room temperature, $LaAlO_3$ has a lattice parameter of 3.790 Åand shows a rhombohedral structure, with a transition to a cubic structure above 813 K. Its high dielectric constant of 25, and wide bandgap of 5.6 eV make it attractive as a gate dielectric[8].

Additionally, the heterointerfaces of oxides, where lattice symmetry is broken, give rise to emergent phenomena that do not exist in the bulk materials, owing to the reconstructions of charge, orbital and spin at the interfaces (Figure 1.2). These interfaces can host novel electronic and magnetic states, offering exciting opportunities for discovering and engineering new functionalities[9]. One of the most famous discoveries is the interface between the insulating $SrTiO_3$ and $LaAlO_3$ showing superconductivity, signature magnetism, and formation a two-dimensional electron gas[10, 11]. These properties have made complex oxide materials a crucial role in the development of advanced materials and electronic technologies.

1.3 Freestanding oxide membranes

Due to the strong epitaxial bonding between oxide films and their substrates, bending oxide films or separating them from their rigid bulk is challenging. However, the development of freestanding oxide membranes has recently overcome this obstacle, allowing oxide films to be separated from their substrates, thereby eliminating substrate effects on film properties(see Figure 1.3). Once detached, these membranes can be stacked and manipulated like 2D materials[14], offering great flexibility in material engineering. Additionally, this technique enables strain and texture engineering on the membranes[15, 16], breaking the constraints imposed by traditional epitaxy.

Several techniques are available for obtaining oxide membranes, such as wet etching[18], mechanical exfoliation[19], and spalling[20]. A common method involves using a water-soluble buffer layer, often $Sr_3Al_2O_6$[18, 21], due to its easy dissolution in water and structural compatibility with $SrTiO_3$. $Sr_3Al_2O_6$ forms a cubic unit cell with a lattice constant of 15.844 Å, closely matching four unit cells of $SrTiO_3$ (a_{STO}= 3.905 Å, 4× a_{STO} =15.620 Å). $Sr_3Al_2O_6$ has distinct ring structures, unlike typical aluminates that form long chains, making it dissolvable in water[18]. To do so, a water soluble $Sr_3Al_2O_6$ buffer layer is first deposited on a $SrTiO_3$ substrate, followed by the growth of the oxide membrane (Figure 1.4). By selectively etching the buffer layer with water, the oxide

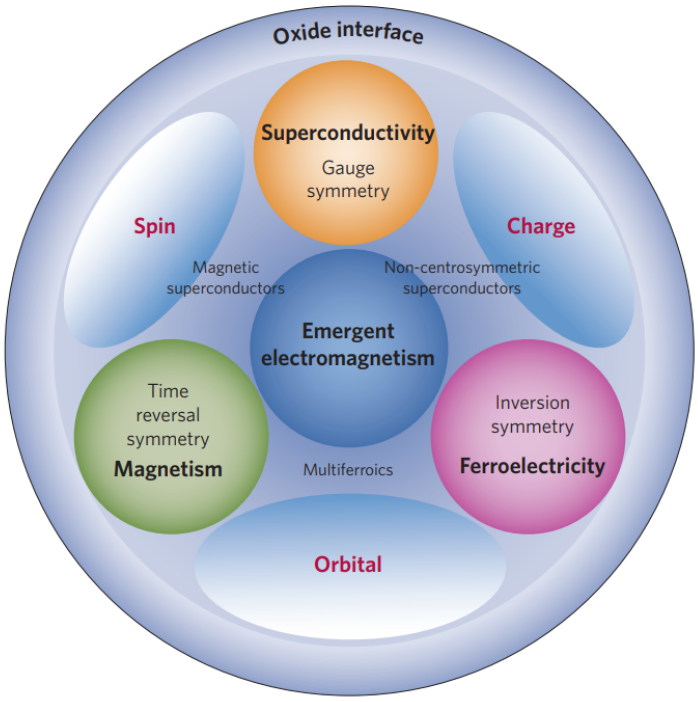

Figure 1.2: Schematic illustrating the symmetries and tunable degrees of freedom of interfaces between complex oxides. Reproduced with permission.[13] Copyright 2012, Springer Nature.

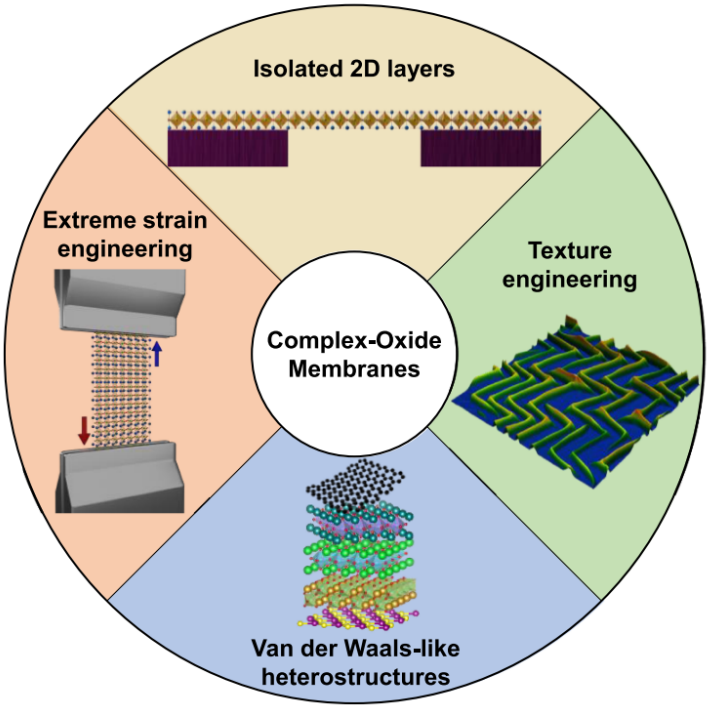

Figure 1.3: Schematic illustrating membrane technique to enable flexibility in material engineering. Reproduced under terms of the CC-BY license.[17]

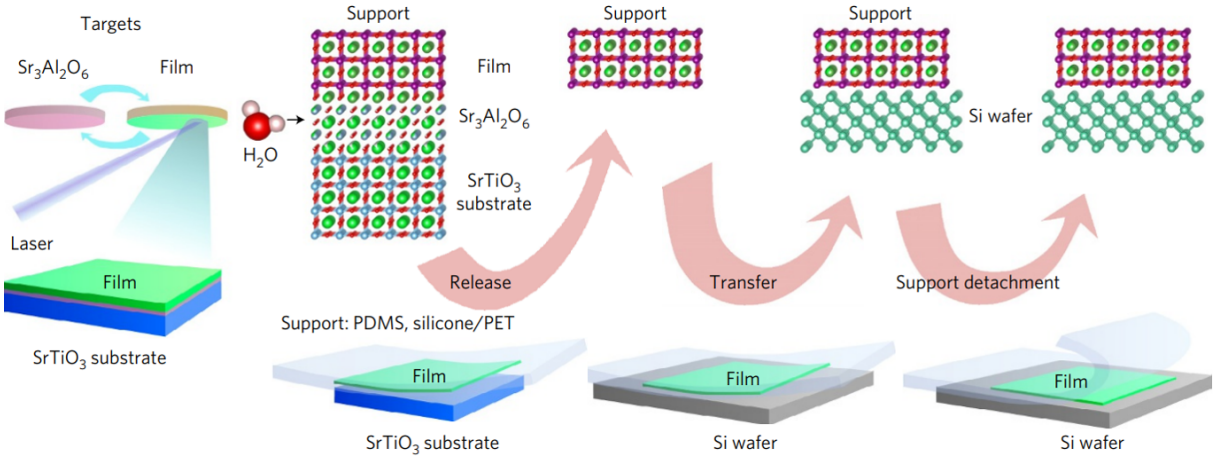

Figure 1.4: Schematic of the fabrication process of oxide membranes. Reproduced with permission.[18] Copyright 2016, Springer Nature.

membrane can be lifted off, resulting in a freestanding membrane which then can be transferred onto a system of choice.

To grow membranes of different lattice constants, substrates and buffer layers with matching lattice constants are needed. Fortunately, the lattice constant of $Sr_3Al_2O_6$ buffer layer can be adjusted by substituting Sr with Ba or Ca, thereby enlarging or decreasing its lattice constant as needed[22]. Other buffers, like $SrRuO_3$[23, 24] and $La_{0.67}Sr_{0.33}MnO_3$[25, 26], are also available and can dissolve in chemical solvents. The range of the buffer layer lattice constants is approaching those of single crystalline substrates[27, 28], providing more options for fabricating membranes with diverse lattice constants. (Figure 1.5).

The flexibility of the membranes enables them to be transferred onto stretchable polymer substrates, facilitating the application of strain and texture engineering, with strain levels reaching up to 10.1%[29], far surpassing the 0.1% typically achievable on bulk substrates. Such strain can dramatically alter the properties of these materials. For instance, $SrTiO_3$ membranes under 2% uniaxial strain have been found to stabilize ferroelectricity at room temperature[15]. Similarly, the resistivity of $La_{0.7}Ca_{0.3}MnO_3$ membranes is strain-tunable with applied biaxial strain up to 5% since the strain effectively suppresses electron hopping between manganese sites[30].

Researchers are also investigating the elastic limits of these membranes and the microstructural arrangements that enable their remarkable elasticity[31], which is unattainable in traditional oxide films. This technique also facilitates the heterointegration of devices[19] by providing the freedom to transfer membranes onto various platforms, including flexible substrates or entirely different materials.

Starting with epitaxial growth, this method retains the advantages of epitaxy—such as precise control over membrane thickness, uniformity, and highly crystalline structures—while simultaneously providing high flexibility.

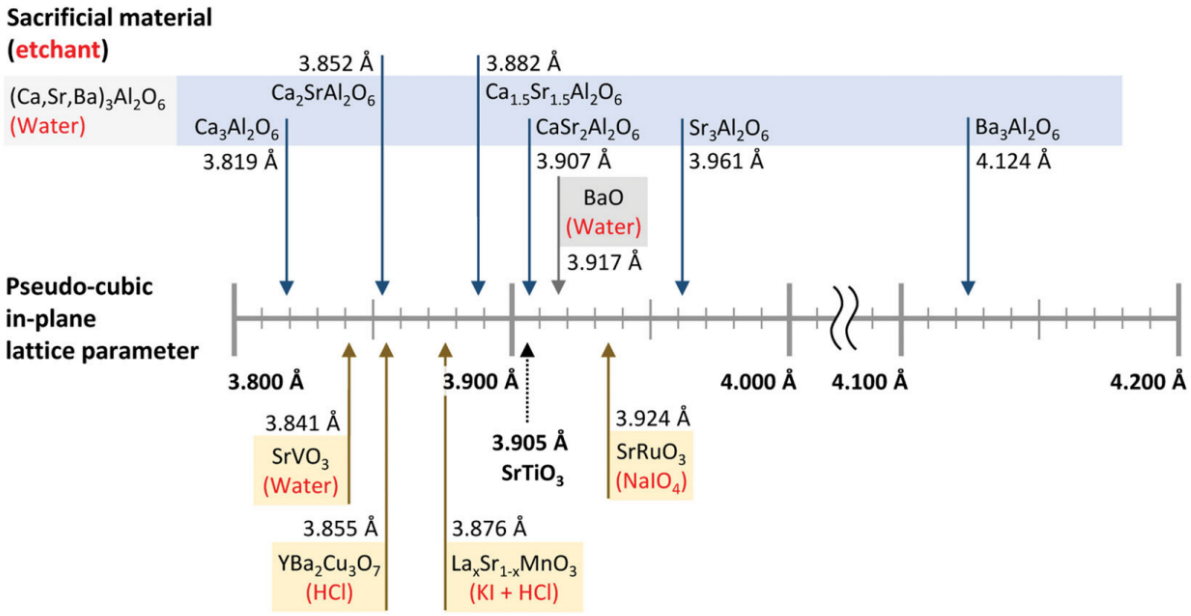

Figure 1.5: Buffer layer materials with varied lattice constants. Reproduced with permission.[28] Copyright 2022, John Wiley and Sons.

1.4 Thesis outline

This thesis attempts to overcome the boundaries of epitaxy by leveraging membrane techniques and thereby put the obtained possibilities in good use. The main work performed is presented in chapter 4 to 7. In chapter 4, the study examines the fabrication of nanocrystals through the self-assembly of oxide membranes. This approach takes advantage of the weak bonding between oxide membranes and sapphire substrates, allowing the membranes to maintain a degree of freedom. When subjected to high-temperature thermal processing, these thermally unstable membranes undergo dewetting, transforming into nanostructures while preserving the crystalline structures of the original membranes.

In chapter 5 and 6, my thesis work pushes the limits of substrate flexibility by utilizing membranes transferred onto various carriers. These membranes act as templates for epitaxial growth, allowing for greater versatility in carrier selection. This flexibility in choosing different materials and shapes for the carriers, combined with the adaptable nature of the membranes, significantly broadens the possibilities for substrate design. As a result, it becomes feasible to create customized or costly substrates, such as bicrystal substrate, using thin-film growth techniques.

Finally, chapter 7 addresses the challenges of creating interfaces between asymmetrical crystal structures. By employing membrane techniques and appropriate post-treatment processes, it is possible to achieve sharp interfaces and bonding between two materials for which their lattice symmetries forbids interface formation by epitaxial growth. This work demonstrates how membrane technique can redefine the possibilities in epitaxy, enabling the creation of novel design and structures that were previously unattainable.

Chapter 2

Standard experimental techniques used

This chapter provides a concise overview of the standard techniques used in the thesis. Pulsed laser deposition (PLD) is used as the method for thin film deposition. During the deposition process, reflection high-energy electron diffraction (RHEED) is utilized to monitor surface structure and verify layer-by-layer growth. Post-deposition, X-ray diffraction (XRD) is conducted to assess the crystalline structure of the samples.

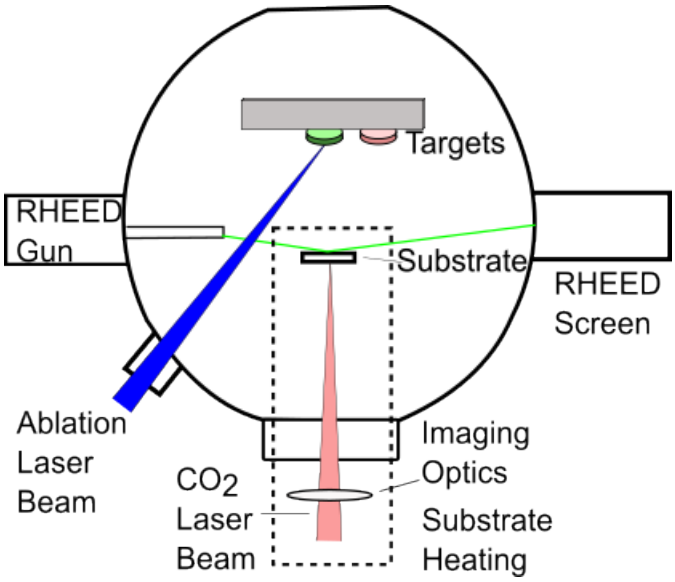

Figure 2.1: Schematic of the PLD system used for thin film growth. A CO_2 heats the back side of the substrate to the desired temperature. An ablation laser vaporizes materials from the targets. The growth process is monitored *in situ* using reflection high-energy electron diffraction.

2.1 Pulsed laser deposition

Pulsed laser deposition (PLD) is a physical vapor deposition technique in which material is removed from a source target by ablating it with an intense UV laser pulse. The laser pulses are fed through a mask which is imaged onto the target to achieve the necessary energy density. Upon absorbing the UV light, the target material ablates, creating a plasma from the evaporated species. This plasma expands from the target toward the substrate, where the ablated material adsorbs and undergoes thermally activated diffusion before forming a thin film layer.

Key parameters influencing the PLD process include substrate temperature, the type and pressure of gas, the energy density of the laser beam on the target, and the laser pulse repetition rate.

Figure 2.1 illustrates a PLD growth system. The substrate is mounted on a metal holder and secured with clamps before being placed on a substrate stage in the PLD chamber, which is maintained at ultra-high vacuum (10^{-9} torr). The substrate is heated to the desired temperature using a CO_2 laser applied to its backside. During deposition, the target material is ablated by a KrF excimer laser with a wavelength of 248 nm, and the target-to-substrate distance is set to 56 mm. To achieve a uniform, droplet free deposition and to optimize the use of the target, it is laterally shifted along a predefined path after each laser pulse. The substrate temperature is measured from the substrate stage with a pyrometer and controlled via a feedback loop. The chamber pressure is regulated by adjusting the gas flow and the pumping speed through a variable shutter placed in front of the turbo pump.

2.2 Reflection high-energy electron diffraction

During deposition, the growth process is monitored *in situ* using reflection high-energy electron diffraction (RHEED), enabling precise control of film thickness down to a single

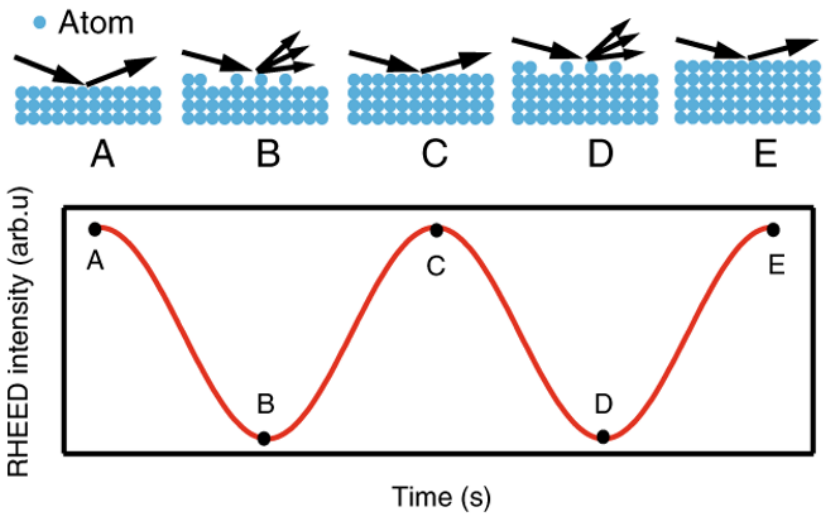

Figure 2.2: Schematic illustrating layer-by-layer growth and the corresponding variation in RHEED intensity. Reproduced under terms of the CC-BY license.[32]

unit cell. RHEED is exceptionally sensitive to surface features, where electrons with a kinetic energy of 30 kV are directed at the sample surface at grazing angles, penetrating only the top few atomic layers. The diffracted electrons arising from the interaction of the electron beam with the atomic arrangement at the sample's surface produce a pattern on a fluorescent screen, revealing the surface structure.

Figure 2.2 shows a typical variation in RHEED intensity during deposition. At the start, the RHEED intensity is at a maximum, but as material is ablated and deposited on the substrate resulting in an increase of surface roughness, the intensity decreases. Once the deposited material reaches a thickness corresponding to a single lattice spacing, the RHEED intensity recovers, and this cycle repeats, corresponding to layer-by-layer growth.

Such oscillations in RHEED intensity indicate a good layer-by-layer growth, which usually yields a smooth surface on the sample. If the growth mode shifts to 3D, where small crystallites form on the surface, the RHEED pattern changes from distinctive spots or streaks to arrays of spots, indicating diffraction through the crystallites and a loss of surface smoothness.

2.3 X-ray diffraction

For a crystalline material with a regular array of atoms, X-ray diffraction is a powerful tool for determining its crystal structure, orientation, and lattice parameters. In this thesis, X-ray diffraction data were obtained using a monochromatic Cu-Kα1 source on a Panalytical Empyrean machine.

X-rays generated by a source illuminate the sample, and the sample diffracts the X-rays elastically. Constructive interference occurs at specific angles, determined by the electron density distribution based on the crystal structure. Measuring the diffracted intensity while scanning the angles between the beam and the sample and/ or between the sample and the detector, allowing the recording of diffraction data.

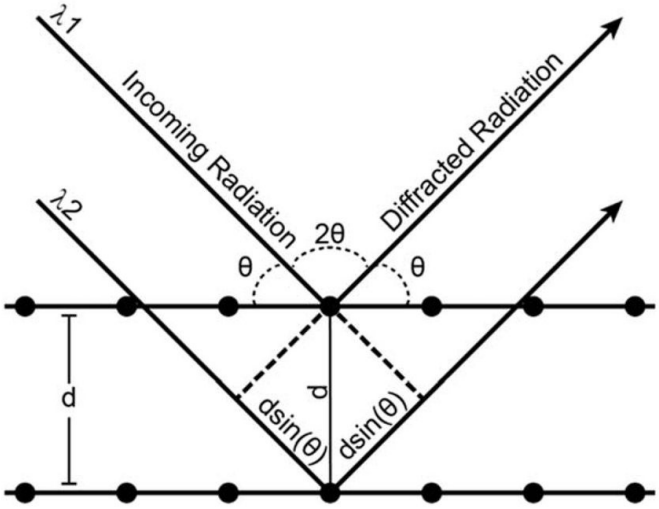

Figure 2.3: Schematic of diffracted radiation. Bragg's condition occurs when the path difference between the diffracted rays ($2d\sin(\theta)$) equals to integer times of the wavelength ($n\lambda$). Reproduced under terms of the CC-BY license.[33]

In symmetric X-ray scans, out-of-plane diffraction can be understood as X-rays scattering off parallel crystal planes. Constructive interference occurs when the well-known Bragg's law is satisfied, which is given by the equation

$$2d\sin(\theta) = n\lambda \tag{2.1}$$

where d represents the inter-planar spacing in the lattice, θ is the the angle of the incident beam relative to the crystal lattice plane, n is the order of the observed diffraction peak, and λ is the wavelength of the X-ray used for diffraction (Figure 2.3).

Chapter 3

Fabrication of freestanding oxide membranes

Fabrication of oxide membranes involves multiple steps—deposition, dissolution, lift-off, and transfer—all detailed in this chapter. Due to the fragile nature of these membranes, optimizing deposition parameters and carefully selecting materials are crucial for a successful transfer.

3.1 Deposition

Before any growth, $SrTiO_3$ substrates were pre-annealed in-situ in an oxygen atmosphere ($P(O_2) = 0.1$ mbar) at 825°C for 40 minutes using a CO_2 laser, resulting in a smooth, step-terrace surface. Films were then deposited using pulsed laser deposition (PLD) with a 248 nm wavelength excimer laser. Initially, a sacrificial layer was deposited, followed by a top membrane. The optimized deposition parameters of different materials are detailed in Table 3.1.

Let us consider, for instance, the commonly used $SrTiO_3$ membranes discussed in this chapter. The growth process of a water-soluble $Sr_2CaAl_2O_6$ buffer layer and a $SrTiO_3$ top layer on a $SrTiO_3$ substrate was monitored by Reflection High-Energy Electron Diffraction (RHEED), as shown in Figure 3.1. The RHEED oscillations confirm the layer-by-layer growth of both $Sr_2CaAl_2O_6$ and $SrTiO_3$, with the inset images displaying 2D patterns indicative of smooth surfaces post-growth. Additionally, Atomic Force Microscopy (AFM) imaging revealed that the sample's surface has a smooth, step-terrace morphology (see Figure 3.2).

Table 3.1: Optimized deposition parameters for the materials used in this thesis.

Material	lattice constant	laser fluence	laser spot size on target	substrate temepra-ture	$P(O_2)$
unit	Å	Jcm^{-2}	mm^2	°C	mbar
$LaAlO_3$	3.792	1.4	2.82	630	$1x10^{-3}$
$YBa_2Cu_3O_{7-x}$	3.855	2.0	2.82	720	0.25
$La_{0.67}Sr_{0.33}MnO_3$	3.876	2.42	4.15	700	0.1
$SrTiO_3$	3.905	1.21	2.82	825	$1x10^{-5}$
$Sr_2CaAl_2O_6$	3.907	1.76	4.15	825	$1x10^{-5}$
$SrRuO_3$	3.924	2.3	2.82	700	$8.6x10^{-2}$
$Sr_3Al_2O_6$	3.961	1.76	4.15	825	$1x10^{-5}$

Note: The deposition of $YBa_2Cu_3O_{7-x}$ was followed by post-annealing at 450°C and $P(O_2)$= 450 mbar for 1 hr.

3.2 Dissolving, lift-off, and transfer

After film deposition, ≈ 600-nm-thick PMMA layers were spin-coated onto the $SrTiO_3$-$Sr_2CaAl_2O_6$-$SrTiO_3$ stacks. The stacks were then immersed in room-temperature deionized water to dissolve the $Sr_2CaAl_2O_6$ sacrificial layers. After 1 to 3 days, the $Sr_2CaAl_2O_6$ layers were selectively etched away by the water, releasing the top membranes coated with PMMA. These released membranes, supported by the PMMA layers, were gently lifted onto the water's surface using tweezers, allowing them to float (Figure 3.3).

The freestanding membranes were then manually transferred onto, for example, Al_2O_3 substrates, which are the most frequently used carriers in this thesis. Any residual water between the membrane and the substrate was removed by heating the assembly to 80°C on a hot plate. The Al_2O_3 substrates had been pre-annealed at 1615°C in a vacuum to create smooth, well-defined step-terrace surfaces. After the membranes were transferred, the PMMA layers were dissolved with acetone, leaving the membranes securely on the Al_2O_3 substrates.

Other materials of membranes were also studied. Optical images demonstrate the successful transfer of $SrTiO_3$, $LaAlO_3$, and $SrRuO_3$ membranes onto sapphire substrates

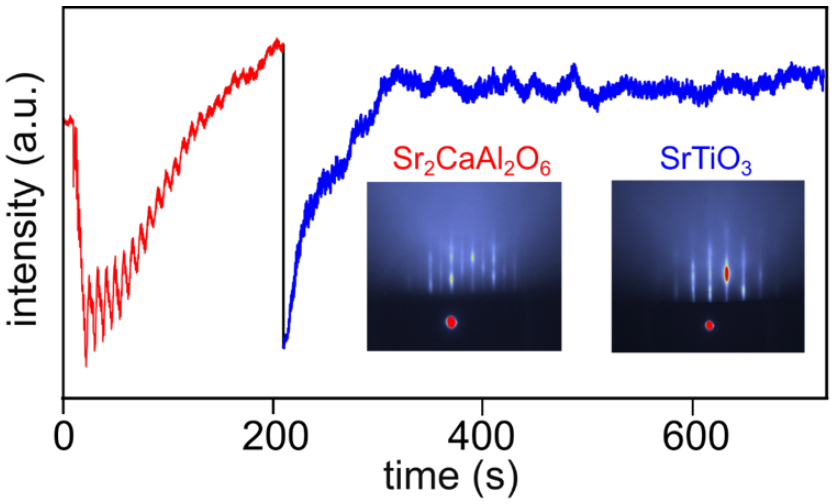

Figure 3.1: RHEED signal of the growth of a 10-nm-thick $Sr_2CaAl_2O_6$ buffer layer and a 16-nm-thick $SrTiO_3$ top layer on a $SrTiO_3$ substrate. Insets: RHEED images taken after the growth of the $Sr_2CaAl_2O_6$ and $SrTiO_3$ layers along the [100] axis of $SrTiO_3$. Reproduced with permission.[34] Copyright 2023, John Wiley and Sons.

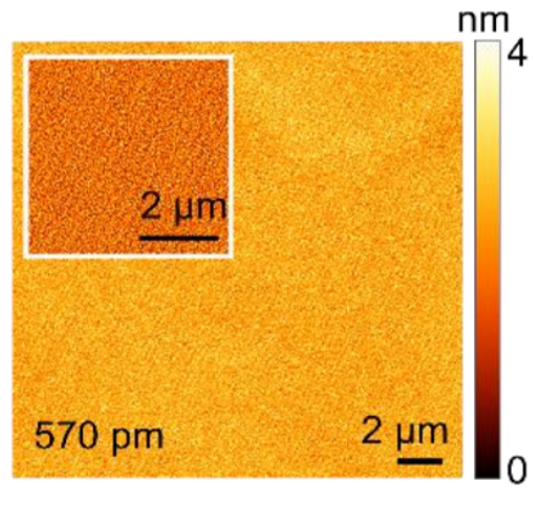

Figure 3.2: AFM images taken after a 10-nm-thick $Sr_2CaAl_2O_6$ buffer layer and a 16-nm-thick $SrTiO_3$ top layer were deposited onto a $SrTiO_3$ substrate. The rms roughness of the surface is 570 pm. Reproduced with permission.[34] Copyright 2023, John Wiley and Sons.

(Figure 3.4). AFM imaging of the transferred membranes confirmed that at a micron scale, the membranes were effectively stacked onto the sapphire carriers, with the underlying step-terrace features of the sapphire substrates remaining visible after stacking. XRD scans indicated that the membranes retained the crystalline structures of their bulk counterparts after lift-off. However, the $SrRuO_3$ membranes exhibited an increased lattice constant, likely due to the use of a reducing etchant during the lift-off process.

3.3 Buffer layer selection

Selecting an appropriate buffer layer was found to be crucial during membrane fabrication. A $La_{0.67}Sr_{0.33}MnO_3/SrTiO_3$ bilayer film with a $Sr_3Al_2O_6$ buffer layer allowed only for small transfer areas (after lift-off, while films with $Sr_2CaAl_2O_6$ buffer layers showed a significantly larger transfer area of approximately 2.5 x 5 mm^2 (Figure 3.5). This difference is likely due to interdiffusion between the $La_{0.67}Sr_{0.33}MnO_3/SrTiO_3$ bilayer and the $Sr_3Al_2O_6$ buffer layer, attributed to the latter's much larger lattice constant.

$LaAlO_3$ films grown on $La_{0.67}Sr_{0.33}MnO_3$ buffer layers cannot be lifted-off, while $LaAlO_3$ films grown on $Sr_2CaAl_2O_6$ buffer layers yield a large-area transfer of approximately 2.5 x 5 mm^2 (Figure 3.4).

Conversely, $SrRuO_3$ films which grown on $Sr_2CaAl_2O_6$ buffer layers cannot be lifted-off, whereas such films on $La_{0.67}Sr_{0.33}MnO_3$ buffer layers achieved a high-quality, large-area transfer of around 2.5 x 5 mm^2 (Figure 3.4). To selectively dissolve the $La_{0.67}Sr_{0.33}MnO_3$ buffer layer, a reducing etchant, specifically a mixture of KI and HCl, is necessary, completing the lift-off process in less than one day. Table 3.2 compares the advantages and disadvantages of the three buffer layers used in this thesis.

Table 3.2: The advantages and disadvantages of using $Sr_3Al_2O_6$, $Sr_2CaAl_2O_6$ and $La_{0.67}Sr_{0.33}MnO_3$ as buffer layers

buffer layer material	advantages	disadvantages
$Sr_3Al_2O_6$	water soluble widely used	1.43% lattice mismatch with $SrTiO_3$ interdiffusion of top layers
$Sr_2CaAl_2O_6$	water soluble 0.05% lattice mismatch with $SrTiO_3$	interdiffusion of top layers
$La_{0.67}Sr_{0.33}MnO_3$	perovskite small lattice constant quick lift-off	reducing etchant required selective chemical etchant required

3.4 Optimization of large-area transfer

To achieve a large-area transfer of $SrTiO_3$ membranes, the fabrication process was systematically optimized, focusing on factors such as film thickness and buffer layer materials. Initially, a 32-nm-thick $Sr_2CaAl_2O_6$ buffer layer was deposited on a $SrTiO_3$ substrate, followed by a 20-nm-thick $SrTiO_3$ top layer. However, the $SrTiO_3$ membranes transferred onto sapphire carriers exhibited numerous cracks, resulting in only small intact areas (μm^2). This issue is likely caused by the uneven dissolution of the thick $Sr_2CaAl_2O_6$ buffer layers. In contrast, if thinner 8-nm-thick $Sr_2CaAl_2O_6$ buffer layers were used beneath 14-nm-thick $SrTiO_3$ top layers, the transfer quality significantly improved, yielding intact areas of approximately 1 x 1 mm^2 (see Figure 3.6).

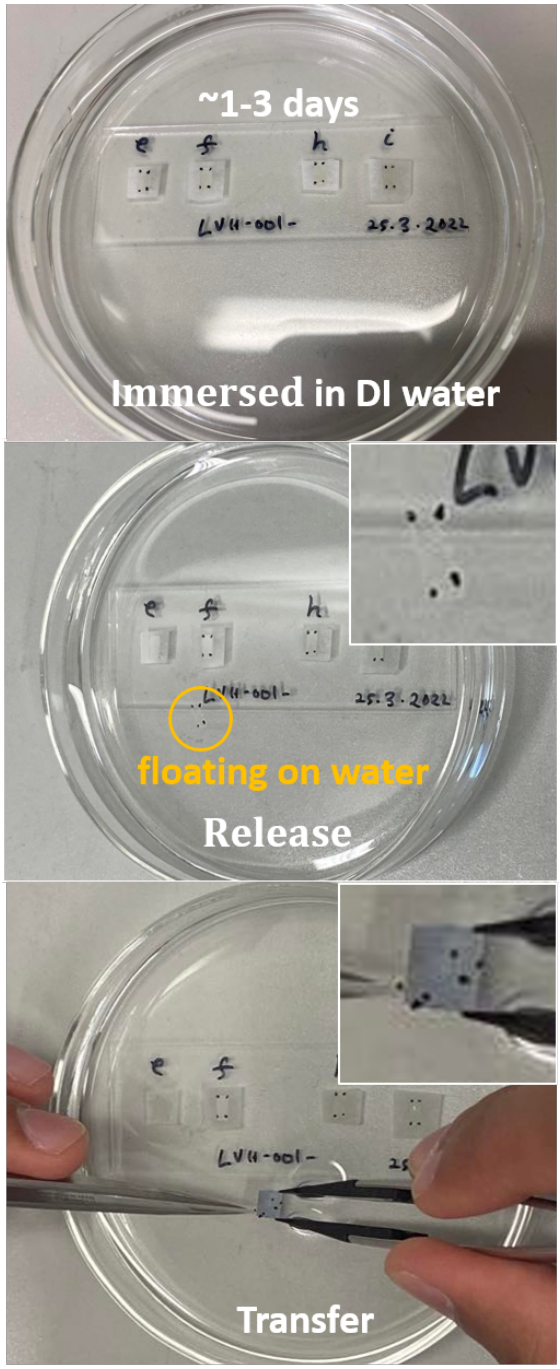

Figure 3.3: Photographs of the transfer process. The upper membrane was lifted off and made to float on water once the buffer layer was selectively dissolved. The membrane was then transferred onto a new carrier. The insets show zoom-in images.

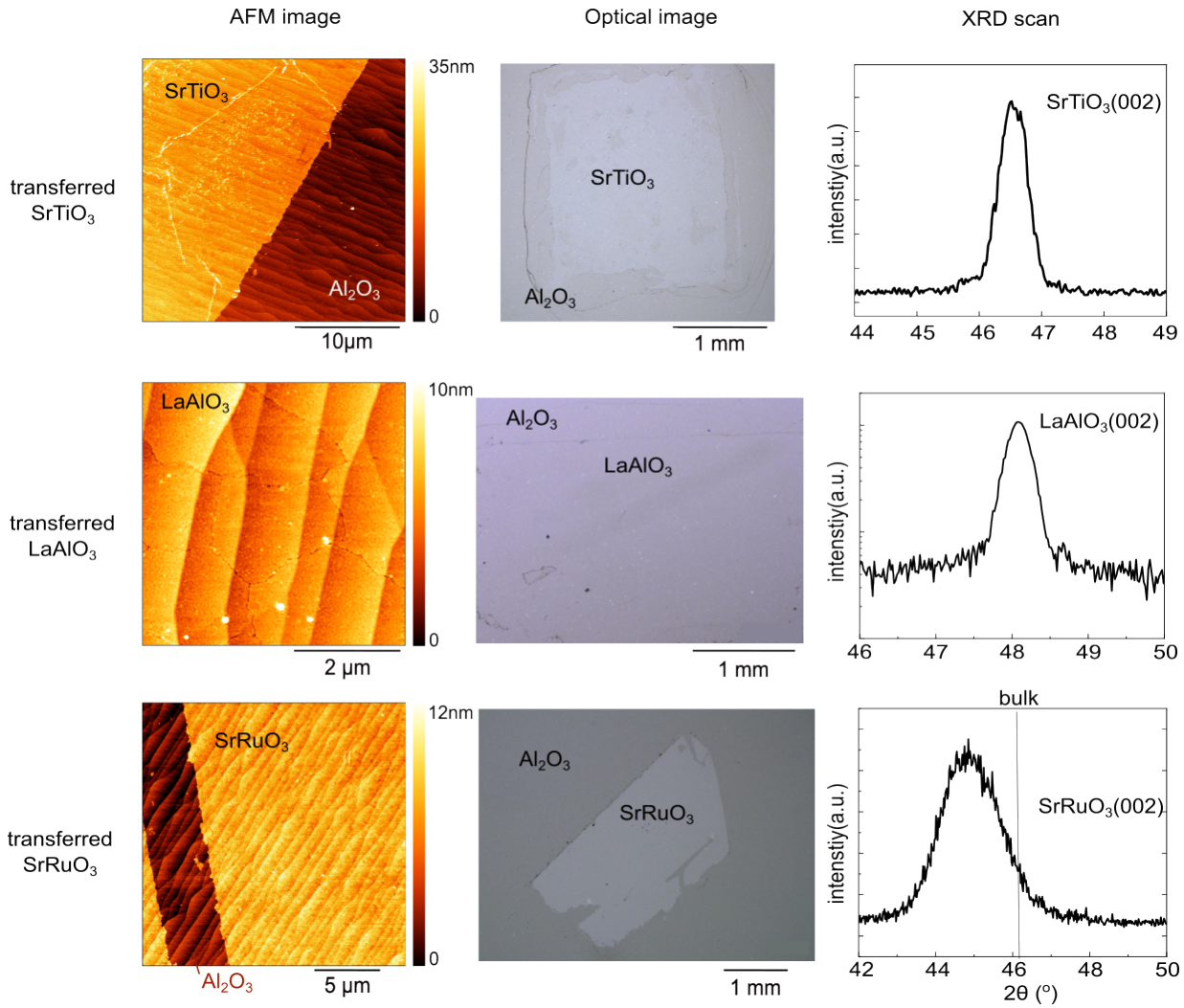

Figure 3.4: AFM images, optical images, and XRD scans of transferred $SrTiO_3$, $LaAlO_3$, and $SrRuO_3$ membranes on sapphire substrates.

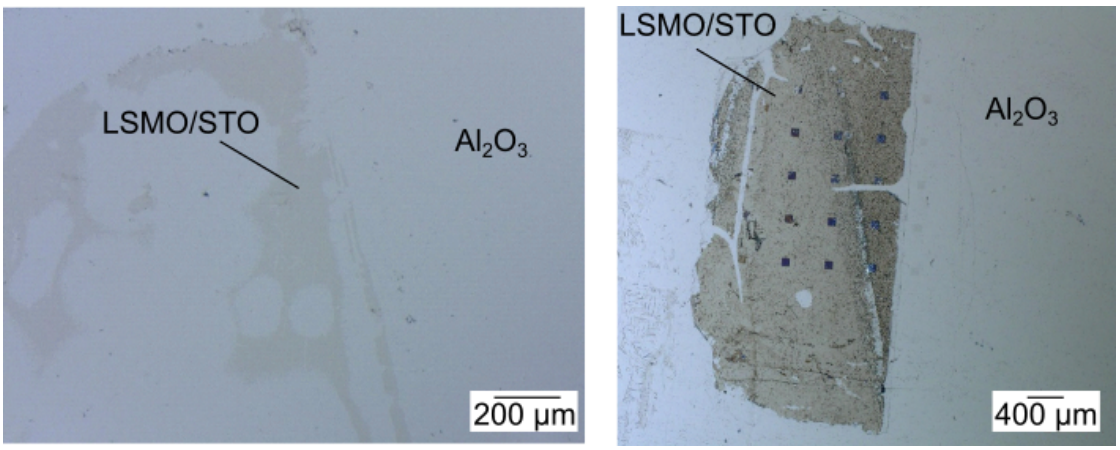

Figure 3.5: Optical images of $La_{0.67}Sr_{0.33}MnO_3$/ $SrTiO_3$ bilayer membranes transferred on sapphire substrates, with the use of $Sr_3Al_2O_6$ (left) and $Sr_2CaAl_2O_6$ (right) buffer layers.

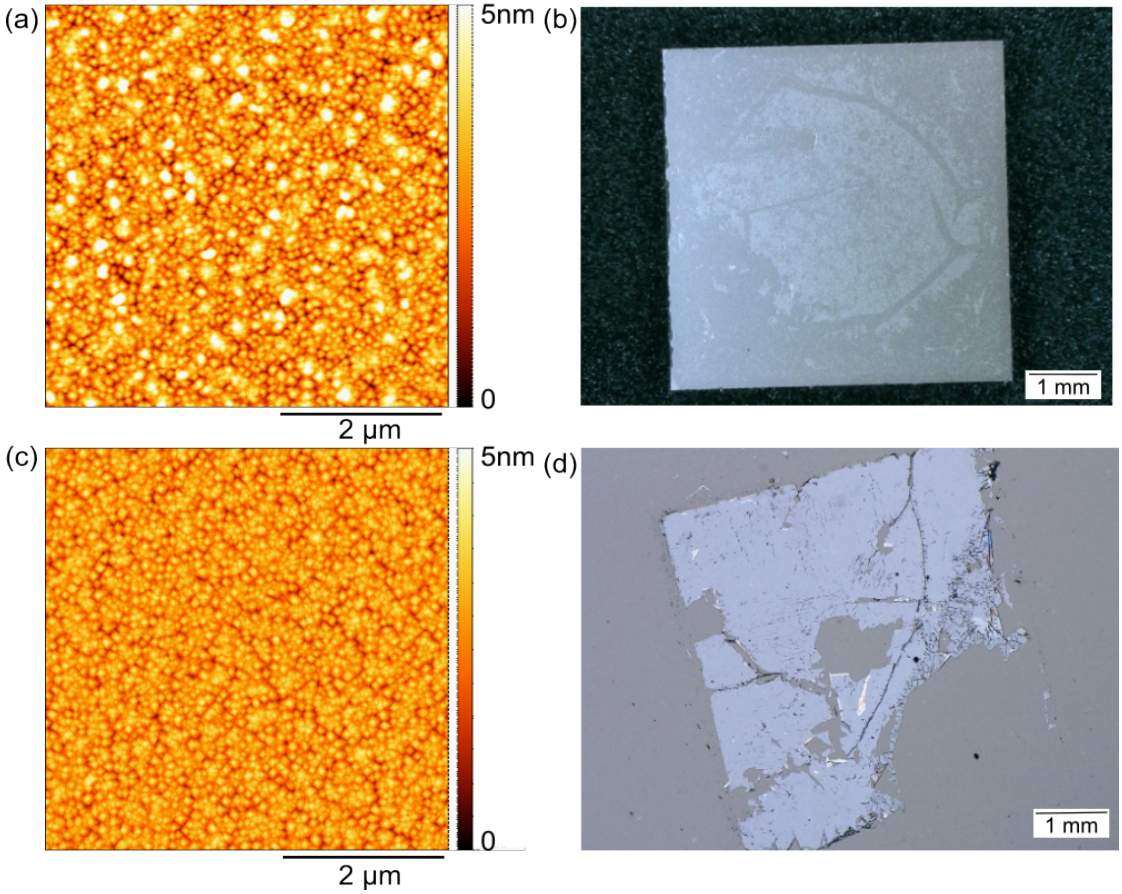

Figure 3.6: (a) AFM micrograph taken after depositing a 32-nm-thick layer of $Sr_2CaAl_2O_6$ and a 20-nm-thick layer of $SrTiO_3$ on a $SrTiO_3$ substrate. (b) AFM micrograph taken following the deposition of an 8-nm-thick $Sr_2CaAl_2O_6$ layer and a 14-nm-thick $SrTiO_3$ layer on a $SrTiO_3$ substrate (c). Optical images of the $SrTiO_3$ membranes from sample (a) and sample (c) transferred onto sapphire substrates are shown in (b) and (d), respectively.

To further study the influence of the buffer layer materials on transfer quality, two similar deposition setups were employed, which only differed in the buffer layer material. Both samples had a 10-nm-thick buffer layer topped with a 16-nm-thick $SrTiO_3$ layer. The first sample used $Sr_3Al_2O_6$ as a buffer layer, while the second used $Sr_2CaAl_2O_6$. Here, the deposition parameters for $Sr_2CaAl_2O_6$ and $Sr_3Al_2O_6$ were carefully optimized, resulting in AFM images that display smooth step-terrace features (Figure 3.7). Large-scale optical images showed intact membranes in both cases, but zoomed-in images revealed strip-like cracks in the $Sr_3Al_2O_6$ sample, attributed to strain release during lift-off due to the high lattice mismatch (1.43%) between $Sr_3Al_2O_6$ and $SrTiO_3$. Conversely, the $Sr_2CaAl_2O_6$ sample exhibited an exceptionally intact transfer, with an area of around 2 x 2 mm^2, which can be attributed to the little lattice mismatch (0.05%) between $Sr_2CaAl_2O_6$ and $SrTiO_3$.

Finally, fabrication of a large area sample (4.5 x 4.5 mm^2) was attempted to learn if a more extensive transfer is achievable. Using the optimized conditions—including a $Sr_2CaAl_2O_6$ buffer layer, optimized deposition parameters, and a 10-nm buffer thickness—the process successfully yielded a high-quality large-area transfer of 4.5 x 4.5 mm^2 (see Figure 3.8).

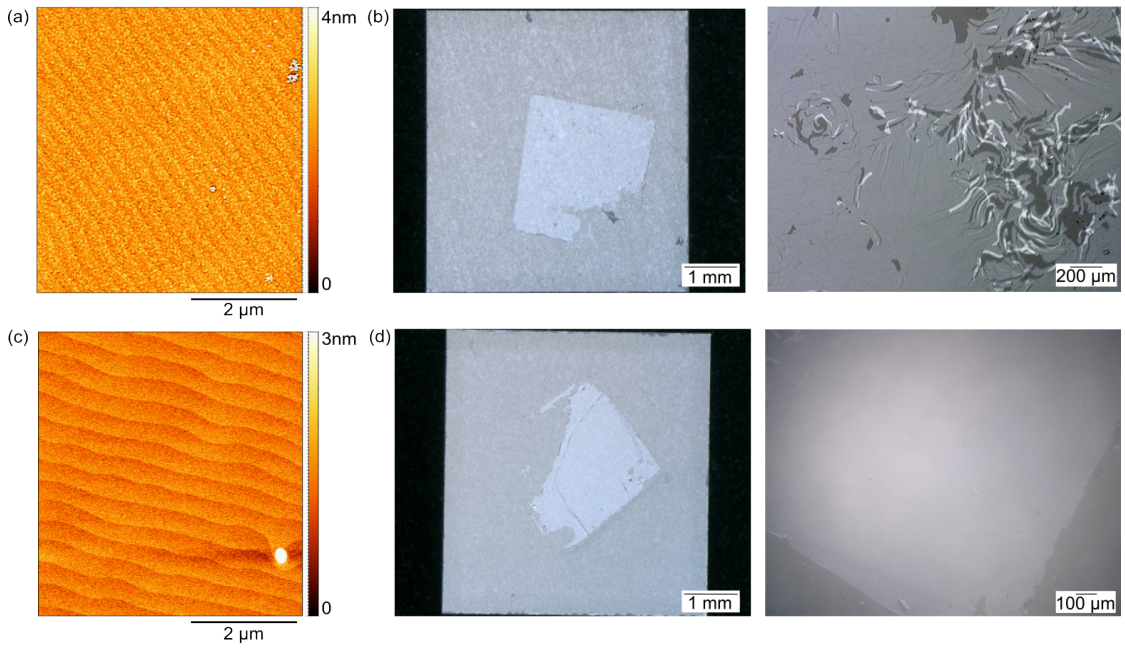

Figure 3.7: AFM images of two samples having similar designs with 10-nm-thick buffer layers on $SrTiO_3$ substrates, topped by a 16-nm $SrTiO_3$ layers. Sample (a) used $Sr_3Al_2O_6$ as buffer, while sample (c) used $Sr_2CaAl_2O_6$. Optical images of the $SrTiO_3$ membranes from samples (a) and (c), after being transferred onto sapphire substrates, are presented in (b) and (d), respectively.

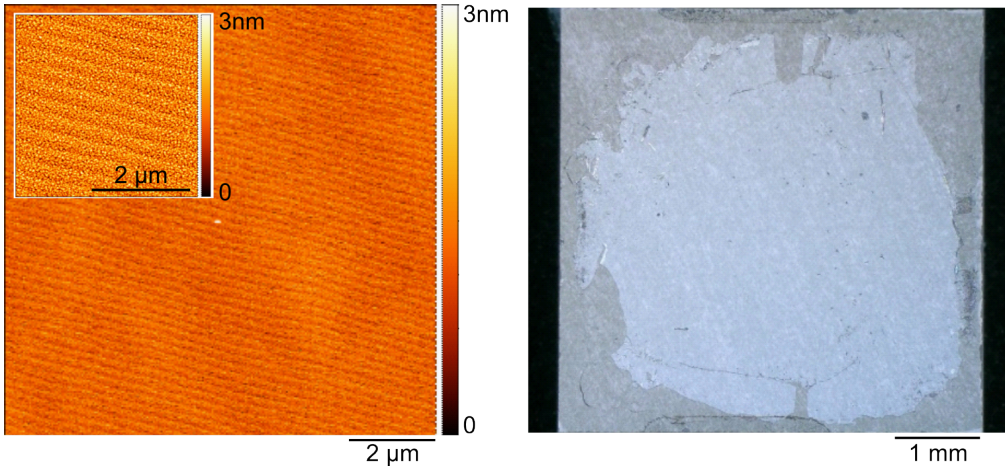

Figure 3.8: AFM image taken after a 10-nm-thick $Sr_2CaAl_2O_6$ and a 16-nm-thick $SrTiO_3$ film on a $SrTiO_3$ substrate (left). Optical image of the top $SrTiO_3$ membrane transferred on a sapphire shows a large-area transfer (right).

Chapter 4

Self-assembly of nanocrystalline structures from oxide membranes

In this chapter, I present a novel route to fabricating nanocrystalline oxide structures of exceptional quality utilizing freestanding oxide membranes. The thermally induced self-assembly of nanocrystalline structures is driven by dewetting $SrTiO_3$ and $LaAlO_3$ membranes once they are lifted off and transferred onto sapphire substrates. Upon annealing at temperatures below the melting point of the membranes, they self-assemble systematically into a variety of nanostructures such as nanovoids, nanowires, and nanocrystals. The orientation of the nanostructures is exactly provided by the crystal lattice of the transferred membrane. The microstructures of the oxide nanocrystals exhibit exceptional quality, characterized by pristine crystal structure and uniform stoichiometry, and their alignment exceeds the capabilities of lithography and ion-milling techniques. These findings illustrate the nanofabrication opportunities created by dewetting complex oxides. Furthermore, the physics underlying the self-assembly process in the membranes can potentially enhance our understanding of interface diffusion, which is important to epitaxial thin film growth.

This work presented in this chapter has been published in Ref. [35]. The text I use in the following chapter has been taken largely from Ref. [35], with appropriate modifications. Scientific conceptualization of the project was led by V. Harbola, J. Mannhart, and P. van Aken. Planning of the experiment was done by V. Harbola. Sample fabrication was conducted by V. Harbola and me. Substrate preparation was carried out by S. Smink, V. Harbola, and me. Characterization and experiment set-up were performed by V. Harbola and me. Scanning Transmission Electron Microscopy measurements were implemented by H. Wang. X-ray diffraction measurements were carried out by S. C. Parks. Analysis of the data was performed by V. Harbola and me. Writing was conducted by V. Harbola and J. Mannhart. All authors contributed to the scientific discussion.

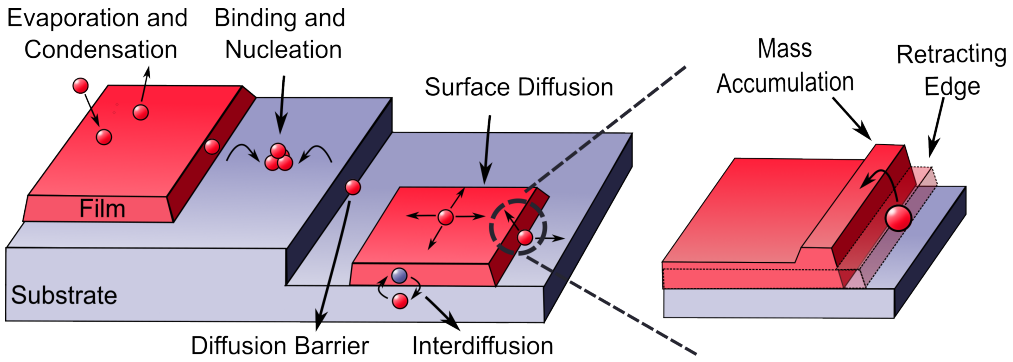

Figure 4.1: Atomic transport processes take place when a thin film is heated on a substrate. Surface diffusion process along the surface of the film or the substrate is relevant. During this process, a diffusing particle may encounter barriers along the substrate surface, bonding to a site and initiating the nucleation of a new crystalline island. Interdiffusion yields the exchange of materials between the film and the substrate. Particles can also undergo evaporation and condensation on the film surface. Capillary forces-induced edge retraction may introduce dewetting of the substrate surface. Reproduced under terms of the CC-BY license.[35]

4.1 Introduction

Scaling down in size is required more and more in electronic, optoelectronic, and medical applications. When structures are scaled down, material properties such as electronic, thermal, chemical, and optical properties differ from the bulk ones due to quantum confinement effects[36]. The study of nanocrystals improves the innovation in the applications[37–39]. The fabrication of nanocrystals can be divided into two main methods: top-down and bottom-up fabrication[36, 40, 41]. In the following, we will introduce a novel route to fabricate nanocrystals combining both top-down and bottom-up approaches. This method utilizes the intrinsic ability of atom agglomeration[42, 43] which is allowed in this case when a membrane is transferred onto a substrate so that the bonding between the membrane and the substrate is weak. This method produces high crystalline quality and well-faceted nanocrystals that, to our knowledge, haven't been reported by electron beam lithography or ion milling. During the process of annealing the membrane transferred on the substrate, mass transport such as evaporation and condensation, surface diffusion, and interdiffusion take place (Figure 4.1). Surface diffusion drives the material atoms at the edge to retract and accumulate which decreases the surface coverage and surface energy[42, 44–46]. This process is called dewetting. Dewetting was already been extensively studied in single-crystal configurations of elements[47–51] such as palladium[52], nickel[51, 53], and silicon[46, 54] and improves our understanding of the driving microscope process[42, 49–51, 53, 55, 56]. However, despite the wide study of dewetting, the study in oxide dewetting is largely lacking[48, 57, 58]. We attribute the lack of study to the high temperature required to dewet oxide materials, which is solved here by using a CO_2 laser beam at $10\,\mu$m wavelength.

4.2 Nanocrystalline structures

4.2.1 Orientation dependence of nanocrystallite formation

In the investigation of single-crystal films, we discovered that the dewetting morphology is influenced by several factors. These include the initial film orientation, lattice symmetry, temperature (T), and the initial thickness (t) of the membrane. These findings align with the observed behavior of Si and Ni in previous studies.[46, 49, 50] In this study, the single-crystalline $SrTiO_3$ oxide membranes are transferred onto a single crystalline sapphire substrate, which allows us to study the effect of the relative angle between the membrane and the underlying sapphire on the dewetting morphology. We found that the relative angle is an important factor. To investigate whether the relative orientation of the membrane and the substrate influence the morphology of dewetting, we diced one 5 mm x 5 mm sample into four pieces and transferred them onto a sapphire substrate with the $SrTiO_3(001)$ axis to equal 0°, 30°, 50°, and 90° with respect to the sapphire $[11\bar{2}0]$ axis. With this procedure, we can ensure the same membrane is measured during this orientation-dependence study. These $SrTiO_3$-sapphire stacks were systematically heated to 800-1200°C under 0.075 mbar oxygen pressure.

During the annealing process, the voids that first form are, with distinct exceptions, all remarkably rectangular shapes with the edges pointing precisely along the orientation of the membranes. The edges of the membranes are along <001> directions, thus the most significant dewetting fronts are also oriented in <001> directions. It is also noticeable that there are retracted fronts that are oriented 45° concerning the dominant rectangle voids showing that <110> is the second dominant agglomeration front for the $SrTiO_3$ membrane. Figure 4.2 displays the temperature-dependent evolution of dewetting for membranes as a function of the alignment angle with respect to sapphire $[11\bar{2}0]$. These results reveal that the surface energy of the $SrTiO_3$ facets governs the dewetting process. Strikingly, the interfacial adhesion energy between the membrane and the sapphire interface is less crucial in commanding facet formation. Indeed, we have consistently observed that the dewetting membranes of various orientations and materials align with the transferred orientation in all cases.

4.2.2 Dependence of nanocrystalline structures on membrane thickness and process temperatures

We now proceed to explore the dependence of nanocrystalline structures on membrane thickness and processing temperatures. (Figure 4.3) We found that both parameters play important roles in the morphology of dewetting. To study this, we grew four thicknesses of $SrTiO_3$ membranes and three thicknesses of $LaAlO_3$ membranes. The membranes were transferred onto sapphire and processed to various temperatures, while the evolution of the resulting dewetting morphology was studied. In all cases, we find that the samples self-assemble in the same three stages regardless of the membrane thickness, despite given heating time at different temperatures (Figure 4.4).

The first stage of the agglomeration process is the appearance of voids or holes in the membranes. According to the literature, the formation of voids requires local defects or preexisting holes.[42] The defects can exist as point defects, dislocations in the membrane, or irregularities on the substrate surface. These defects reduce the nucleation energy of new surfaces and voids. During the second stage, the void boundaries retract, allowing the voids to grow. The voids are mostly enclosed by well-defined facets that continue growing until the percolation threshold is reached. Highly faceted lines

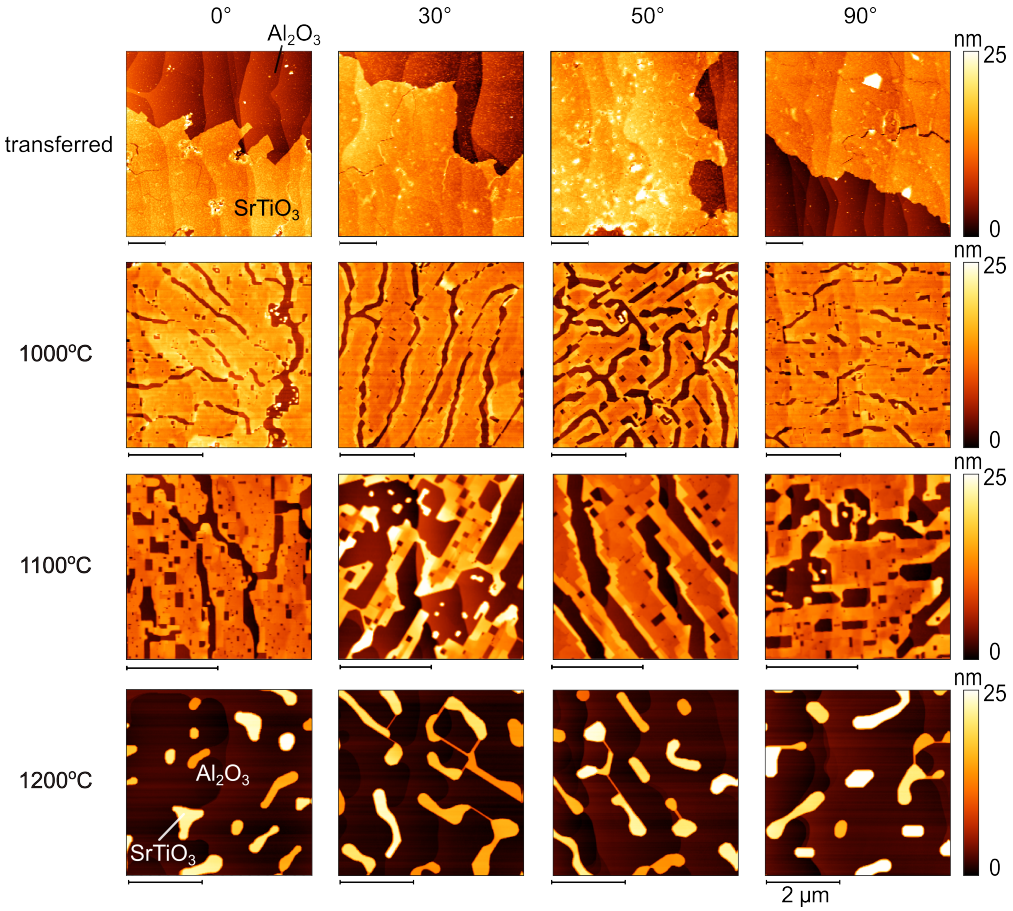

Figure 4.2: AFM scans depicts four $SrTiO_3$ membranes with distinct orientation on an Al_2O_3 substrate following thermal processing at different temperatures, as specified. All four $SrTiO_3$ membranes, each 8 nm in thickness, were obtained from a single sample. The scale bar for all presented scans is 2 μm. Reproduced under terms of the CC-BY license.[35]

and or strands form on a $\approx 500\,\text{nm}$ length scale connecting the separating nanocrystallites. As crystalline faceting stabilizes the nanocrystallites against a Rayleigh–Plateau instability[44, 59], the aspect ratio of these strands can far exceed 1.

When further processed to higher temperatures, the connectivity of the nanostructures is completely lost. In the third stage, well-faceted 3D nanocrystals oriented vertically in the growth direction develop with well-defined lateral facets. These three stages of agglomeration occur consistently in all thicknesses of the membranes, with the required temperatures shifting slightly higher with the increased membrane thickness. The step edges of the underlying sapphire, in general, do not affect the dewetting but act as a diffusion barrier. Many nanoparticles touch the step edges but they are rarely observed to drape over one.

The sapphire surface coverage by the membrane decreases monotonically with processing temperature, with the coverage–temperature curve shifting to higher temperatures as the thickness is increased (Figure 4.5a,b). We define the dewetting temperature (T_{dw}) as the processing temperature at which voids start showing up. The temperature T_{dw} increases monotonically as a function of membrane thickness for both $SrTiO_3$ and $LaAlO_3$ (Figure 4.5c). Furthermore, we observe the T_{dw} of $LaAlO_3$ to be consistently higher. A potential reason is that the stability of the $LaAlO_3$-sapphire interface is higher than that of $SrTiO_3$-sapphire. This behavior of increasing T_{dw} agrees with the dewetting behavior observed in other materials such as gold, silver, and copper reported in the literature.[60, 61]The mean height of the nanocrystals is another key parameter in characterizing the self-assembly process. We found that the thickness of the nanocrystals at the final stage increases as a function of the initial membrane thickness (Figure 4.5d). This finding is consistent with straightforward expectations, as thicker films provide more material to agglomerate.

4.2.3 Nanocrystalline self-assembly through material agglomeration

Above, I reported our findings on the experimental control of the self-assembly nanostructures. Here, I will analyze the self-assembly process and its potential for nanofabrication and device applications.

Throughout all stages of nanocrystalline restructuring, we observe self-assembly and the formation of pristine crystalline nanostructures. Starting at low temperatures, the voids enclosed with well-defined strands are formed. Nanowires are formed with increasing temperature. At the highest temperature we processed, the membranes depercolate and form nanocrystals in the end. The instability seen in single-crystal metal and semiconductor dewetting is largely absent here.[53, 56] The crystalline nature of oxide defines the morphology of the dewetting.

For all $SrTiO_3$ and $LaAlO_3$ membrane thicknesses we have tested, processing at 1300 and 1400°C, respectively, resulted consistently and repeatably in the formation of well-defined, singly oriented nanocrystals. The nanocrystals show two main features. The first is the top surface of the nanoparticle is atomically flat and shows the orientation of the original membrane. Second, the top and the bottom surfaces are connected by a low-index plane. For example, in the <100> direction of a 001 oriented nanocrystal, the connected plane is the 101 plane. Similarly, the 111 plane connects the two planes in <111> direction. The facets in $LaAlO_3$ are not clearly expressed, which we think is owing to the vertical face being located at the edge of the crystal.

In the second stage of the processing step, void growth takes place as the hole

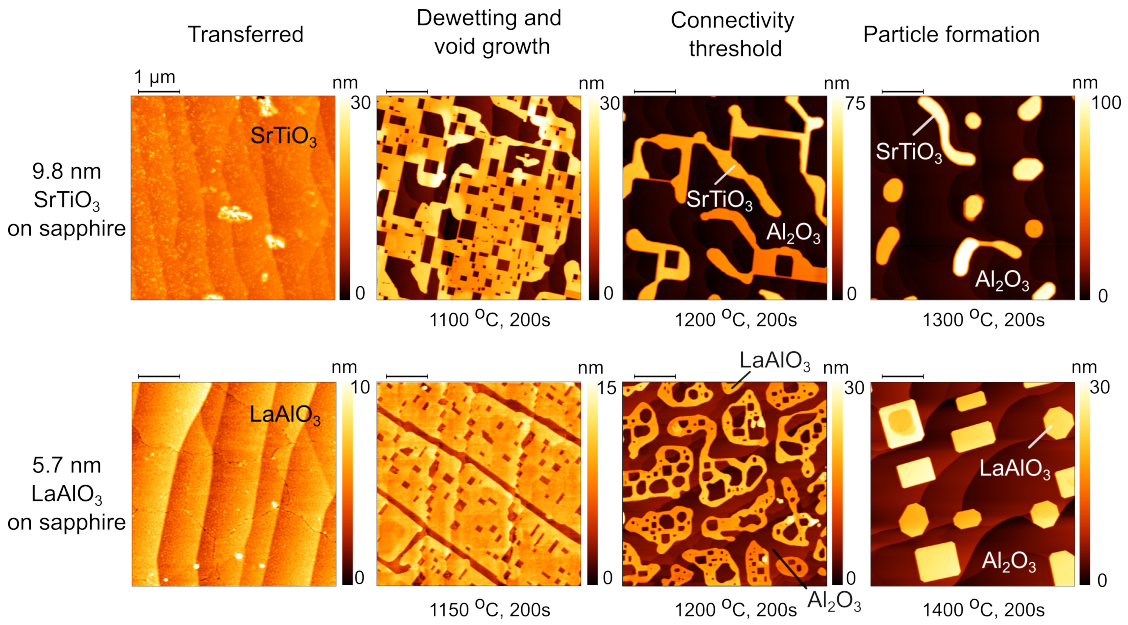

Figure 4.3: AFM images present the dewetting progression in $SrTiO_3$-sapphire samples(top row) and $LaAlO_3$-sapphire samples(bottom row) at different stages. The processing temperature, as illustrated, notably influences the dewetting process. The grid illustrates various dewetting stages for $SrTiO_3$ and $LaAlO_3$ membranes annealed at different temperatures. The consistent stages include the emergence of voids, subsequent void growth leading to depercolation and loss of connectivity in the membrane, and ultimately, the fragmented membrane coalescing into nanocrystals at the highest temperatures. A scale bar of 1 μm is provided for all scans. Each membrane undergoes thermal processing at the specified temperature for 200 seconds. The full thickness dependent grid is shown in Figure 4.4. Reproduced under terms of the CC-BY license.[35]

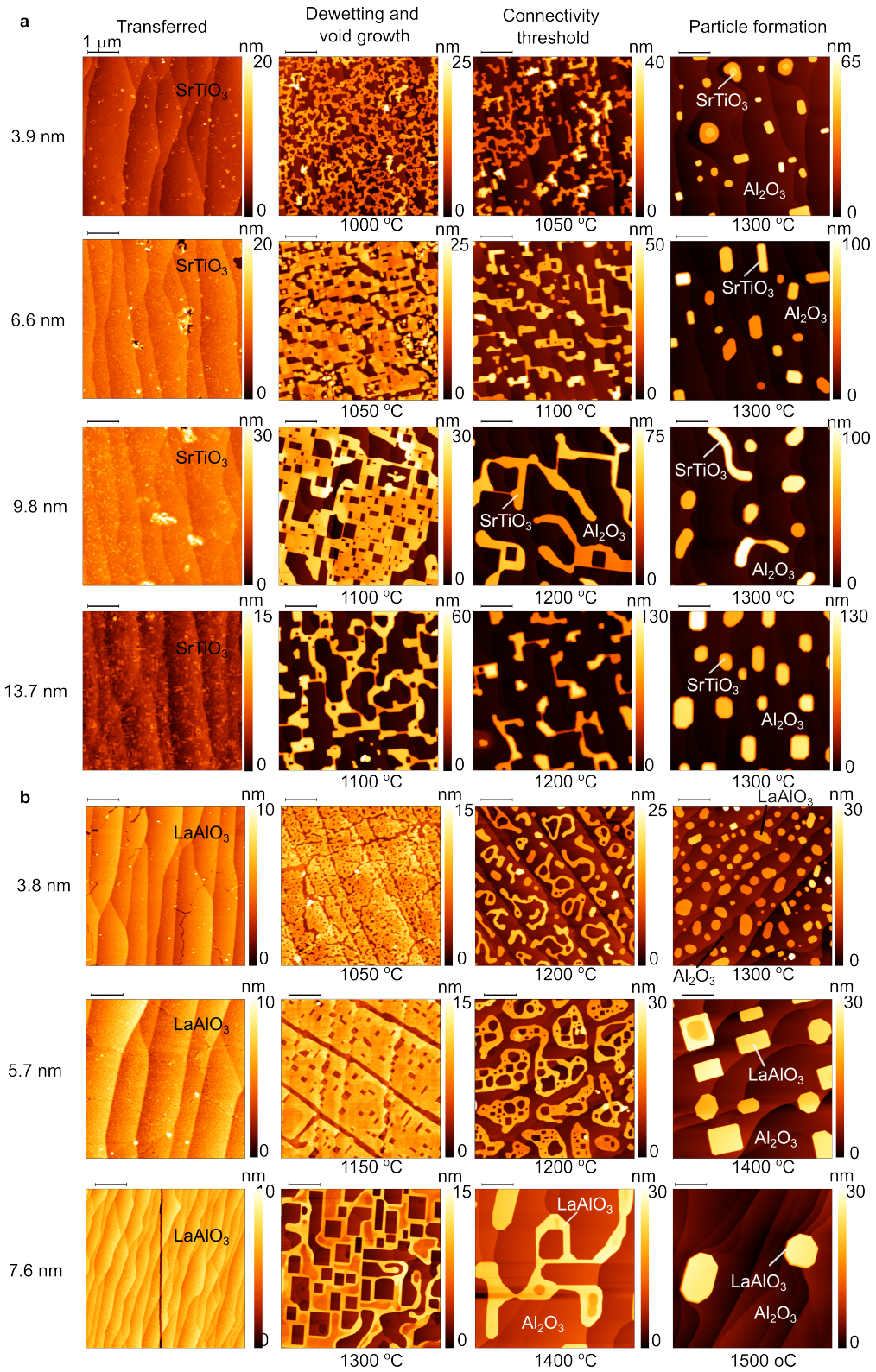

Figure 4.4: AFM micrographs showing the dewetting process at different stages for $SrTiO_3$-sapphire samples(a) and $LaAlO_3$-sapphire samples (b). The grid illustrates the evolution of dewetting in membranes of $SrTiO_3$ and $LaAlO_3$ with varying thickness, subjected to annealing at specified temperatures. The consistent stages of dewetting include the initial appearance of voids, subsequent void growth leading to depercolation, and the fragmented membrane coalescing into nanocrystals at elevated temperatures. A scale bar of 1 μm is provided for all scans. The thermal processing at each temperature is maintained for 200 seconds. Reproduced under terms of the CC-BY license.[35]

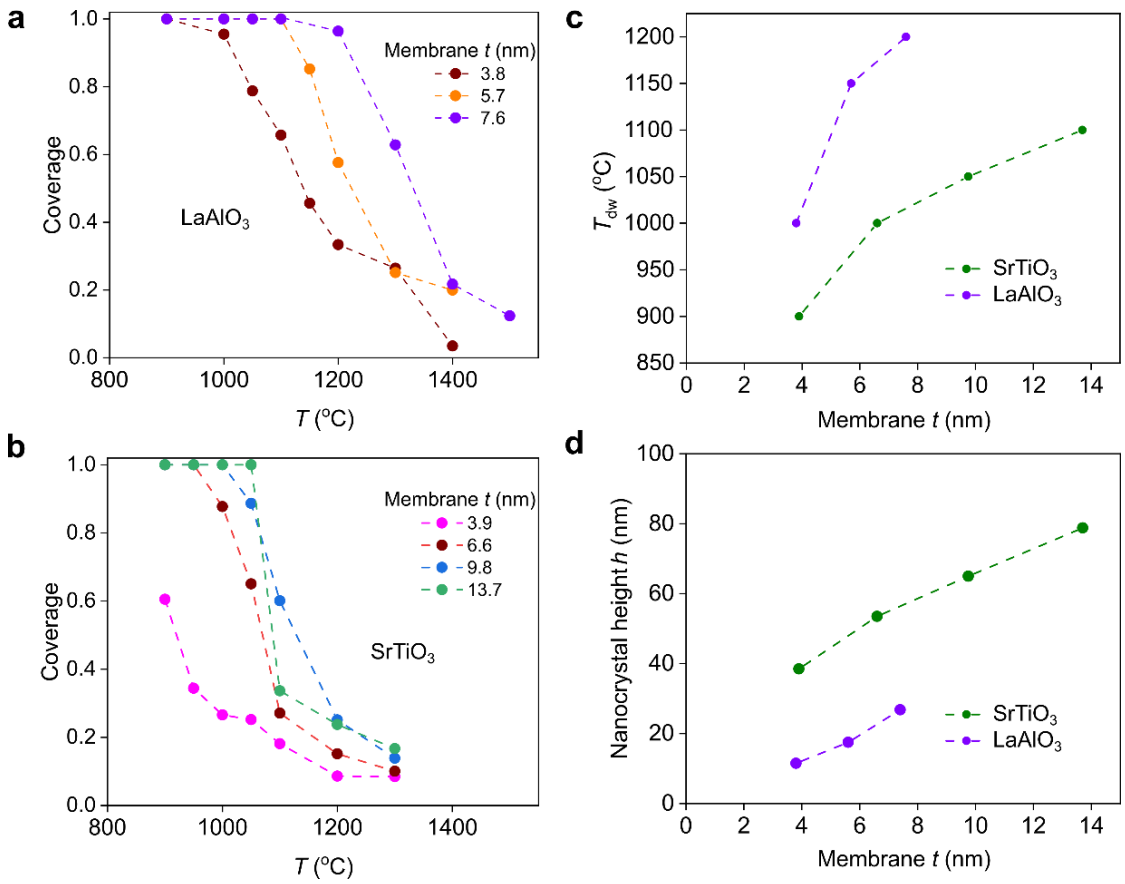

Figure 4.5: (a, b) Substrate coverage measurements are recorded as a function of process temperature (T). The progression of dewetting stages illustrates a decline in overall coverage with rising temperature. The membrane coverage decreases uniformly with increasing temperature, and the temperature at which film dewetting begins shifts to higher values as thickness increases. (c) A plot of the dewetting temperature (T_{dw}), where initial voids are observed, against the initial membrane thickness. T_{dw} exhibits a consistent increase with thicker membranes, although it remains notably lower than the melting temperature of $SrTiO_3$ and $LaAlO_3$.(d) The mean height of nanocrystals is plotted against the initial thickness of membranes. The mean heights show a continuous increase, as anticipated due to the larger amount of material available for nanocrystal formation. This image was made by Varun Harbola. Reproduced under terms of the CC-BY license.[35]

fronts retract along the low-index directions of the transferred membrane. The voids are mostly in a rectangular shape which measured 90° angles between the retraction fronts (Figure 4.6a).

As stated above, the crystalline nature of retraction fronts can stabilize the high-aspect-ratio nanowires since the edges of the nanowires do not go through a Rayleigh-Plateau-like instability. For example, we show high-quality $SrTiO_3$ and $LaAlO_3$ nanowires self-assembled and oriented along the <100> direction (Figure 4.6b). The highest aspect ratio of the nanowire we found was ≈ 30 for $SrTiO_3$. (Figure 4.7).

4.3 Characterization

To gain further insight into the formation and the properties of nanostructures, we studied them microscopically. By studying an initial 6.6 nm thick $SrTiO_3$ membrane processed at 1000°C and 1100°C for 200 s with scanning transmission electron microscopy (STEM) and electron-loss spectroscopy (EELS), we analyzed their crystalline quality, chemical homogeneity, and facets. Aligning with the atomic force microscopy (AFM) results, the STEM images show the density and the lateral size of the nanocrystallites to decrease with higher process temperature, while the thickness increases. (Figure 4.8). Moreover, the dewetted $SrTiO_3$ nanocrystallites show exceptional crystalline quality and possess low-indexed facets. High-resolution high-angular annular dark field-scanning (HAADF)-STEM images of $SrTiO_3$ nanocrystallites cross-sections present atomic lattice without visible defects anywhere (Figure 4.9a,b and Figure 4.10). The uniformity of the contrast in the HAADF image exhibits excellent structural homogeneity of these dewetted structures. The retracted edges present high crystallinity and well-defined facets right to the boundary (Figure 4.9a,b). Furthermore, the overall curvature increases with higher processing temperature, which is after annealing at 1100°C. This is owing to high indexed facets introduced. These results show that the surface energy of the crystalline facets stabilizes the surface of the nanocrystallites. No droplet formation was observed. The droplet shape provides the lowest surface energy and shows up when cohesive capillary forces are dominant. However, the increase of the curvature with increased temperature indicates the surface energy of a faceted structure and a smoothly curved surface are competitive. Throughout the processing process, the out-of-plane orientation of the crystallites remains in the [001] direction which is exactly provided by the transferred membrane. Note that during the sample fabrication, the transferred $SrTiO_3$ membranes are not fully aligned with the Al_2O_3 substrates, so the high symmetry directions of the substrates and membranes are different.

The distribution of the constituent elements of a single $SrTiO_3$ crystallite was analyzed by electron energy-loss spectroscopy (EELS). The EELS maps show the uniformity of the element distribution across the agglomerated geometry and the interface between the $SrTiO_3$ membrane and the Al_2O_3 substrates is sharp without visible interdiffusion. Atomically resolved STEM-EELS maps show the intensity of the Sr and Ti drop to baseline within 1 unit cell across the boundary revealing an atomically sharp interface between the transferred membrane and the substrate. These findings present the exceptional crystalline quality and elemental uniformity of the nanocrystallites that can be achieved by the self-assembly process. To our knowledge, the nanocrystalline structures with such high quality up to and including the edges exceed the capability that electron beam lithography or other top-down techniques like ion milling can achieve.

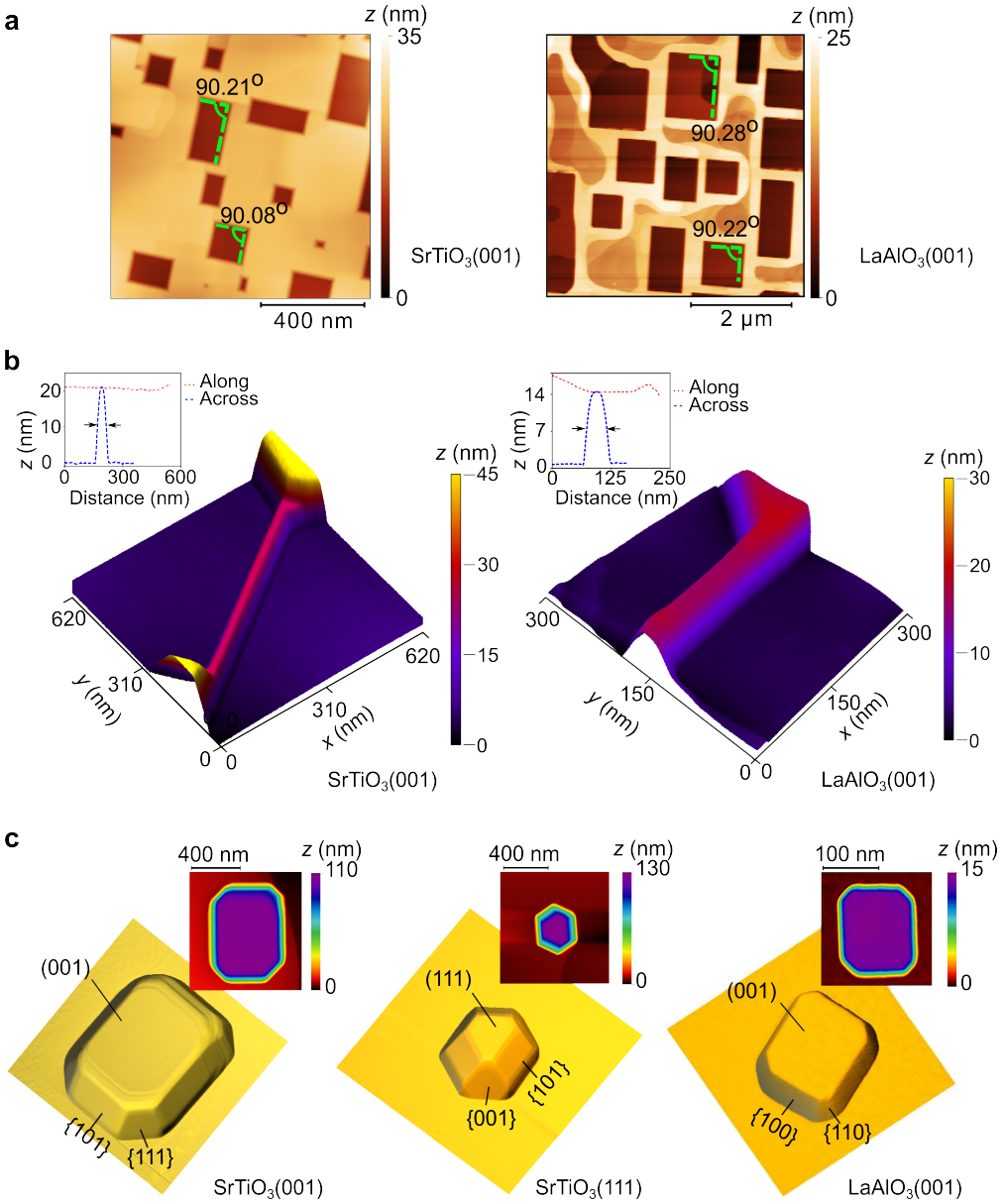

Figure 4.6: (a) AFM images capturing the development of interconnected crystalline voids in the initial stage of dewetting, featuring retraction along the crystalline <100> and <010> directions, quantified by measuring right angles between the retreating edges. In the left panel, nanovoids in $SrTiO_3$ (001) membranes are depicted, while the right panel illustrates nanovoids in $LaAlO_3$ (001) membranes. (b) 3D topography images showcase stabilized nanowires for $SrTiO_3$ and $LaAlO_3$ before the complete depercolation of the membrane, leading to the formation of nanocrystals. The left and right panels display the nanowires for $SrTiO_3$ and $LaAlO_3$, respectively. Insets provide line-cuts along and across the nanowire topography, revealing a flat top. The strands depicted have a Full Width at Half Maximum (FWHM) of 44 and 45 nm, respectively. The emergence of these nanocrystalline structures highlights the stabilizing effect of crystalline facet energy against the structural instabilities observed in the single-crystal dewetting of metals or semiconductors. (c) 3D topographies exhibit self-assembled nanoparticles from (001) and (111)-oriented membranes of $SrTiO_3$ and (001)-oriented membranes of $LaAlO_3$. Insets present a 2D height map of the same particle. The crystalline facets of these nanocrystals are distinctly identifiable and marked on the 3D AFM topographies. Reproduced under terms of the CC-BY license.[35]

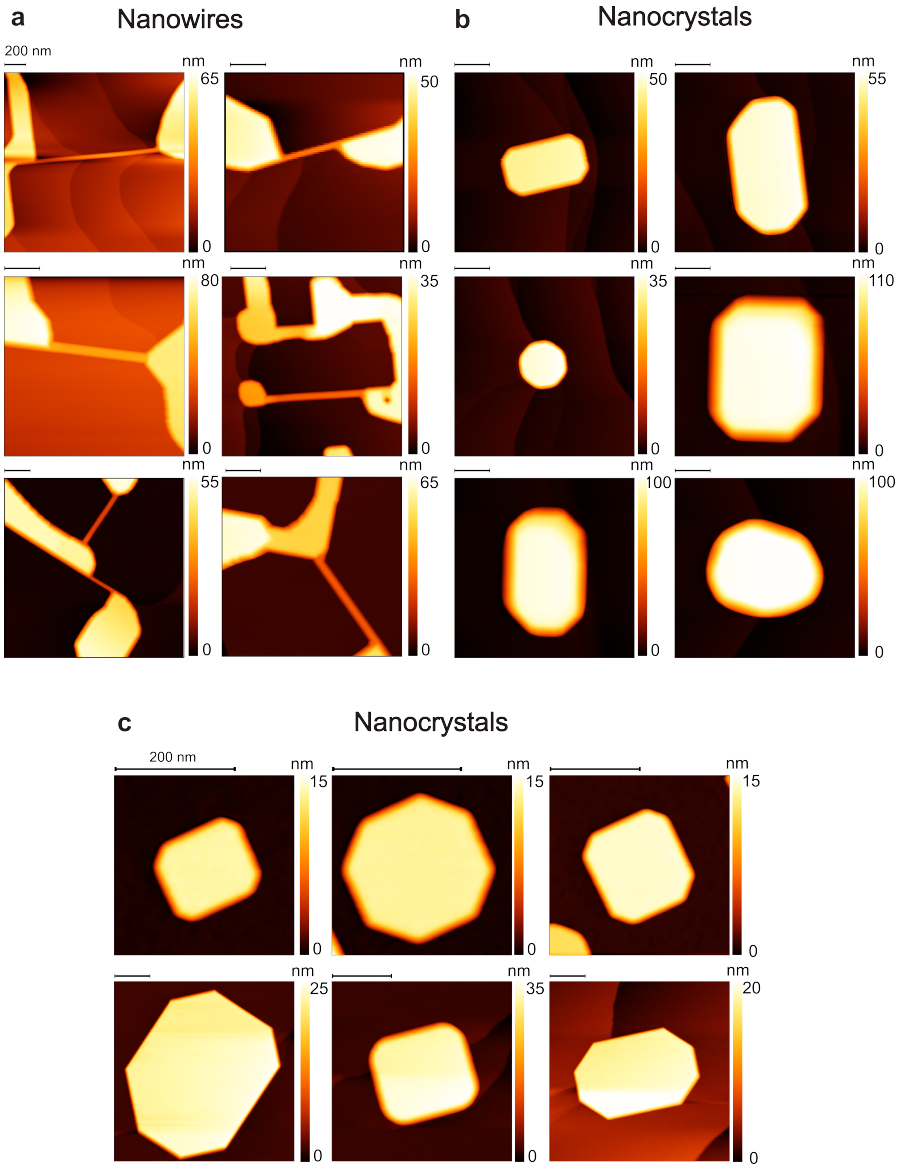

Figure 4.7: AFM images of (a) nanowires observed in $SrTiO_3$ membranes with thicknesses of 6.6 and 9.8 nm during thermal processing at temperatures of 1100°C and 1200°C, and (b) nanocrystals observed in $SrTiO_3$ membranes with thicknesses of 3.9, 6.6, 9.8, and 13.7 nm at 1300°C. (c) AFM images illustrating nanoparticles formed at 1300°C in transferred $LaAlO_3$ membranes with thicknesses of 3.8 and 5.7 nm.

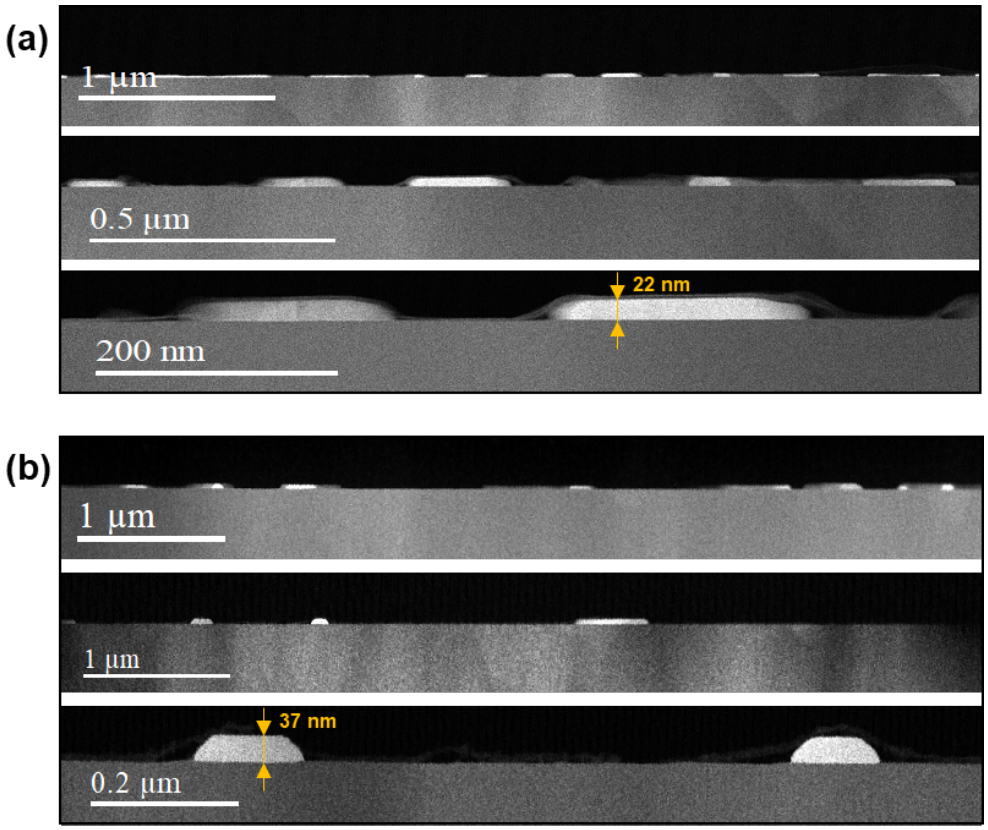

Figure 4.8: STEM imaging reveals a cross-section of a $SrTiO_3$ membrane after dewetting at (a) 1000°C and (b) 1100°C. The initial thickness of the $SrTiO_3$ membrane is 6.8 nm. Following dewetting, the thickness increases to 22 nm at 1000°C and 37 nm at 1100°C. Simultaneously, as anticipated, the lateral size of the dewetted $SrTiO_3$ nanocrystals is reduced. Micrographs were taken by Hongguang Wang.

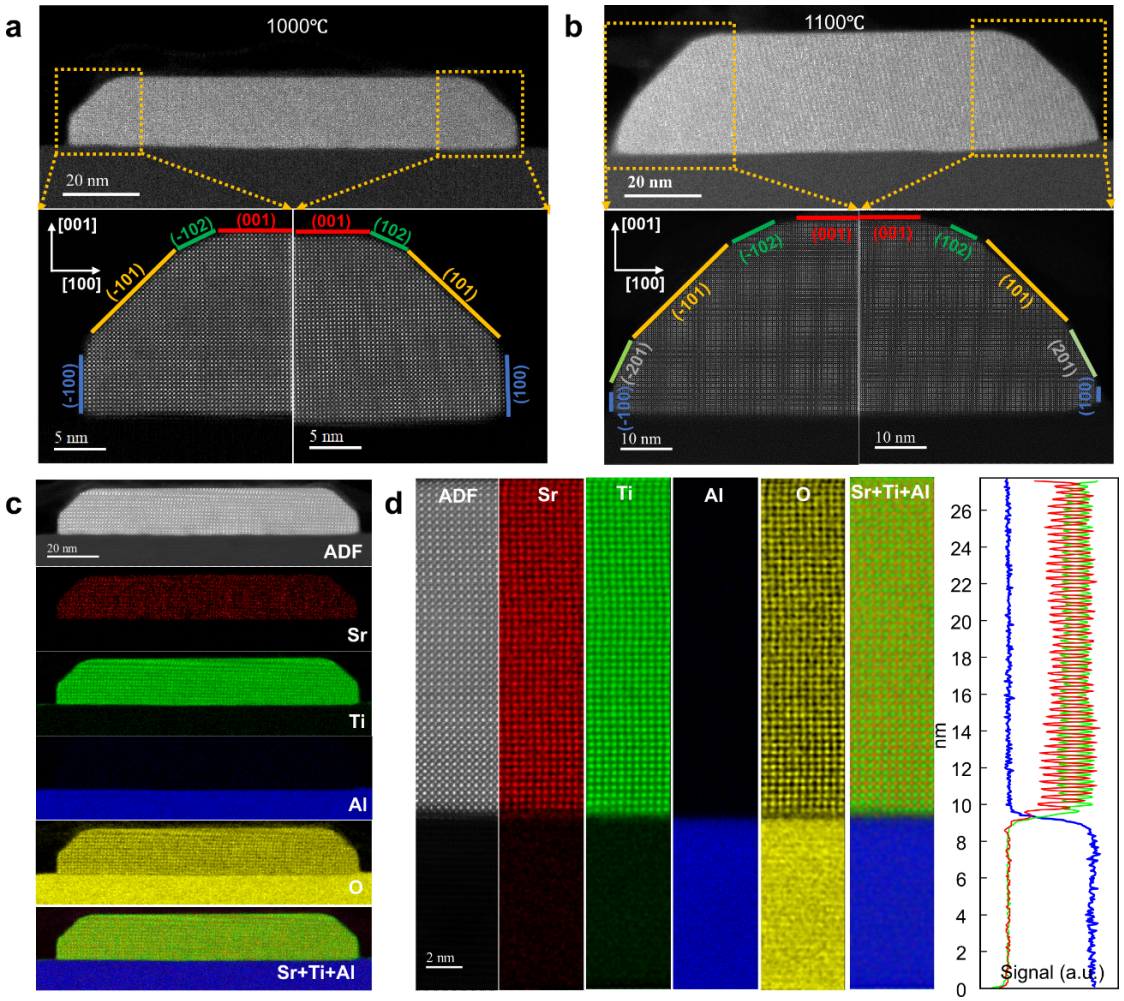

Figure 4.9: (a) STEM and EELS observations capture nanocrystalline structures formed through self-assembly. Post-processing at 1000°C, a $SrTiO_3$ membrane exhibits material agglomeration and recrystallization during dewetting. The thickness of this region increases to nearly three times the initial membrane thickness. A transition region, marked in the image, connects the top and bottom surfaces via crystalline facets. (b) Subsequent annealing at 1100°C causes further edge retreat, resulting in thicker regions after dewetting. The boundaries of this thicker structure display increased curvature, accommodated by the introduction of additional crystalline facets between the top and bottom faces of the crystallite. The crystal structure remains intact up to the boundary, with uniform contrast indicating minimal defect density. (c) An annular dark-field (ADF) image, elemental EELS maps for Sr, Ti, Al, and O, and a color-coded overlay of the elemental maps for Sr, Ti, and Al reveal an exceptional and uniform elemental distribution throughout the entire dewetted geometry. A sharp interface is evident between the membrane and the substrate. (d) A high-resolution ADF image, elemental EELS maps for Sr, Ti, Al, and O, color-coded overlay of elemental maps for Sr, Ti, and Al, and horizontally integrated intensity profiles for Sr (red), Ti (green), and Al (blue) across the interface illustrate the uniform distribution of Sr and Ti within the membrane and the atomically sharp interface between the membrane and the substrate. Micrographs were taken by Hongguang Wang. Reproduced under terms of the CC-BY license.[35]

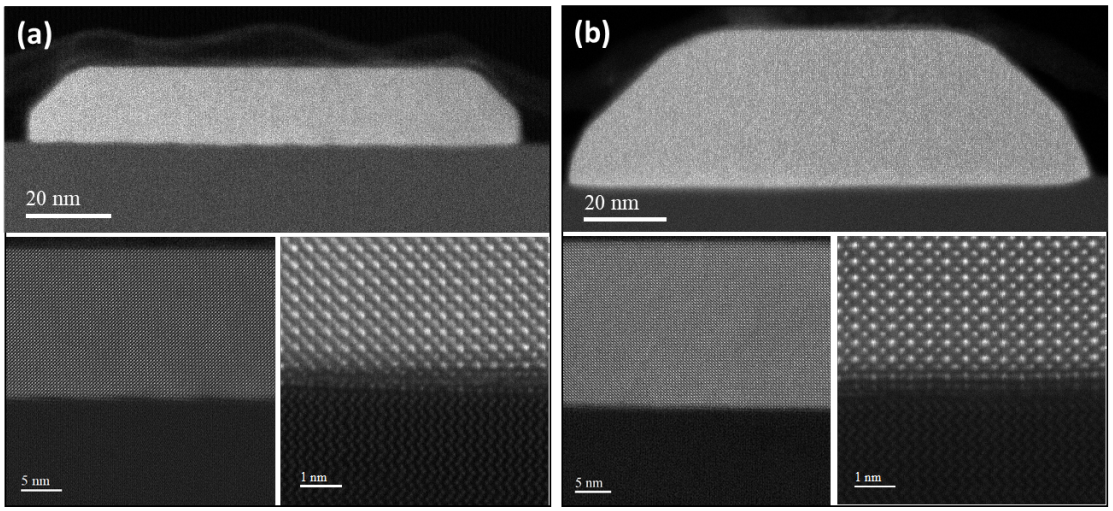

Figure 4.10: HAADF-STEM imaging captures a cross-section of a individual $SrTiO_3$ nanocrystallite after dewetting at (a) 1000°C and (b) 1100°C, along with the corresponding interfacial lattice structure. Micrographs were taken by Hongguang Wang.

4.4 Analytical model

To further analyze the energy relevant to the self-assembly process, we apply a model to the dewetting of $SrTiO_3$. This model follows the dewetting model of Ref. [48] and aims to predict whether a hypothetical hole present initially in the membranes may dewet, resulting in a reduction of membrane coverage. The formula compares the energy after dewetting E_{dw} with the energy of the intact membrane E_0, which is conducted for a square membrane with initial thickness h, size a, and a square hole of size x with 101 facets (Figure 4.11). The ratio of the energy of the dewetted structure to the energy of the initial structure can be determined using this geometry

$$\frac{E_{dw}}{E_0} = 1 - d^2 + \left(\frac{r_s}{r_{001}}\right)\left(\frac{1}{1+\frac{r_i}{r_{001}}}\right) + \left(\frac{4\sqrt{2}dr}{1-d^2}\right)\left(\frac{\frac{r_{011}}{r_{001}}}{1+\frac{r_i}{r_{001}}}\right) \tag{4.1}$$

where $d = x/a$ and $r = h/a$, and r_s represents the surface energy density of the substrate, r_{001} and r_{011} denote the energy densities of the 001 and 011 planes, respectively. As both the substrate and the membrane sides are oxides, we assume r_s/r_{001}=1 for simplicity. The energy ratio is plotted for various interfacial energy densities r, revealing that, for a constant aspect ratio, the probability of dewetting increases with higher interfacial energy (see Figure 4.11a). The ratio $E_{dw}/E_0 = 1$ serves as the dewetting threshold. When $E_{dw}/E_0 < 1$, the membrane dewets into a new structure.

This model reveals that holding the ratio of interface energy to 001 surface energy constant ($E_r = r_i/r_{001}$), thinner films dewet easier. Additionally, the maximum thickness capable of dewetting is determined for a given E_r. Moreover, an energy barrier for dewetting is obtained and serves as a threshold for the film to initiate dewetting and for voids to grow. Notably, voids are observed to reach a critical size before spontaneously growing. The energy barrier increases with thickness together with an increase in critical void size (Figure 4.12). Figure 4.11c-f illustrates the energy landscape of agglomeration, plotted through maps of E_r and r versus d. A critical E_r is established for each r by tracing the contour of 1. Dewetting becomes possible only when $E_r > E_r^{crit}$ (Figure

4.11c,d). Additionally, for a fixed E_r, dewetting does not occur beyond a well-defined value of r (Figure 4.11e,f). The critical size exhibits a monotonic increase with decreasing E_r and increasing r, as evident in the local maximum denoted as the barrier in Figure 4.11c-f.

This simple model consistently elucidates the thickness-dependent behavior observed in $SrTiO_3$ membranes. Furthermore, it functions as a tool for deducing the interface energy between the membrane and substrate based on the measured nanostructures. To achieve this, we consider the largest mean $r \approx 0.1$ identified in the self-assembled $SrTiO_3$ nanocrystals, as these represent the largest nanostructures formed without a void in the center. In Figure 4.11c,d, employing interface energy as a continuously varying parameter, the agglomeration energy maps enable the exploration of this parameter at the wetting-dewetting boundary for a given r. Taking the threshold value for r=0.1, as depicted in Figure 4.11c, we calculate E_r to be ≈ 2.4. Using r_{001} for the TiO_2-terminated $SrTiO_3(001)$ plane,[62] we derive $r_i = 3.11\,\mathrm{Jm}^{-2}$ for $SrTiO_3$ on sapphire. This value is comparable to the surface energies of binary oxides with a rock salt structure.[63] It is $\approx 50\,\%$ higher than the surface energies of pure metals,[63] a factor of ≈ 3 higher than common semiconductors[64], and exceeds that of the $SrTiO_3(001)$ plane by a factor of ≈ 2.4. Consequently, we anticipate that the interfaces between the membrane and substrate are thermodynamically less stable than those between the material and vacuum, making them more favorable to dewet.

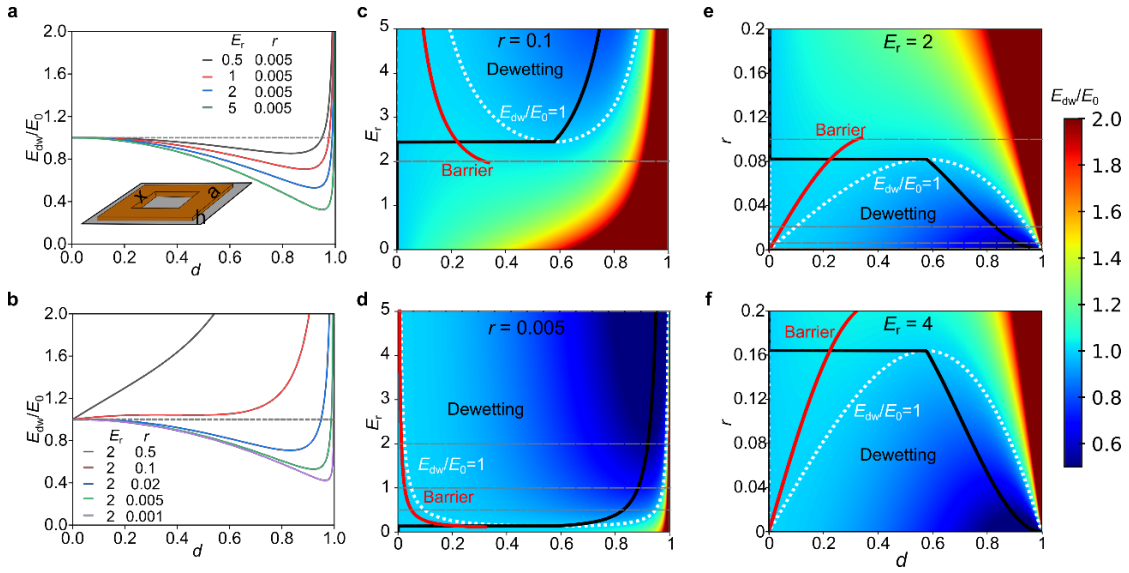

Figure 4.11: The outcomes of model calculations for the self-assembly process are presented. The panels compare the energies between a dewetted geometry and a structure with complete coverage during volume-conserving dewetting. (a) The energy ratio of the dewetted structure to a fully intact membrane transferred onto a substrate, maintaining a constant initial aspect ratio, and varying the ratio of interface energy to the energy of the (001) plane (E_r). The plot is a function of d, the ratio of void size to the lateral size of the initial membrane. The propensity to dewet increases with rising interface energy, resulting in larger void sizes and a higher energy differential between the dewetted and initial geometries. (b) Energy ratio for different initial h/a (r), with the same interface energy. The stability of the dewetted structure increases with decreasing r, indicating that thinner membranes are more prone to agglomeration. (c, d) Energy landscapes for a given r as a function of various values of E_r, where the dashed white curve outlines the contour of $E_r = 1$, demarcating the region where the dewetted membrane is thermodynamically more stable than the initial membrane. The phase space available for dewetting at different values of r is evident between (c) and (d). The red curve indicates the critical size for dewetting, representing the maximum of the energy barrier, while the black curve traces the minimum value of E_r. (e, f) Comparable maps to those in (c) and (d), but now for specified E_r values in relation to varying r values. This image was made by Varun Harbola. Reproduced under terms of the CC-BY license.[35]

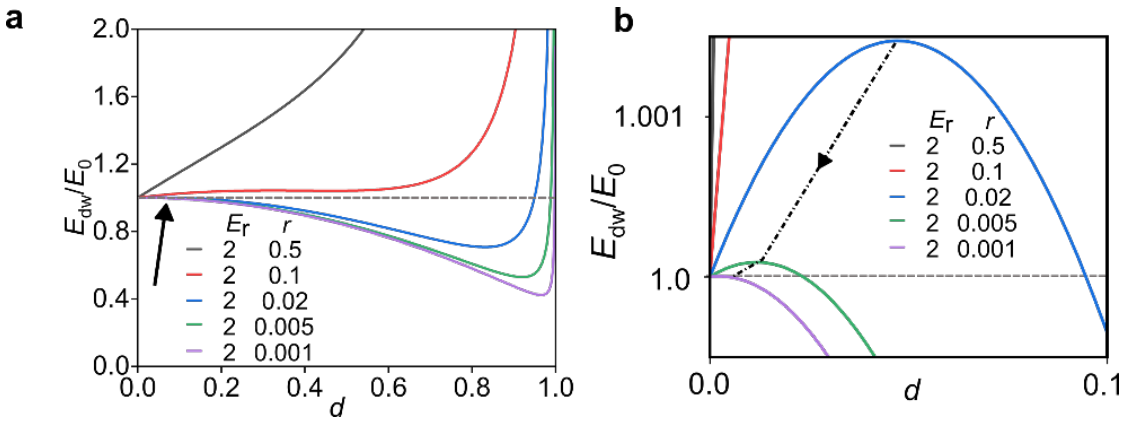

Figure 4.12: (a) Reproduced version of Figure 4.11(b). The solid arrow highlights the specific area that is magnified in (b) to clearly illustrate the energy barrier that exists prior to the occurrence of spontaneous dewetting in the model. The dashed line in (b) follows the position and height of the barrier, showing its changes with decreasing thickness. This image was made by Varun Harbola. Reproduced under terms of the CC-BY license.[35]

4.5 Conclusion and outlook

A new way to fabricate nanocrystalline structures has been found. This process utilizes the self-assembly of oxide membranes when processing them at high temperatures. By using the recently developed techniques, $SrTiO_3$ and $LaAlO_3$ membranes are transferred on thermal-prepared sapphire substrates. Upon annealing them to a temperature of half the melting temperature, the membranes self-assemble into nanocrystalline structures such as nanocrystals, nanowires, and nanovoids. Transmission electron microscopy evident the exceptional quality of the crystallinity of the nanostructures with uniform element distribution devoid of visible defects and well-defined facets on the edge. Nanocrystals with sizes down to 100 nm laterally and nanowires with aspect ratios exceeding 10 have been obtained. We have introduced an analytical model from which the interface energy between the membrane and the substrate is obtained. The self-assembly of a variety and high-quality nanostructures, influenced by temperature and thickness variations, offers new prospects for crystalline nanostructuring in oxide materials. Currently, we can manipulate facet orientation and crystallite size, but not the positions of nanovoids, nanocrystals, or the orientation of strands. Achieving control over these aspects seems possible by pre-templating membranes or substrates before processing.[43, 65–67] These findings show the opportunities for fabricating nanocrystalline structures through self-assembly. This unprecedentedly high quality exceeds the capability that electron beam lithography and ion milling can achieve. These nanostructures can be used in optics, catalysis, and nanoelectronics. The understanding of dewetting improves our knowledge in surface diffusion which is important to epitaxial thin film growth.

Chapter 5

Vector substrates: idea, design, and realization

Substrates play a crucial role in thin film deposition, but they do not always align with the specific requirements of a particular experiment or application. For instance, they might be expensive or unavailable with the desired crystal lattice structure.

To address this, this chapter introduces a novel concept of "vector substrates." In this approach, the template layer for growing thin films, referred to as the vector, is both chemically and structurally independent of the bulk of the substrate. Vector substrates are fabricated by transferring a membrane, which serves as the template layer and is grown on a reusable parent substrate, onto a carrier substrate. The template and carrier layers can be independently chosen and optimized, which offers unparalleled flexibility and reduces material costs. An interesting case comes to when the conventional substrate is expensive or hard to acquire such as bicrystal substrates. The details of bicrystal vector substrates will be discussed in Chapter 6.

The benefits and limitations of vector substrates compared with traditional substrates will be discussed in this chapter in detail. The feasibility of this technology has been validated by fabricating sets of viable vector substrates. Although the vector substrate concept is in its infancy, it holds significant promise to supplement conventional substrates and drives future advancements in substrate technology and thin-film deposition.

This work presented in this chapter has been published in Ref. [34]. The text I use in the following chapter has been taken largely from Ref. [34], with only minor modifications. Scientific conceptualization of the project was led by V. Harbola, J. Mannhart, and P. van Aken. Planning of the experiment was performed by V. Harbola. Sample fabrication was conducted by V. Harbola and me. Characterization and experiment set-up were performed by V. Harbola and me. Scanning Transmission Electron Microscopy measurements were carried out by H. Wang. X-ray diffraction measurements were implemented by F. V. E. Hensling. Analysis of the data was done by V. Harbola and me. Writing was performed by V. Harbola and J. Mannhart. All authors contributed to the scientific discussion.

5.1 Introduction

Thin solid films are essential for numerous device applications and foundation of research across a wide variety of fields. Substrates are trivially required for film deposition. For example, the growth of epitaxial films requires substrates with precise crystal structures, orientations, and minimal defects (see, for example, Ref. [27]). To achieve this, substrates for epitaxy are typically produced as single crystals, which are then cut, oriented, and polished. This process makes them costly, and finding or growing single crystals with the exact required lattice structure may not always be feasible.

To address the challenge of producing substrates from various materials in a cost-effective way, it is important to recognize that only the surface layer, a few unit cells thick, is structurally critical for film deposition. However, the high cost of conventional substrates arises primarily from the cost to provide an excellent crystal lattice throughout the entire substrate volume. For context, a typical substrate is on the order of 1 mm thick—roughly 10^5 times thicker than the top layer that is relevant for epitaxial growth, which is on the order of 10 nm (see Figure 5.1). As a result, a substantial portion of the substrate's mass is perfected in its structure at significant expense, even though it does not interface with the thin film. This leads to a waste factor of about 10^5. If the substrate is made from precious elements or isotopes, the same waste factor applies to their cost, as the number of atoms used is far greater than the number needed for achieving the desired function. Clearly, the majority of the substrate's volume primarily serves as mechanical support or to provide desired thermal properties—functions that could potentially be fulfilled by cheaper, more defect-prone materials with bulk properties desired for specific investigations or applications.

It is important to note that, in some cases, the challenges described here can be readily addressed by using an initial substrate which a film of the desired material has been grown to serve as a template layer for subsequent film growth. An example is the use of Si wafers coated with MBE-grown $SrTiO_3$ films,[68–71] a method pioneered over two decades ago. This approach is successful, but is limited to combinations of substrates and template layers that satisfy the requirements for epitaxial growth of the template film. This means the initial substrate must already have a suitable, high-quality crystal lattice. As a result, epitaxial growth of a template layer, such as single-crystalline $DyScO_3$ on an arbitrary substrate like polycrystalline Cu, is typically not feasible.

With the novel substrate technology proposed in this chapter, a very large number of materials can serve as a carrier for the template layer, which is chemically and crystallographically independent of the bulk substrate. The template layer is fabricated using thin-film deposition techniques as a membrane, and then transferred onto a carrier substrate (Figure 5.2).

This new type of substrates is referred to as "vector substrates" due to their resemblance to the traditional mathematical notation of marking vectors with an arrow above a letter. Just as these arrows indicate direction and magnitude, the membranes on the carrier substrates convey orientational crystallographic information necessary for epitaxial growth.

Vector substrates will self-evidently not replace conventional substrates but can serve as a viable alternative in certain cases. Both technologies offer distinct advantages and disadvantages, with their relevance depending on the specific application.

In the next sections, the deeper concept of vector substrates will be discussed,

including demonstrations of their feasibility. We will also focus on fabricating examples of vector substrates, such as $SrTiO_3$ (001) on c-cut sapphire or $LaAlO_3$ on Si, where we characterize their properties and demonstrate their suitability for epitaxial growth.

5.2 Concept of vector substrates

To meet the demands of film growth, various substrates are used depending on specific requirements, and several key considerations come into play. A wide variety of materials are employed for substrates, as highlighted in Ref. [27], and significant efforts have been made to optimize them, resulting in a wide spectrum of available substrates. Some substrates, such as silicon and sapphire, are of exceptionally high quality. The choice of substrate material depends on factors such as compatibility with deposition conditions, the desired structure of the thin film, further characterization needs, the intended application of the deposited thin film, and costs.

However, these factors can sometimes conflict with one another. For instance, available substrates may not always be ideal for the desired use case. $SrTiO_3$, commonly used in oxide electronic research, has a large dielectric loss factor and undergoes a structural phase transition at 105 K, which affects the strain in deposited films. In contrast, sapphire, while offering excellent microwave properties, has a hexagonal crystal structure that is unfavorable for growing cubic films commonly required in many applications.

To address this challenge, we developed the concept of vector substrates, which combine different materials for the bulk part of the substrate and the surface layer. The surface layer consists of a membrane grown using thin-film deposition techniques, typically on a parent substrate, which is then lifted off and transferred to a carrier substrate (Figure 5.2b). The template layer is carefully chosen and optimized to provide a desirable surface for film growth, while the carrier substrate can be independently optimized based on desired parameters such as mechanical, thermal, electronic, and magnetic properties, as well as cost considerations. The carrier substrate does not need to be a single crystal or atomically flat and can even be machined into specific 3D geometries, for example into curved shapes. Curvatures in a single direction are preferred for wrinkle-free membrane deposition on curved substrates. A membrane transferred in such a way as to preserve its crystallographic surface structure and orientation will enable epitaxial growth even on non-planar surfaces of vector substrates (Figure 5.2a).

An especially interesting case arises when a bulk single crystal of a desired material or lattice constant is difficult or impossible to obtain, but the material can be stabilized single crystalline in thin-film form. In such cases, vector substrates offer several innovative possibilities. Membranes with bicrystalline or related structures can be used to create specialized vector substrates. Bicrystal vector substrates are intriguing and will be explored in greater detail in Chapter 6. Additionally, multiple membranes can be attached to a single carrier substrate, potentially through stitching techniques, which have already been shown for 2D materials.[72] This approach not only enables the production of large-area substrates but also allows for the creation of single vector substrates with distinct surface areas that vary in material or crystal lattice.

Removing the sacrificial layer from the parent substrate, such as by dissolving it in water, preserves the structure of the parent substrate, and the original surface can often be restored through cleaning or heating procedures (see, for example, Refs. [19, 73, 74]), eliminating the need for polishing. As a result, parent substrates can be recycled many times, unlike standard substrates, which thin out with each polishing

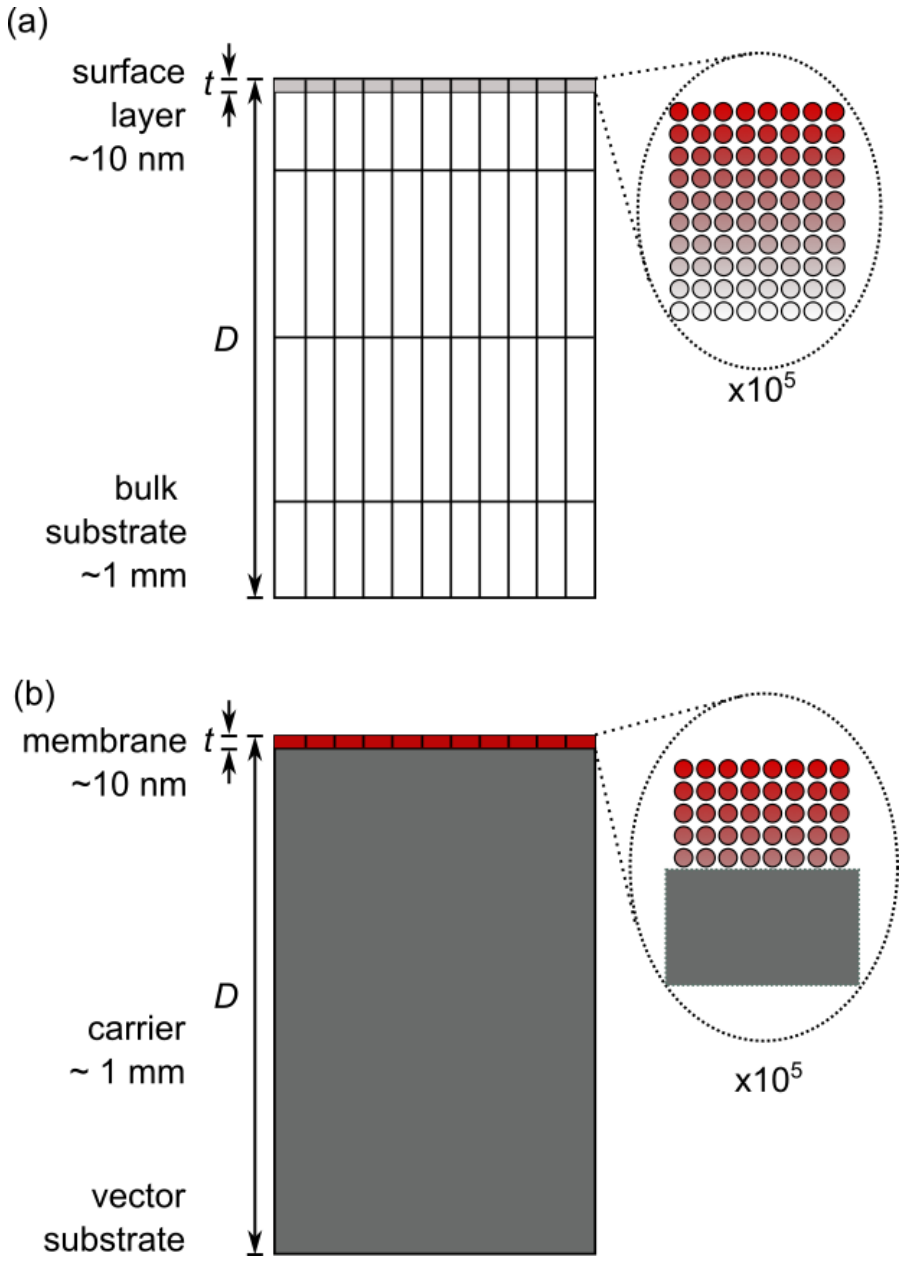

Figure 5.1: a) Sketch of a cross-sectional view of a conventional substrate made of a single crystal with thickness D, where only a thin surface layer of thickness t is active for film growth. The magnified section highlights the decreasing influence of atomic layers on thin-film deposition as the distance from the substrate surface increases. b) Sketch of a cross-sectional view of a vector substrate, consisting of a bulk carrier material coated with a membrane. The membrane material is selected to serve as an optimal template for thin-film deposition. This image was made by Varun Harbola. Reproduced with permission.[34] Copyright 2023, John Wiley and Sons.

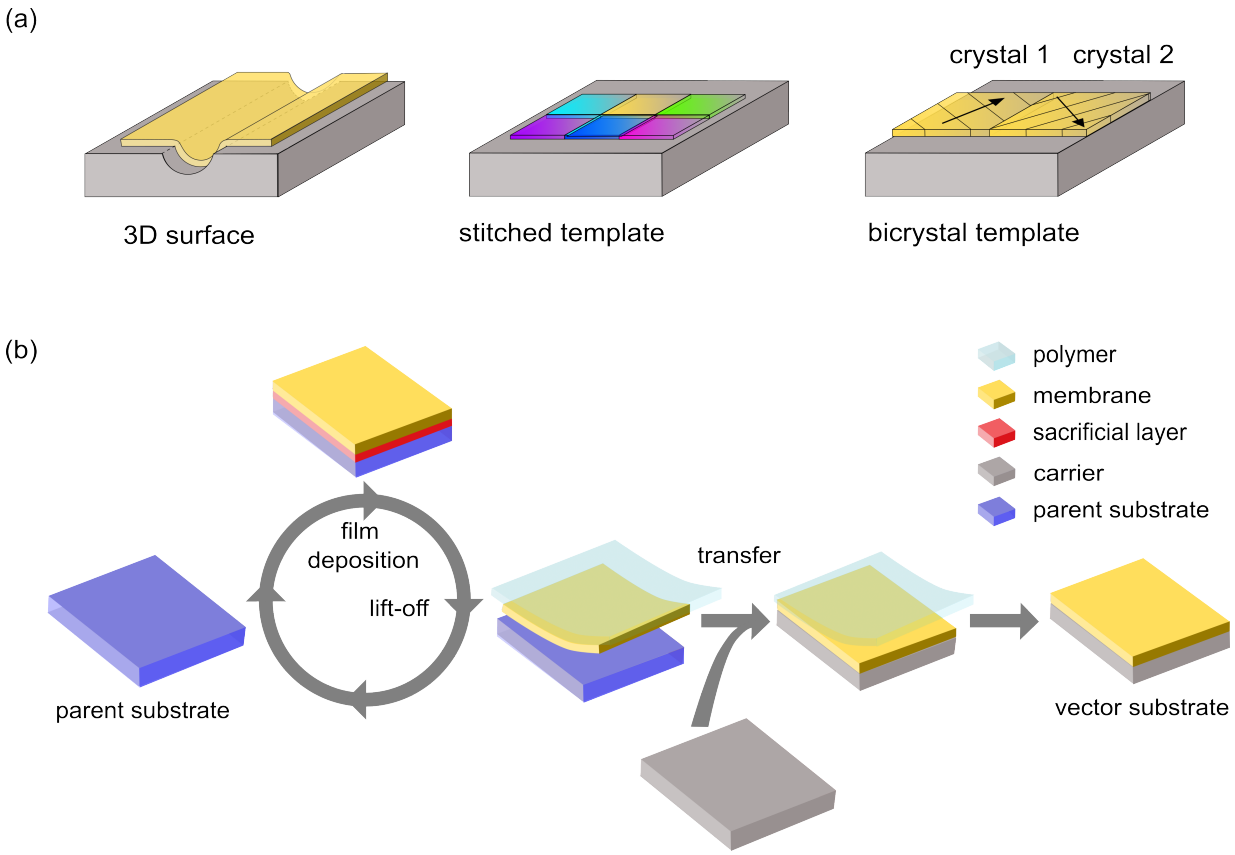

Figure 5.2: a) The integration of membranes with carriers to form vector substrates offers numerous new opportunities for film growth that are not available with conventional substrates. Starting from the left: epitaxial growth is feasible on vector substrates, even for curved or 3D textured surfaces, as the crystal lattice of the transferred membrane aligns perpendicularly to the carrier surface. The middle panel sketch illustrates the stitching of various template layers, resulting in a vector substrate with locally defined templates. The right panel shows how bicrystalline membranes can be used to produce cost-effective bicrystalline vector substrates. b) A workflow diagram detailing the process of fabricating freestanding membranes and bonding them to carrier substrates to create vector substrates. Left: A sacrificial layer and a thin film (which will become the membrane) are deposited on a parent substrate. Center: The sacrificial layer is selectively dissolved, lifting off the membrane, which is supported by a polymer layer and transferred onto the carrier. Right: The polymer support is removed, producing the vector substrate with a template layer ready for film deposition. After a heating step, the parent substrate may be reused for further depositions. Reproduced with permission.[34] Copyright 2023, John Wiley and Sons.

step. Additionally, vector substrates can be used as parent substrates, further reinforcing the recycling loop. All membranes grown on the same parent substrate will share the same vicinal cut, allowing the production of numerous vector substrates with identical surface orientations. This level of uniformity is not achievable with standard substrate technology due to variations among crystal boules and substrate batches.

The fragility and flexibility of membranes pose challenges for the lift-off, transfer, and positioning processes, so automation is essential for large-scale production. Although manual fabrication of vector substrates with $SrTiO_3$ membranes at surface areas of $2.5 \times 2.5\,mm^2$ and $5 \times 5\,mm^2$ is possible and meets certain research needs, many applications require substrates on the scale of centimeters or even tens of centimeters, which raises concerns about scalability. Currently, it remains uncertain whether vector substrates can be fabricated or made competitive at these larger scales, so further research is necessary to address these challenges and the following ones:

- Typically, after membranes undergo dissolution of their sacrificial layer, such as in water, they are transferred onto the carrier substrate in air, leading to potential contamination and defects at the interface.
- Vector substrate surfaces should not be polished or treated with harsh chemicals, as these can easily remove the template layer.
- High-temperature annealing of the vector substrate requires careful control to prevent membrane dewetting. [35]

These limitations, along with current technological challenges in vector substrate fabrication, will be discussed further below.

5.3 Fabrication of vector substrates

The two essential components of a vector substrate, the carrier substrate and the membrane, are prepared independently and then joined to form the final vector substrate. The process begins with the growth of a template layer on a parent substrate, which carries a sacrificial buffer layer (Figure 5.2b). Once the buffer layer is removed, the template layer is lifted off with the help of a support layer, such as a polymer film. The assembly is placed on a chosen carrier substrate, and after removal of the support layer produces the vector substrate. The parent substrate can be reused multiple times.

To explore the feasibility of this technique, four types of vector substrates have been fabricated in this thesis work: $SrTiO_3$–sapphire, $SrTiO_3$–Si, $LaAlO_3$–sapphire, and $LaAlO_3$–Si using the membrane–carrier substrate notation (Figure 5.3 and 5.4). Detailed studies were conducted on vector substrates made of $SrTiO_3$ template layers on c-plane-oriented sapphire carrier substrates. $SrTiO_3$ was chosen due to its common use as a substrate material and its structural phase transition at 105 K, which often introduces artifacts in epitaxial films grown on bulk $SrTiO_3$ crystals. Further studies in this chapter will explore whether vector substrates can overcome these limitations.

The exemplary vector substrate consists of a $4.5 \times 4.5\,mm^2$ $SrTiO_3$ membrane placed on the (0001) surface of a sapphire carrier (Figure 5.3a). The sapphire was conditioned by annealing at 1615 °C in UHV for 200 s, resulting in a step-and-terrace surface morphology.[75] The $SrTiO_3$ film was grown by pulsed laser deposition (PLD) onto a 10-nm-thick $Sr_2CaAl_2O_6$ buffer layer, which was also grown by PLD on the

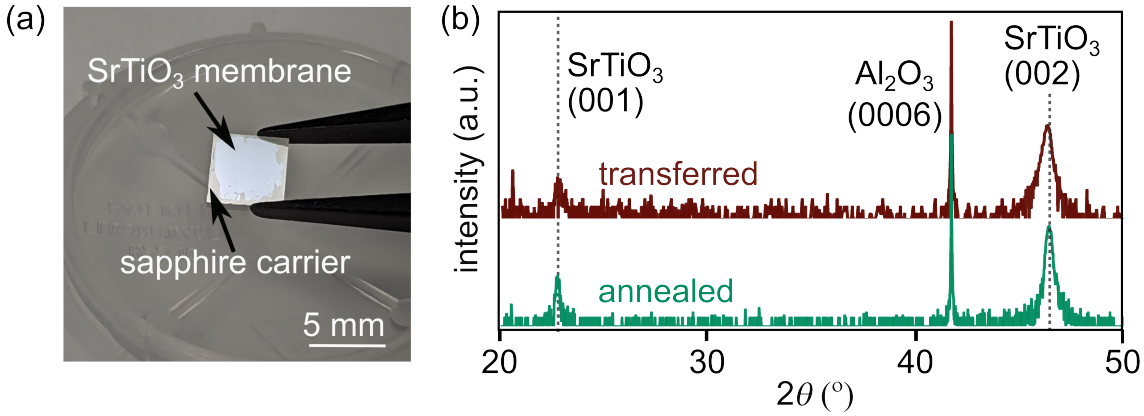

Figure 5.3: a) Optical image of the vector substrate consisting of a (001) $SrTiO_3$ membrane on a sapphire substrate oriented along the [0001] direction. The image shows the extensive coverage of the sapphire surface by the membrane. b) X-ray diffraction pattern from a symmetric 2θ-w scan, revealing that the single-crystalline nature of the transferred membrane and the thermal stability of the vector substrate. The bottom trace was obtained after annealing the template at 850 °C for 200 s in 0.1 mbar of O_2. Reproduced with permission.[34] Copyright 2023, John Wiley and Sons.

$SrTiO_3$ parent substrate. PMMA 950K C5 was spin-coated onto the $SrTiO_3$ film and used as the support polymer layer for membrane transfer.

The resulting heterostructure was immersed in deionized water, where the buffer layer dissolved after one day, releasing the PMMA-coated $SrTiO_3$ membrane. The membrane was then transferred onto the sapphire carrier, although potential wrinkles and folds could form due to water drainage and weak adhesion. Therefore, wrinkling was minimized by maintaining a hot plate temperature of 80 °C during transfer, resulting in a clean and smooth interface with wrinkle spacing exceeding 1 mm.

The PMMA support layer was dissolved in acetone at 50 °C, which left behind a smooth $SrTiO_3$ membrane on the sapphire. Chapter 3 provides more details of membrane fabrication. X-ray diffraction (XRD) studies confirmed excellent crystallinity of the $SrTiO_3$ template layer and a clean interface with the sapphire. So far, the $SrTiO_3$ parent substrates have been reused up to three times. It is found that it is also possible to transfer membranes onto curved carrier surfaces, as exemplarily shown in Figure 5.5.

5.4 Characterization of the vector substrates fabricated

The behavior of vector substrates with 2.5 × 2.5 mm^2 template layers during thermal annealing was systematically investigated (Figure 5.6) for two primary reasons. First, to assess the stability of the membrane layers during high-temperature treatments required for the epitaxial growth of subsequent films, and second, to explore the potential of using thermal annealing to achieve single-terminated vector substrate surfaces. Annealing the sample at approximately 850 °C for 200 s consistently restored the smoothness of the originally deposited $SrTiO_3$ films after transfer, without introducing additional defects (Figure 5.6c). Lower-temperature annealing did not effectively restore the surface, while higher temperatures further reduced surface roughness but introduced few-unit-cell-deep pits in certain areas subjected to dewetting as discussed in the study of chapter 4.

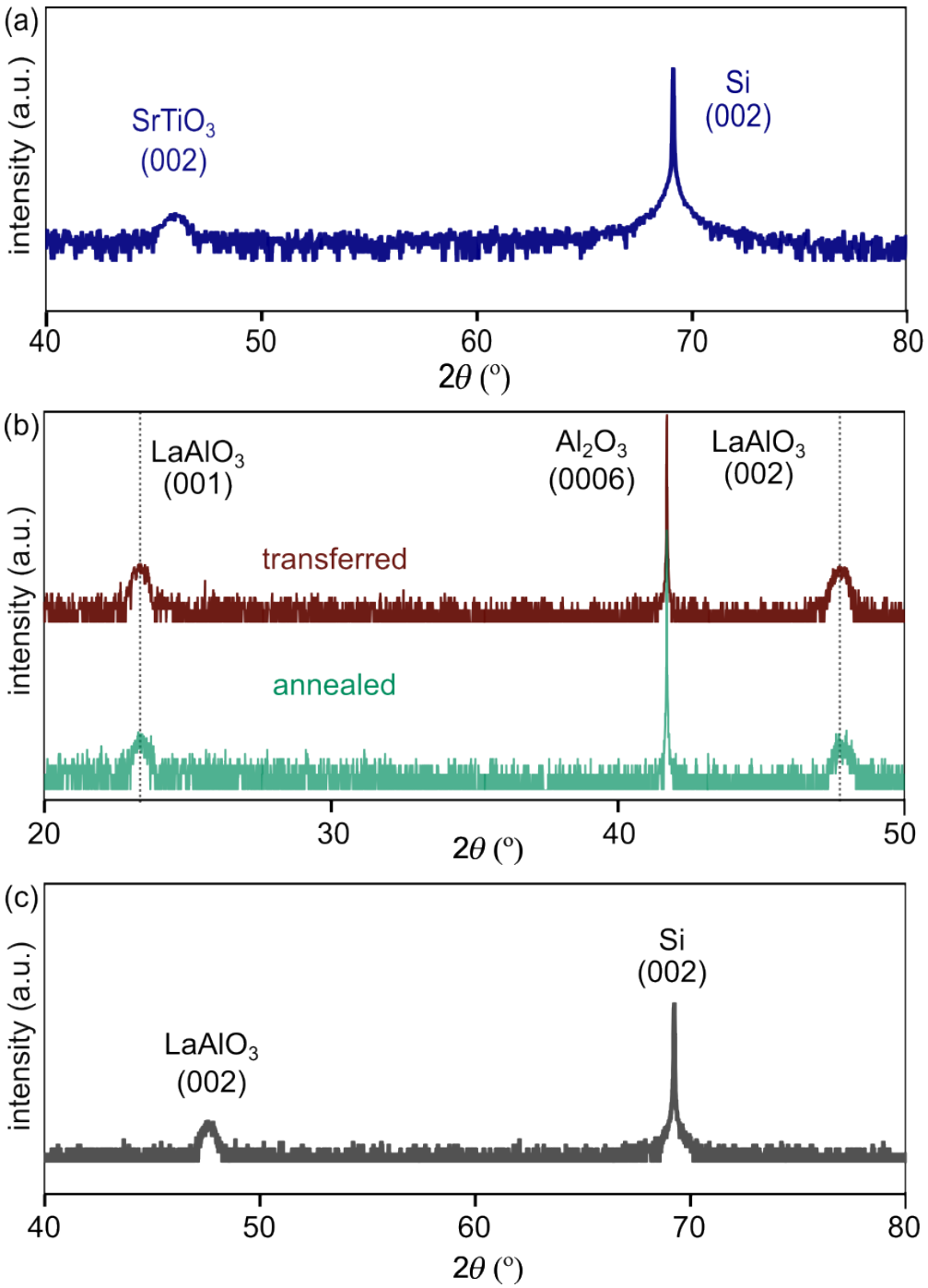

Figure 5.4: Symmetric 2θ-w scans of (a) a $SrTiO_3$ membrane transferred onto silicon as a carrier, (b) a $LaAlO_3$ membrane transferred on sapphire as a carrier revealing that the single-crystalline nature of the transferred membrane and the stability of the vector substrate to thermal annealing, and (g) a $LaAlO_3$ membrane transferred onto silicon as a carrier.

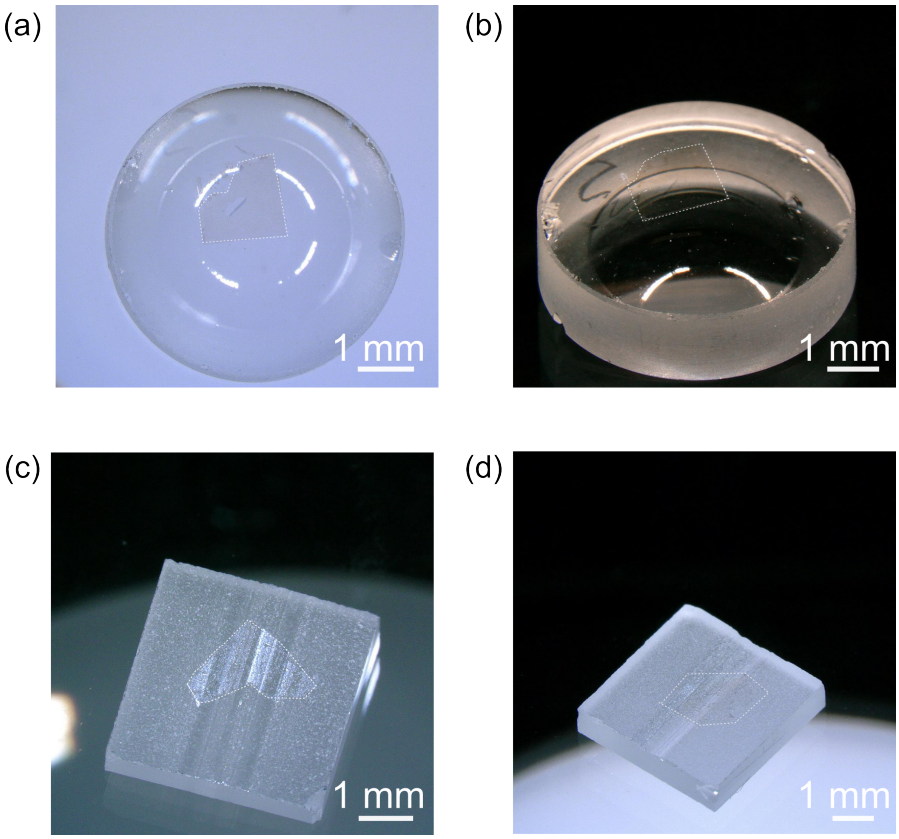

Figure 5.5: Optical images of vector substrates with non-planar surfaces, featuring single-crystalline $SrTiO_3$ membranes transferred onto 3D curved structures. In (a) and (b), the substrates consist of 30 nm thick [001]-oriented $SrTiO_3$ membranes transferred onto convex glass lenses, using the transfer process detailed in the chapter. The vector substrates in (c) and (d) are sapphire carriers that have been machined to include either a 0.1 mm wide ridge (c) or trench (d) along the length of the substrate. For clarity, the membrane edges are highlighted with a dotted white line.

At each stage of vector substrate preparation, surface quality was evaluated using atomic force microscopy (AFM) (Figure 5.7). The vector substrate was annealed under the optimized condition (850 °C, 200 s, 0.1 mbar O_2) for surface preparation. X-ray diffraction (XRD) verified the structural stability of the vector substrates throughout the thermal annealing process (Figure 5.3b). For material systems such as TaS_2 on Ta, previous research has shown that a strong interfacial bond is critical for achieving the desired surface properties.[76] Fine-tuning the interfacial bonding through specific membrane-carrier combinations may be important in these cases, although no such scenario has been encountered in this research yet.

Given the high structural quality of the vector substrates, the next step was to assess their suitability for high-quality epitaxial growth. To this end, the epitaxial growth of $La_{0.67}Sr_{0.33}MnO_3$ (001) films on $SrTiO_3$–sapphire vector substrates was investigated. Epitaxial growth of such a perovskite film is not feasible on conventional sapphire c-plane substrates due to their hexagonal crystal lattice. While it is standard to use $SrTiO_3$ substrates for growing $La_{0.67}Sr_{0.33}MnO_3$ films, these substrates can introduce unwanted artifacts below the 105 K antiferrodistortive transition temperature of $SrTiO_3$,[77–82] which can affect the film's properties.

In this study, 20-nm-thick $La_{0.67}Sr_{0.33}MnO_3$ films were deposited using pulsed laser deposition (PLD) on the $SrTiO_3$–sapphire vector substrates. The growth rate on these vector substrates was comparable to that on conventional substrates, with clear RHEED oscillations indicating layer-by-layer growth (Figure 5.8a). The surface remained smooth post-deposition, and XRD 2θ-w scans, along with cross-sectional scanning transmission electron microscopy images, confirmed single-phase growth without any degradation of the $SrTiO_3$ membrane (Figure 5.8b-d). The $La_{0.67}Sr_{0.33}MnO_3$ and $SrTiO_3$ films were measured to be 20 nm and 30 nm thick, respectively, and diffraction data determined the c-axis lattice parameter of the $La_{0.67}Sr_{0.33}MnO_3$ film to be d=0.3842 nm at 300 K. This suggests that the antiferrodistortive phase transition of bulk $SrTiO_3$ and the resulting strain effects on the $La_{0.67}Sr_{0.33}MnO_3$ film are likely diminished.[83–85]

To further characterize the $La_{0.67}Sr_{0.33}MnO_3$ films, temperature-dependent magnetization measurements were carried out using vibrating sample magnetometery (Figure 5.9). These results were compared with reference $La_{0.67}Sr_{0.33}MnO_3$ films grown under identical conditions on conventional $SrTiO_3$ (001) substrates (Figure 5.9a). While the transition temperatures and magnetization values were similar regardless of the substrate type, a distinct kink at 105 K was observed in the magnetization curves of the films grown on conventional $SrTiO_3$ substrates, attributed to the substrate's structural phase transition (inset in Figure 5.9a). This kink, however, was absent in the films grown on the vector substrate, consistent with expectations based on the behavior of bulk-like $La_{0.67}Sr_{0.33}MnO_3$ films.[86]

The vector substrate concept significantly minimizes—if not completely eliminates—bulk substrate-induced measurement artifacts by employing an appropriate carrier. As shown in Figure 5.9b, the zero-field cooled magnetization of the vector-substrate-grown sample decreases rapidly below 190 K and bifurcates from the field-cooled curve is likely attributed to an increased blocking temperature in the $La_{0.67}Sr_{0.33}MnO_3$ film.[87, 88]

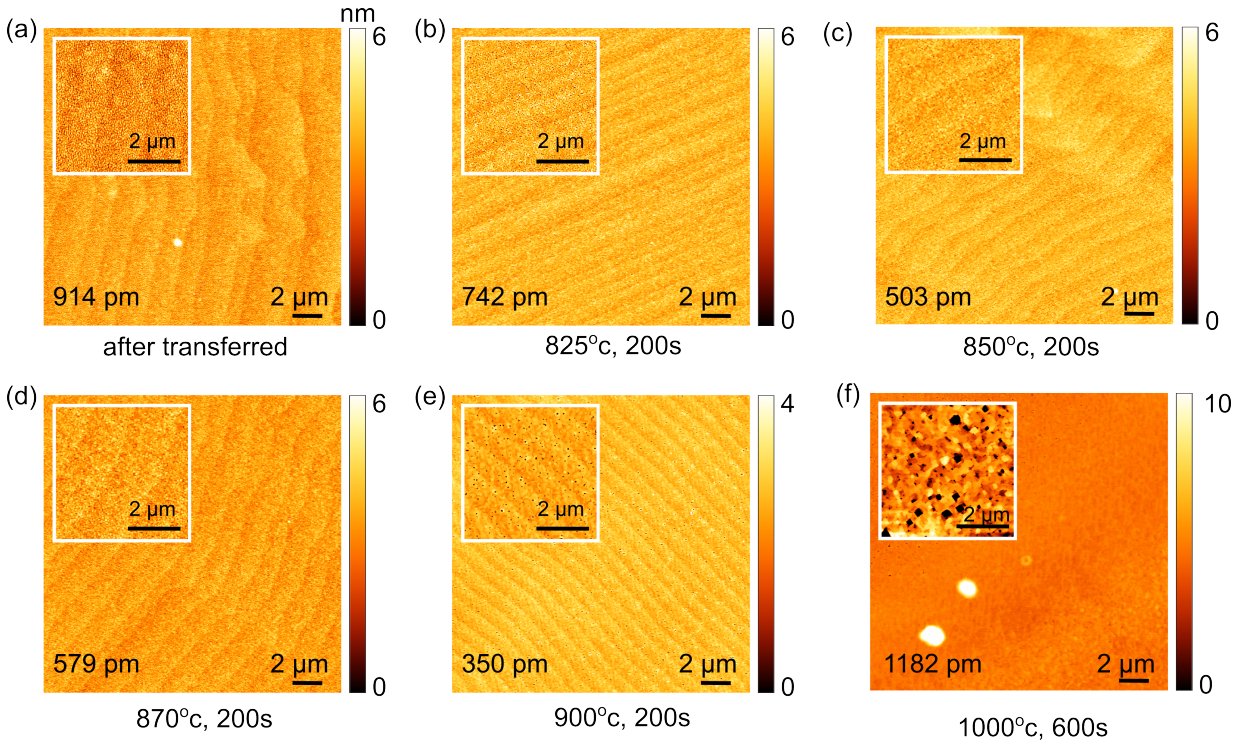

Figure 5.6: Surface morphologies of vector substrates studied by AFM after transfer and subsequent annealing at elevated temperatures under 0.1 mbar oxygen. (a) The surface of a 40-nm-thick $SrTiO_3$ film, transferred onto a sapphire substrate, exhibits broad step terraces originating from the thermally prepared sapphire substrate. (b) After annealing the transferred $SrTiO_3$ at 825 °C, the surface roughness slightly decreases. (c)–(e) Following annealing at 850 °C, 870 °C, and 900 °C, the surface reveals narrow step terraces from the $SrTiO_3$ membrane, along with the broader terraces from the underlying sapphire. (e) After annealing at 900 °C, small holes begin to form on the surface of the $SrTiO_3$ membrane. (f) At 1000 °C, these holes increase in size and depth. The sapphire substrate in (f), which was not thermally prepared, shows no wide step terraces. Reproduced with permission.[34] Copyright 2023, John Wiley and Sons.

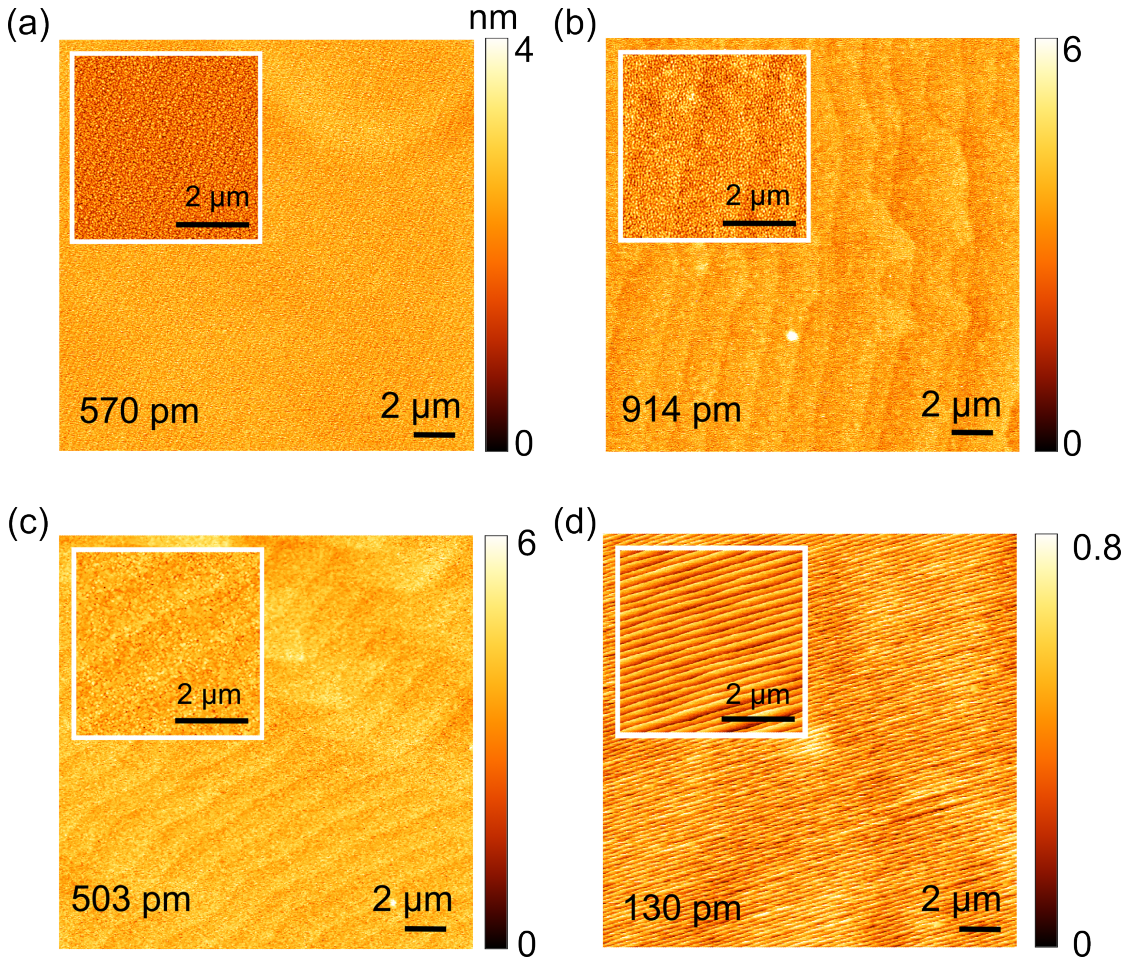

Figure 5.7: AFM images showing surface morphologies at different stages of vector substrate fabrication. a) Surface of a film–buffer bilayer (40-nm-thick $SrTiO_3$ on 10-nm-thick $Sr_2CaAl_2O_6$) deposited on a $SrTiO_3$ parent substrate. b) Surface morphology of the same $SrTiO_3$ film after being transferred onto a [0001]-oriented sapphire carrier substrate. The 1–2 µm-wide step terraces correspond to the sapphire substrate, and the transfer process caused a slight increase in surface roughness. c) An annealing step at 850 °C for 200 s in 0.1 mbar of O_2 completely restores or even slightly improves the surface quality. d) The surface of the $SrTiO_3$ parent substrate is restored after lift-off by annealing at 1100 °C for 480 s in 0.1 mbar of O_2. Reproduced with permission.[34] Copyright 2023, John Wiley and Sons.

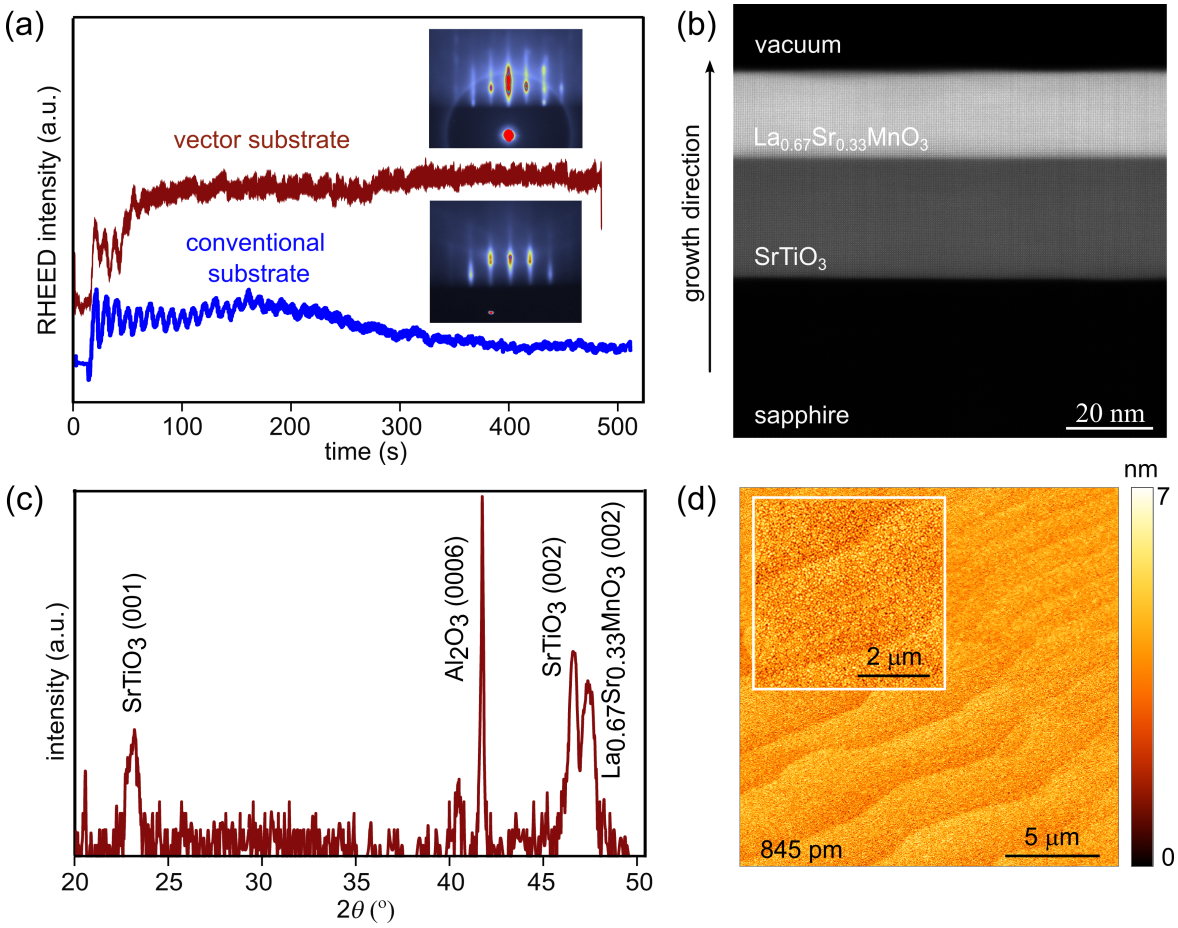

Figure 5.8: Characterization of a 20-nm-thick $La_{0.67}Sr_{0.33}MnO_3$ film deposited on a $SrTiO_3$–sapphire vector substrate. a) RHEED intensity oscillations observed during growth on the vector substrate indicate layer-by-layer growth, with deposition rates on both the conventional and vector substrates being closely matched. b) A wide-area cross-sectional scanning transmission electron microscopy image of the $La_{0.67}Sr_{0.33}MnO_3$ film deposited on the $SrTiO_3$–sapphire vector substrate shows clean interfaces at both the sapphire-$SrTiO_3$ and $SrTiO_3$–$La_{0.67}Sr_{0.33}MnO_3$ boundaries. Since the $SrTiO_3$ membrane's zone axes are misaligned with the sapphire carrier, the sapphire lattice is not visible when the $SrTiO_3$ and $La_{0.67}Sr_{0.33}MnO_3$ lattices are resolved, and vice versa. c) XRD 2θ-w scan of the $La_{0.67}Sr_{0.33}MnO_3$ film shows single-phase growth, with distinct peaks from the $SrTiO_3$ membrane, demonstrating the stability of the vector substrate during epitaxial thin-film growth. d) The surface morphology of the $La_{0.67}Sr_{0.33}MnO_3$ film imaged by AFM shows a surface roughness of less than 1 nm. Reproduced with permission.[34] Copyright 2023, John Wiley and Sons.

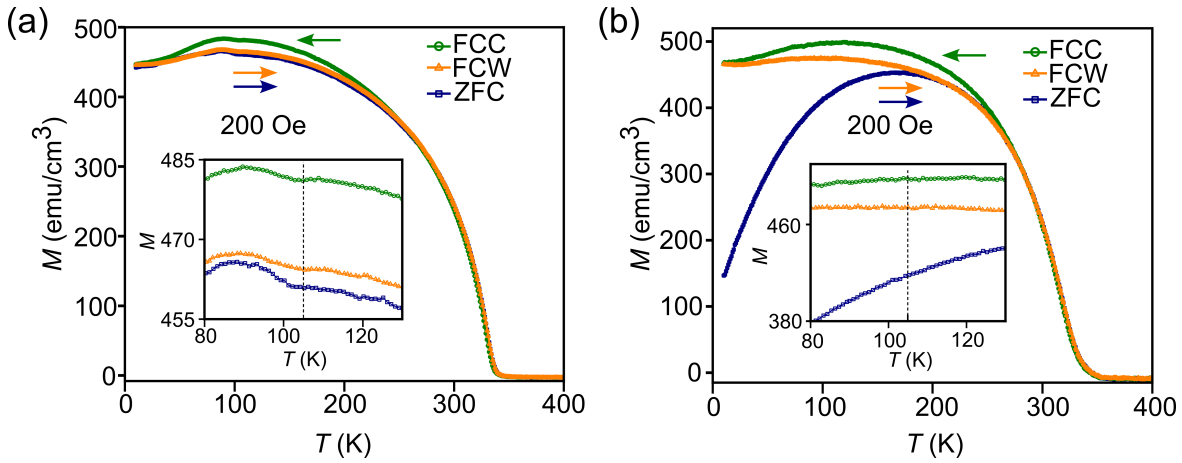

Figure 5.9: a) Magnetization curves measured as a function of temperature for a $La_{0.67}Sr_{0.33}MnO_3$ film grown on a conventional $SrTiO_3$ substrate. The curves include FCC (field-cooled cooling), FCW (field-cooled warming), and ZFC (zero-field-cooled cooling) measurements. These data reveal that the magnetization is influenced by the antiferrodistortive phase transition of $SrTiO_3$ at 105 K. This structural transition in the $SrTiO_3$ film alters the intrinsic magnetization behavior of $La_{0.67}Sr_{0.33}MnO_3$, producing a distinct kink in the magnetization-temperature curve at the transition temperature (inset). b) Magnetization curves for a $La_{0.67}Sr_{0.33}MnO_3$ film grown on a $SrTiO_3$–sapphire vector substrate, showing FCC, FCW, and ZFC data. The magnetization evolves smoothly with temperature, with no distortion or kink observed at 105 K, indicating the absence of interference from the structural transition (inset). This image was made by Varun Harbola. Reproduced with permission.[34] Copyright 2023, John Wiley and Sons.

5.5 Conclusion and outlook

In summary, the concept of vector substrates has been introduced as a novel approach to substrate fabrication. The idea is rooted in the understanding that while only the thin surface layer of a substrate is crucial for film growth, the bulk of the substrate significantly influences physical properties and cost, despite serving basic functions. To address this, substrates were fabricated by transferring a membrane-like template layer, grown on a reusable parent substrate, onto a carrier substrate. This allows for the independent selection and optimization of the template layer and the carrier substrate.

To test the viability of this technology, vector substrates were fabricated using sapphire carriers coated with single-crystalline (001)-oriented $SrTiO_3$ membranes, with the parent substrates reused multiple times. The vector substrates were characterized, and high-quality epitaxial $La_{0.67}Sr_{0.33}MnO_3$ films were successfully grown on them. These films did not exhibit the artifacts commonly observed in films grown on conventional $SrTiO_3$ substrates. Chapter 6 will discuss bicrystal vector substrates in detail, focusing on the use of bicrystalline membrane transfer onto alternative carriers. This approach reduces both the reliance on traditional bicrystal substrates and the cost.

Only limited time has been able to be invested in scaling up the substrates, initial studies therefore produced vector substrates of up to $4.5 \times 4.5\,mm^2$ in size. For commercial applications, increasing the substrate size and automating the fabrication process are essential future goals that have yet to be realized. However, the current substrate sizes are sufficient for many fundamental thin-film studies, and experiments can be tailored to fit within these smaller areas.

In conclusion, vector substrates provide a valuable alternative to conventional substrates. By eliminating the need for single-crystal growth, this technology enables researchers and manufacturers with thin-film deposition capabilities to create optimized substrates for a wide range of applications.

Chapter 6

Vector-substrate-based Josephson junctions

A novel method for fabricating bicrystal Josephson junctions of high-T_c cuprate superconductors that are not grown on bulk bicrystalline substrates is introduced. Utilizing vector substrate technology, this novel approach employs bicrystalline membranes that are only a few nanometers thick, which are then transferred onto conventional substrates. Josephson junctions with 24° [001]-tilt $YBa_2Cu_3O_{7-x}$ grain boundaries fabricated on sapphire single crystals by utilizing 10-nm-thick bicrystalline $SrTiO_3$ membranes are demonstrated.

This technique enables the fabrication of bicrystalline Josephson junctions of high-T_c superconductors on a large variety of bulk substrate materials, offering novel degrees of freedom in the design and optimization of junctions and their electronic properties. Additionally, this method replaces the traditional need for bulk bicrystalline substrates with thin-film growth methods.

This work presented in this chapter has been published in Ref. [89]. The text I use in the following chapter has been taken largely from Ref. [89], with only minor modifications. Scientific conceptualization of the project was led by V. Harbola, J. Mannhart, K. Wurster, R. Kleiner, D. Koelle, and me. Planning of the experiment was performed by V. Harbola, J. Mannhart, M. Hack, K. Wurster, S. Koch, R. Kleiner, D. Koelle, and me. Bicrystal vector substrate fabrication was conducted by V. Harbola and me. $YBa_2Cu_3O_{7-x}$ film growth was performed by V. Harbola and me. Micro patterning was carried out by M. Hack, K. Wurster, and S. Koch. Transport measurements were implemented by M. Hack, K. Wurster, S. Koch, V. Harbola, and me. Analysis of the data was carried out by V. Harbola, M. Hack, K. Wurster, S. Koch, and me. Writing was performed by V. Harbola, M. Hack, K. Wurster, J. Mannhart, and me. All authors contributed to the scientific discussion.

6.1 Introduction

Bicrystal Josephson junctions of high-transition-temperature (high-T_c) cuprate superconductors[90–93] have found many uses in fundamental science and applications.[91, 94–96] For example, bicrystal and the related tricrystal junctions have been instrumental in identifying the *d*-wave order-parameter symmetry of high-T_c cuprates.[97, 98] Studies of their critical currents as a function of the grain boundary angle revealed that the necessity of aligning the grains in high-T_c cables and/or utilizing large grain boundary areas[98] to achieve high critical currents, as is now done in coated conductor technologies (see, e.g., Refs.[99, 100]).

Bulk bicrystalline substrates are required for bicrystal Josephson junctions for the epitaxial growth of bicrystalline high-T_c superconducting thin films. However, such substrates are costly to produce, limited in material options and may possess properties undesirable for certain applications. Sapphire, for example, features a low dielectric loss tangent of $<10^4$ at 10^{10} Hz and 300 K, high thermal conductivity of $\approx$35 W/mK at 300 K, and a moderate dielectric constant of $\approx$10. It therefore appears to be a desirable material for substrates of high-T_c Josephson junctions.[101] However, because of its hexagonal crystal lattice symmetry, its poor lattice match, and its contamination of high-T_c films by Al diffusion, sapphire is not generally considered a useful material for bicrystals.

A new approach called vector substrate technology[34] has been developed in the context of this thesis, as discussed in chapter 5, that builds on advances based on the fabrication[17, 18, 25, 28, 30, 102, 103] and application[14, 15, 19, 29, 35, 104–106] of freestanding oxide membranes and offers new degrees of freedom in choosing substrates for the epitaxial growth of thin films.[34, 106] This allows for the use of low-cost or application-specific materials as carrier.

6.2 Idea and concept

Given its many advantages, the vector substrate technology has been proposed as an alternative to bicrystalline bulk substrates by making use of bicrystalline membranes[34], as illustrated in Fig. 6.1a. Our work shows the successful realization of this concept by demonstrating excellent bicrystalline $YBa_2Cu_3O_{7-x}$ Josephson junctions fabricated on standard *c*-plane sapphire single crystals. In this demonstration, the surfaces of the sapphire substrates are coated by 10-nm-thick $SrTiO_3$ membranes. These membranes are produced by thin-film growth on bicrystalline substrates, referred to as parent substrates, which can be recycled to grow numerous additional membranes.

To fabricate bicrystalline $YBa_2Cu_3O_{7-x}$ Josephson junctions on sapphire single crystals, $SrTiO_3$ bicrystals[107] as parent substrates were used. On such a parent substrate, a water-soluble, sacrificial $Sr_2CaAl_2O_6$ layer[15, 22] and a $SrTiO_3$ layer were epitaxially deposited by pulsed laser deposition (PLD), such that the bicrystal structure was transferred through the sacrificial layer to the final $SrTiO_3$ membrane. By dissolving the sacrificial layer in water, the bicrystal $SrTiO_3$ membrane was then lifted-off and transferred onto a carrier substrate, in our case a sapphire single crystal, yielding a vector substrate. In this process, illustrated in Figure 6.1b, the surface structure of the bicrystal parent substrate remains unscathed. The parent substrates are therefore reusable, such that numerous membranes can be derived from one parent substrate (Figure 6.2). Furthermore, vector substrates fabricated in this way may also serve as parent substrates, reducing the overall need for bulk bicrystals completely.

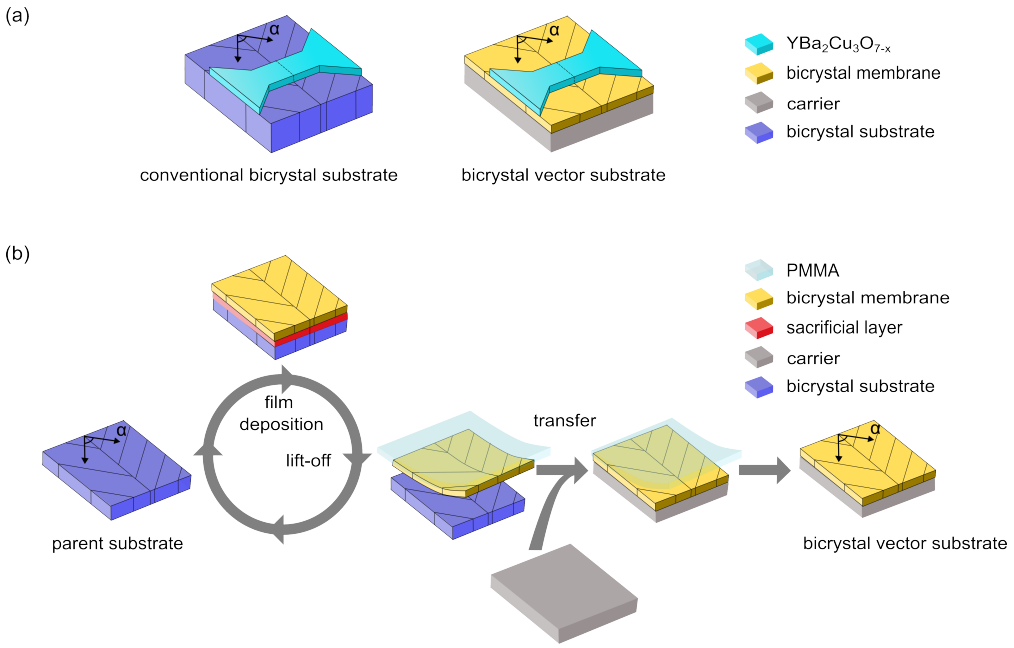

Figure 6.1: (a) Conceptual illustration of the main idea of this study. Left: schematic of a bicrystalline Josephson junction created through epitaxial growth on a conventional bicrystalline bulk substrate. Right: schematic of a bicrystal arrangement using a vector substrate. The vector substrate which consists of a bulk substrate of almost unrestricted choice, here it is a sapphire single crystal, carries a bicrystalline thin-film membrane sintered to its surface, here a 10-nm-thick, 24° $SrTiO_3$ bicrystalline film. High-T_c superconducting film grown on either type of substrate yield Josephson junctions at the bicrystal grain boundary. (b) Depiction of the vector substrates fabrication process. Note that the parent substrates can be reused multiple times. Here α equals ~24°. Reproduced under terms of the CC-BY license.[89]

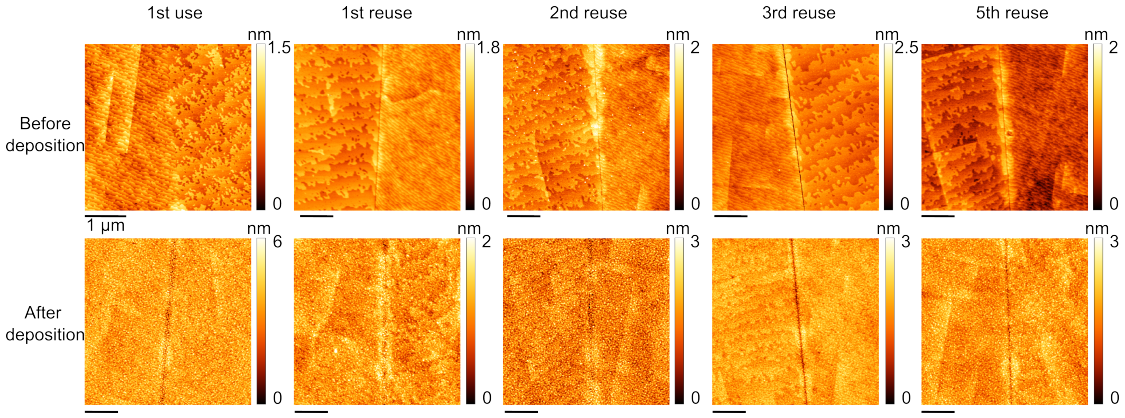

Figure 6.2: Evolution of the surface morphology when reusing the parent $SrTiO_3$ bicrystal substrate. The bicrystal grain boundary remains clearly preserved upon substrate reuse after the membrane is lifted-off. There is a slightly more pronounced diffusion of material near and at the grain boundary resulting in a sub-nanometer trench appearing even after the first reuse and evolving with subsequent reuse (top row). Bottom row shows the surface morphology after the deposition of the sacrificial layer and thin film on top of the parent substrate. Notably, even after the 5th reuse, the substrate surface is still viable for epitaxial growth. Reproduced under terms of the CC-BY license.[89]

6.3 Microscopical studies of bicrystal vector substrate during fabrication

The fabrication of the sample began by thermally preparing 24° [001]-tilt $SrTiO_3$ bicrystals[107]. This was achieved through an *in situ* anneal in $P(O_2)$= 0.1 mbar at 825°C for 40 min, resulting in surfaces exhibited standard step-terrace patterns and well visible boundaries between the two constituent crystals (Figure 6.3). Following this, the layer-by-layer growth of $Sr_2CaAl_2O_6$—this material having been selected for its lattice match to $SrTiO_3$—by PLD, $SrTiO_3$ layers were also grown layer-by-layer by PLD (see Chapter 3.1). Both the $Sr_2CaAl_2O_6$ layer and the $SrTiO_3$ membranes were 10 nm thick, optimized for large-area membrane lift-off and effective disolving.

The surfaces of the parent substrates were restored through cleaning and annealing, which once again reveal the distinct step-terrace features (Figure 6.2). The parent substrates were reused up to five times without encountering the end of their lifetime. Note, however, that although the surfaces of the parent bicrystal substrate can be completely restored, the bicrystal grain boundaries may experience some reconstruction due to the high temperatures used during film growth and annealing. This can lead to a sub-nanometer trench that develops along the boundary during subsequent preparations (Figure 6.2).

Although the fragile grain boundary sections of the membranes remained intact after the transfer, the outer parts of the membranes always became fragmented. As a result, the bicrystal membranes exhibit variable shapes with areas of several mm^2 (Figure 6.4).

To prepare the vector substrate surface and remove contaminants still present between the sapphire substrates and the $SrTiO_3$ membranes and to enhance the bonding between the membranes and the sapphires, a 825°C, 40-min anneal in $P(O_2)$= 0.1 mbar was also performed on these samples.[34, 108] The membrane surfaces smoothly bulged upward by ∼20 nm over a length perpendicular to the boundary of ∼2×200 nm, which can be attributed to relaxation of strain present between the two $SrTiO_3$ grains. Otherwise the surfaces were found to be flat and smooth, suitable for subsequent epitaxial growth. The bulging was observed each time a bicrystal membrane was transferred, and found to persist after annealing. The amplitude of the bulging was so small that it never interfered with subsequent epitaxial deposition. Figure 6.3 provides a series of AFM micrographs that illustrate the evolution of the sample surface during its fabrication.

These results reveal that it is possible to grow heterostructures consisting of a bicrystalline substrate and several layers of thin films, in which the grain boundary is copied from the substrate into each layer. It is even possible to do so in case one of the layers, like the $Sr_2CaAl_2O_6$ film in this study, has a non-perovskite structure. Furthermore, the results show that bicrystalline membranes are sufficiently robust to allow them to be lifted-off and transferred.

6.4 $YBa_2Cu_3O_{7-x}$ deposition and Josephson junction

In the following step, $YBa_2Cu_3O_{7-x}$ films, approximately 100 nm thick, were epitaxially grown on the bicrystalline $SrTiO_3$ surface by PLD using standard growth parameters (see Chapter 3.1). The bulge at the grain boundary became unnoticeable after the $YBa_2Cu_3O_{7-x}$ deposition. The film surfaces exhibited precipitates (Figure 6.3e), which likely arose due to a non-stoichiometric transfer of material from the PLD target to the

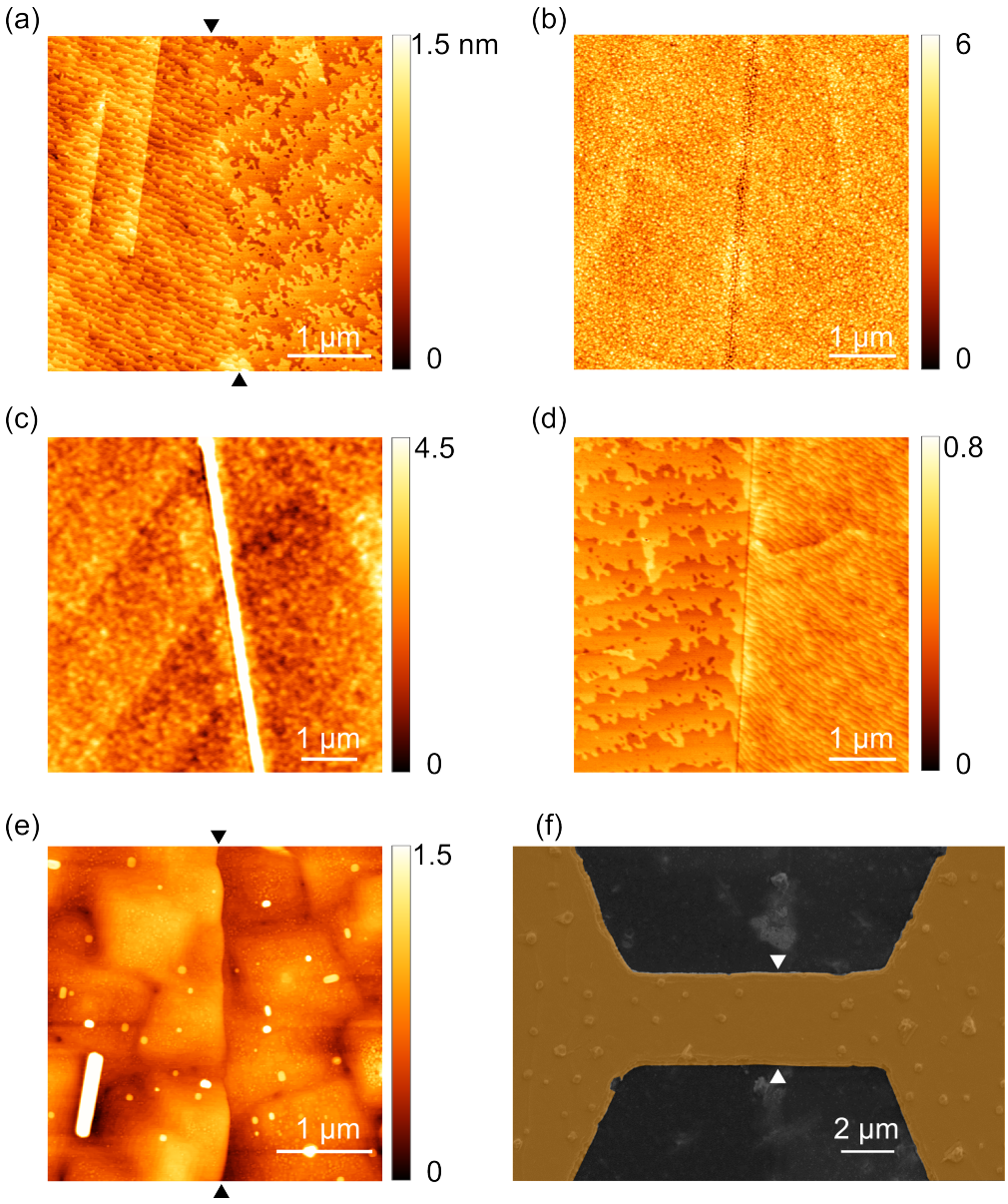

Figure 6.3: (a)–(e) AFM micrographs showing the sample surfaces at various stages of preparation. (a) Surface of a bicrystal parent substrate after being terminated at 825°C for 40 min. (b) Surface morphology following the growth of $Sr_2CaAl_2O_6$ layers with a $SrTiO_3$ membrane on top. (c) The same bicrystal $SrTiO_3$ membrane after transfer onto a *c*-plane sapphire and subsequent annealing at 825°C for 40 min. (d) Surface morphology of the parent bicrystal substrate after membrane lift-off, cleaning and preparation for reuse. (e) Grain boundary after deposition of $YBa_2Cu_3O_{7-x}$ on a bicrystal vector substrate. (f) Scanning electron microscopy image of a $YBa_2Cu_3O_{7-x}$ microbridge crossing the 24° [001]-tilt bicrystal boundary of the vector substrate, which forms a Josephson junction. Arrows indicate grain boundary positions in (a), (e) and (f). Reproduced under terms of the CC-BY license.[89]

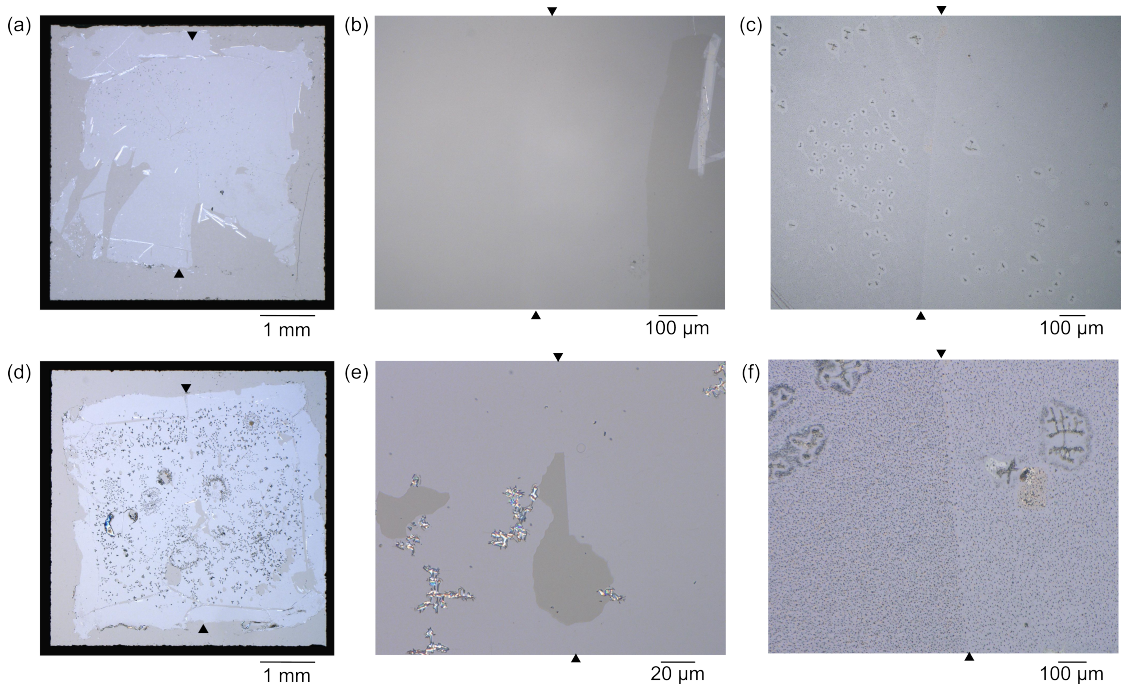

Figure 6.4: Optical microscopy images of two different bicrystal $SrTiO_3$-on-sapphire vector substrates derived from the same parent substrate. (a) and (d) show the full vector substrates on 5x5 mm^2 sapphire carriers. (b) and (e) provide closer views of the grain boundary areas of the vector substrates, where the grain boundary is not optically visible. However, in (e), the membrane fracture of the membrane can be seen to occur precisely at the grain boundary, indicating its location. By comparing (d) and (e), what looks like contaminations in (d) is actually the wrinkling of the bicrystal membrane upon this transfer, as apparent in (e). (c) and (f) show images taken after the deposition of ∼100 nm $YBa_2Cu_3O_{7-x}$ on these vector substrates, where the bicrystal boundary becomes clearly visible. Arrows mark the grain boundary positions in all images.

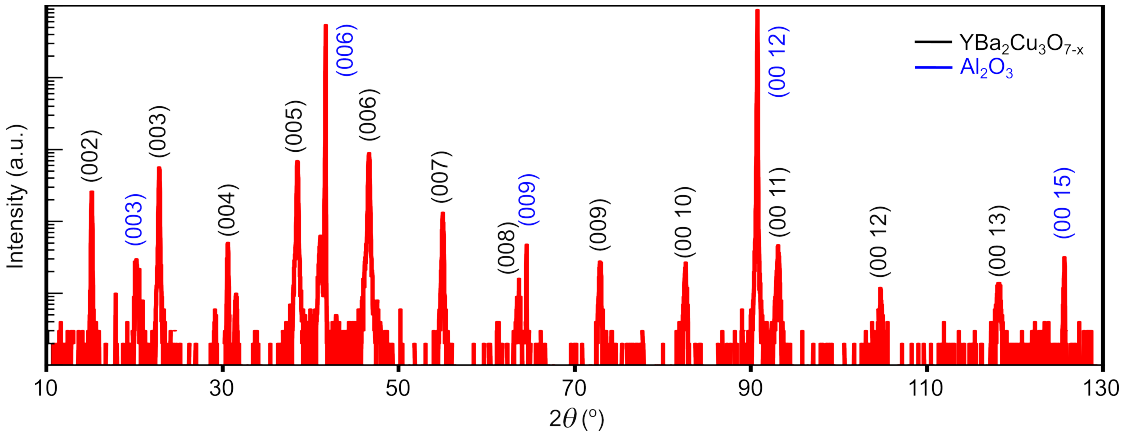

Figure 6.5: A 2θ-w X-ray diffraction scan of $YBa_2Cu_3O_{7-x}$ deposited on a bicrystal $SrTiO_3$-on-sapphire vector substrate. The scan reveals that a single-phase growth of $YBa_2Cu_3O_{7-x}$ occurs, with peaks corresponding to $YBa_2Cu_3O_{7-x}$ on $SrTiO_3$ (001) clearly identified. The $SrTiO_3$ peaks are not visible due to the 10 nm thickness of the $SrTiO_3$ layer, compared to the ∼100 nm thickness of the $YBa_2Cu_3O_{7-x}$ layer.

growing film. Despite this, X-ray diffraction confirmed that the films were predominantly single-phase and c-axis oriented, consistent with $YBa_2Cu_3O_{7-x}$ films grown on standard single-crystallline $SrTiO_3$ substrates (Figure 6.5).[109] Their intragrain superconducting $T_{c,0}$ equaled ∼88 K. To create ∼3–4-µm-wide superconducting bridges crossing the grain boundary as desired to fabricate the Josephson junctions, the samples were patterned using optical lithography. The patterning involved depositing a ∼20-nm-thick Au film on the sample followed by lithography, gold etching and Ar-ion milling. The samples remain resilient throughout each stage of the fabrication process. A scanning electron microscopy image of a typical sample is shown in Figure 6.3f.

6.5 Josephson junctions transport properties

The patterning and the analysis of the bridges were done by the Physikalisches Institut, Center for Quantum Science (CQ) and LISA+ at the University of Tübingen. The transport properties of the bridges were obtained using 4-point measurements conducted at 4.2 K in an electrically and magnetically shielded environment with an external magnetic field applied perpendicular to the substrate plane. Figure 6.6 provides the current–voltage $I(V)$ characteristics for two nominally identical bridges under the influence of the magnetic field. Both bridges demonstrate textbook-like $I(V)$ characteristics, as described by the resistively and capacitively shunted junction (RCSJ) model.[110, 111] The critical currents I_c at $H = 0$ equal ∼116 and 159 µA, corresponding to critical current densities J_c ∼5×10^4 A/cm^2, respectively. These I_c values were measured after the samples had been kept at 300 K for several months. Immediately after fabrication, they were a factor of about 3–5 smaller (Figure 6.7). This enhancement is attributed to relaxation of oxygen ions at the grain boundary[91], a phenomenon also observed in Josephson junctions fabricated on bulk bicrystalline substrates.[112] The normal state resistance R_n of the junctions shunted by the 18-nm-thick Au layer were calculated to be 7.1 and 5.4 Ω. The calculated I_cR_n products for the two bridges are 820 and 850 µV, in agreement with literature values of ∼300 µV for similarly shunted 24° junctions.[113, 114] The full data set of Figure 6.6 is shown in Figure 6.8. Fitting the $I(V)$ characteristics to the RCSJ model yields a Stewart–McCumber parameter of β_c ∼1.7 (see

Figure 6.11), which aligns with the expected value of $\beta_c \sim 2.5$ resulting from a stray capacity of $\sim 0.15\,\mathrm{pF}$ possibly caused by the huge low-temperature dielectric permittivity of $SrTiO_3$.[115] The $I_c(H)$ characteristics (Figure 6.9) reveal a notably homogeneous current density and high-quality junctions. The temporal evolution of $I_c(H)$ is shown in Figure 6.10.

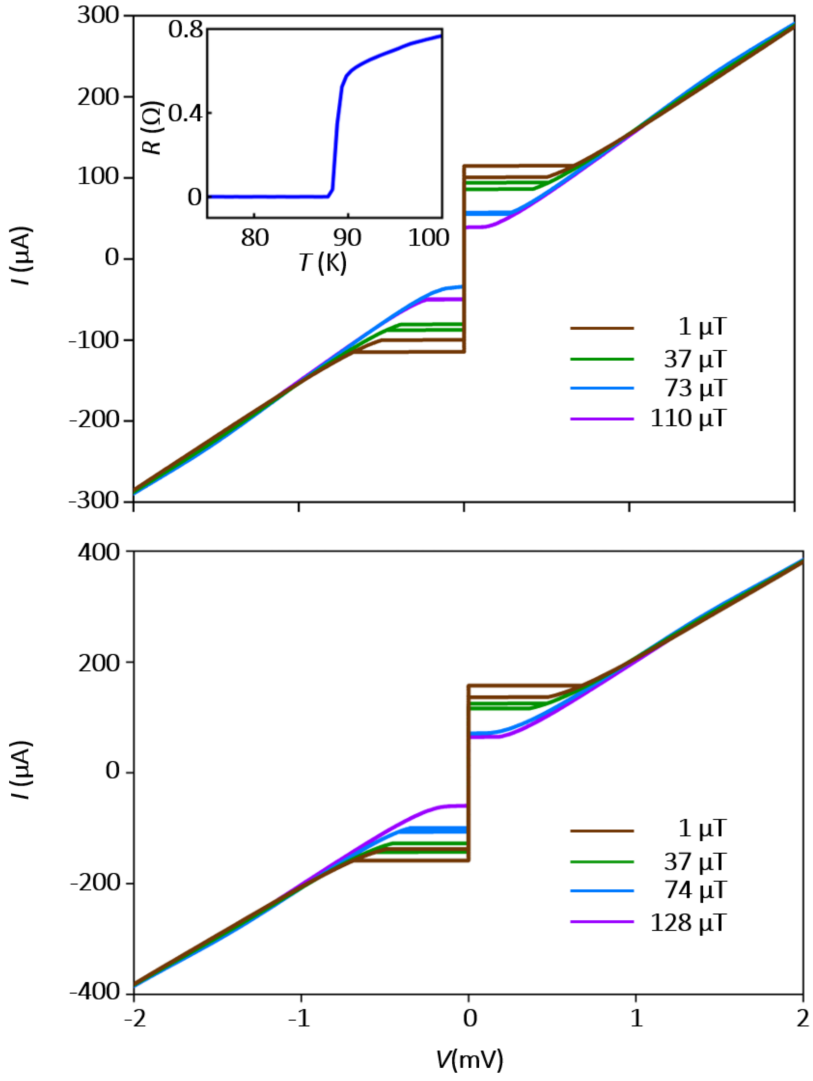

Figure 6.6: Current–voltage characteristics of the 24° bicrystal Josephson junctions, nominally identical and fabricated using vector substrate technology. Measurements were taken at 4.2 K with a magnetic field H applied perpendicular to the sample surfaces, as described. The observed characteristics conform to RCSJ behavior (refer to Figure 6.11). Inset in the upper graph: Intragrain $R(T)$ characteristic of a nominally identical sister sample. The characterizations were conducted by Martin Hack. Reproduced under terms of the CC-BY license.[89]

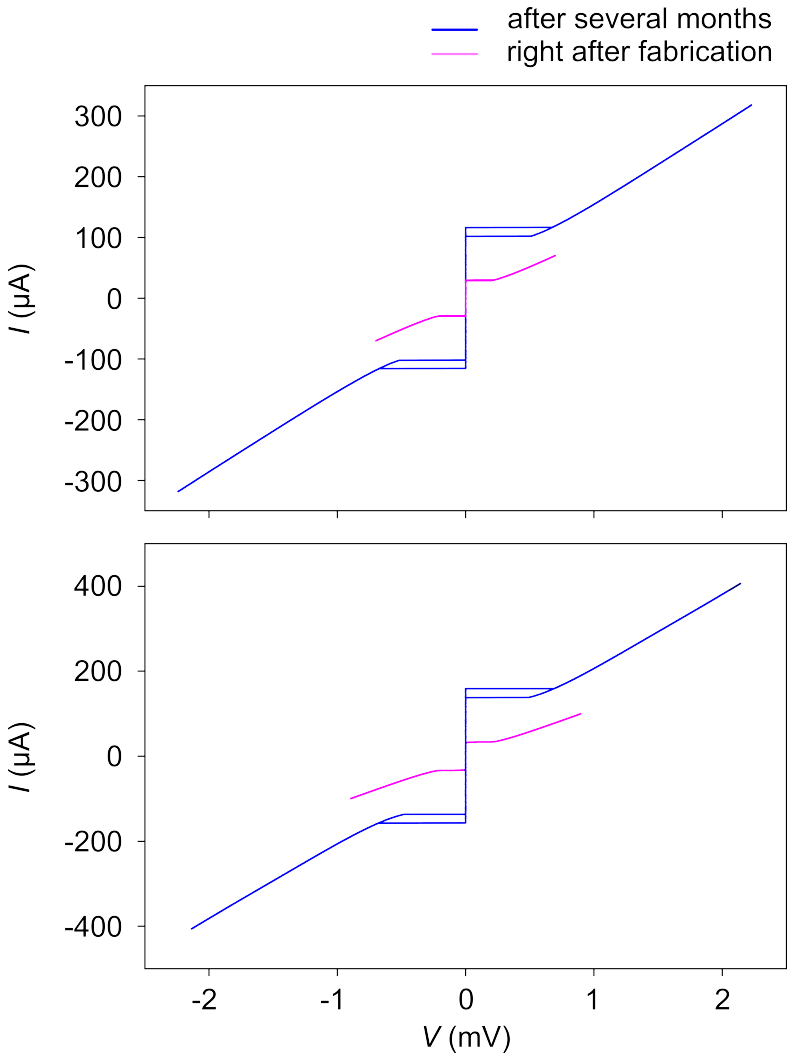

Figure 6.7: Temporal evolution of the $I(V)$ characteristics of the Josephson junctions shown in Figure 6.6. Both junctions were measured right after fabrication and after several months of storage in a nitrogen atmosphere. A significant improvement in the I_c is observed, about a factor of about five in both junctions. Additionally, a more pronounced hysteresis in the I-V sweep is evident, indicative of an increased Stewart-McCumber parameter. This "healing" effect of the Josephson junctions is likely due to the relaxation of oxygen ions at the grain boundary over time. The characterizations were conducted by Martin Hack. Reproduced under terms of the CC-BY license.[89]

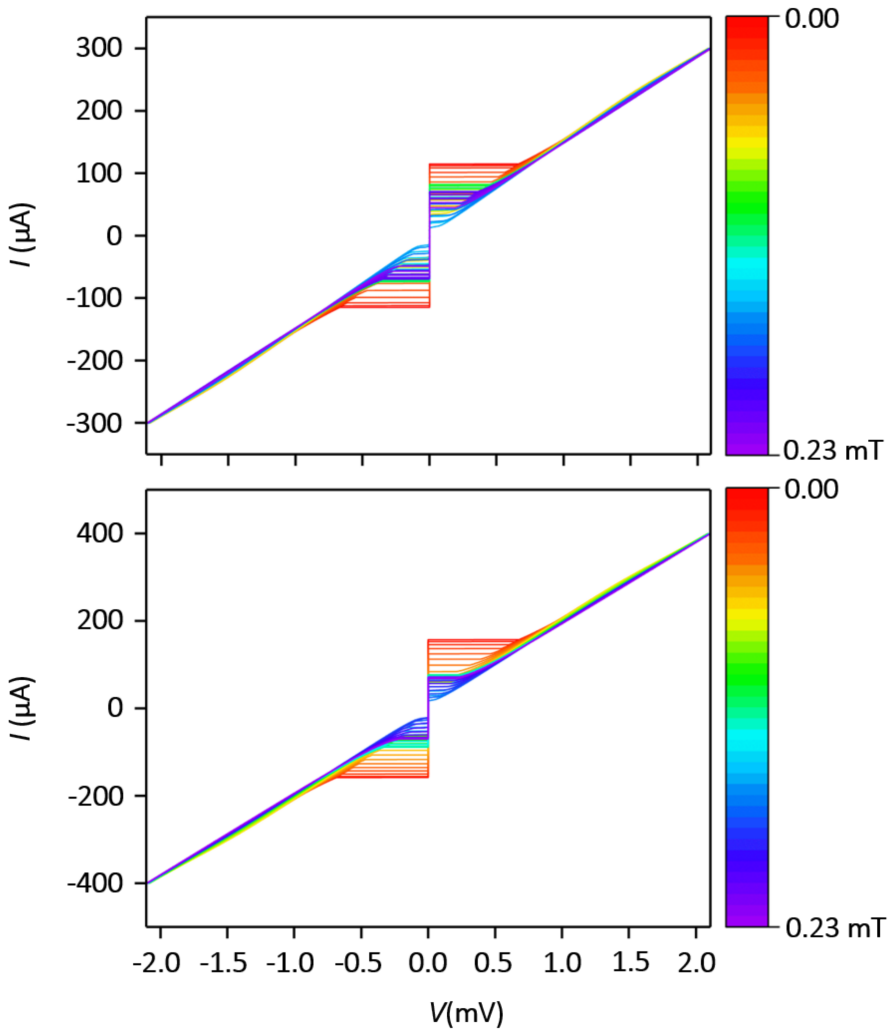

Figure 6.8: The complete dataset of the Josephson junction characteristics shown in Figure 6.6. Electric-transport characteristics of $YBa_2Cu_3O_{7-x}$ grain boundary Josephson Junctions fabricated using the vector substrate technology. The dataset features multiple current vs voltage measurement taken at external magnetic fields varying from 0 to 0.23 mT applied perpendicular to the grain boundary. For clarity, only one direction of the current sweep is shown here. The characterizations were conducted by Martin Hack.

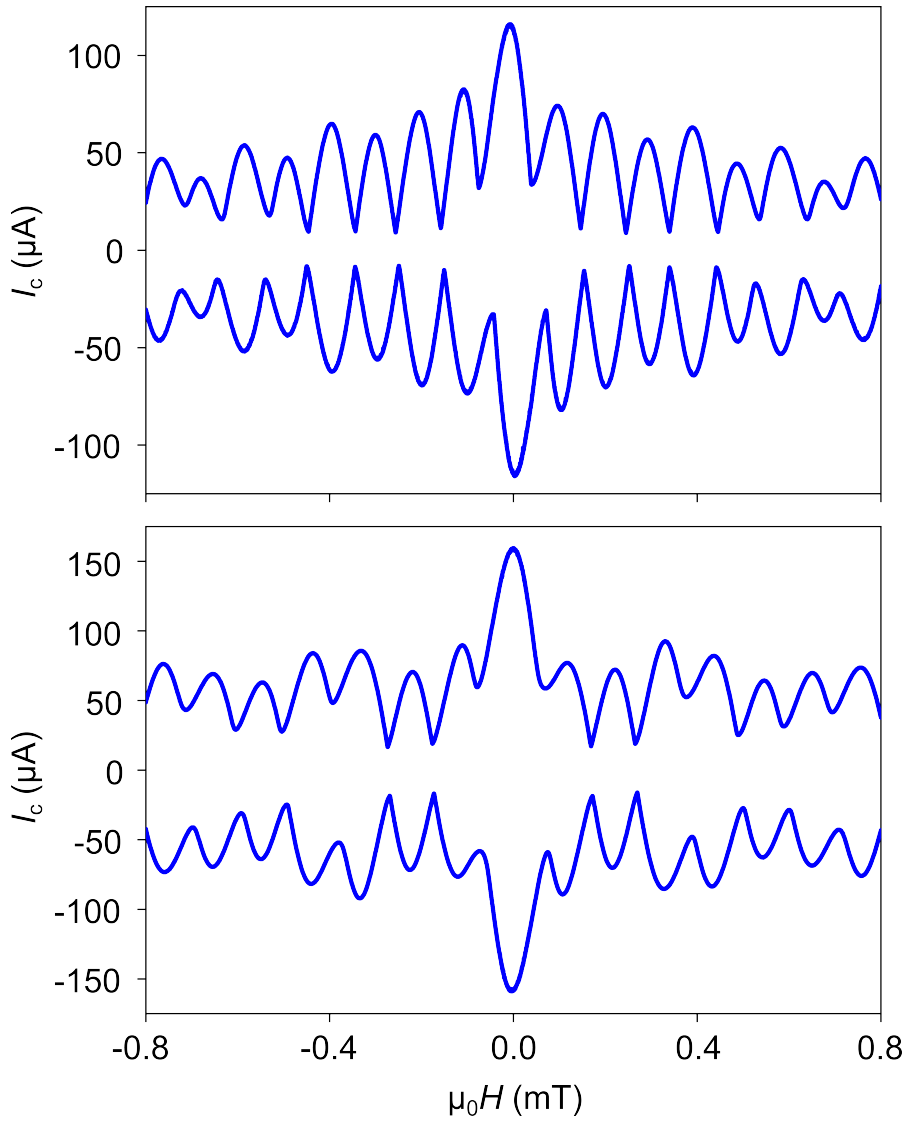

Figure 6.9: $I_c(H)$ characteristics of the two Josephson junctions from Figure 6.6 , measured at 4.2 K with the magnetic field H applied perpendicular to the sample surface. The characterizations were conducted by Martin Hack. Reproduced under terms of the CC-BY license.[89]

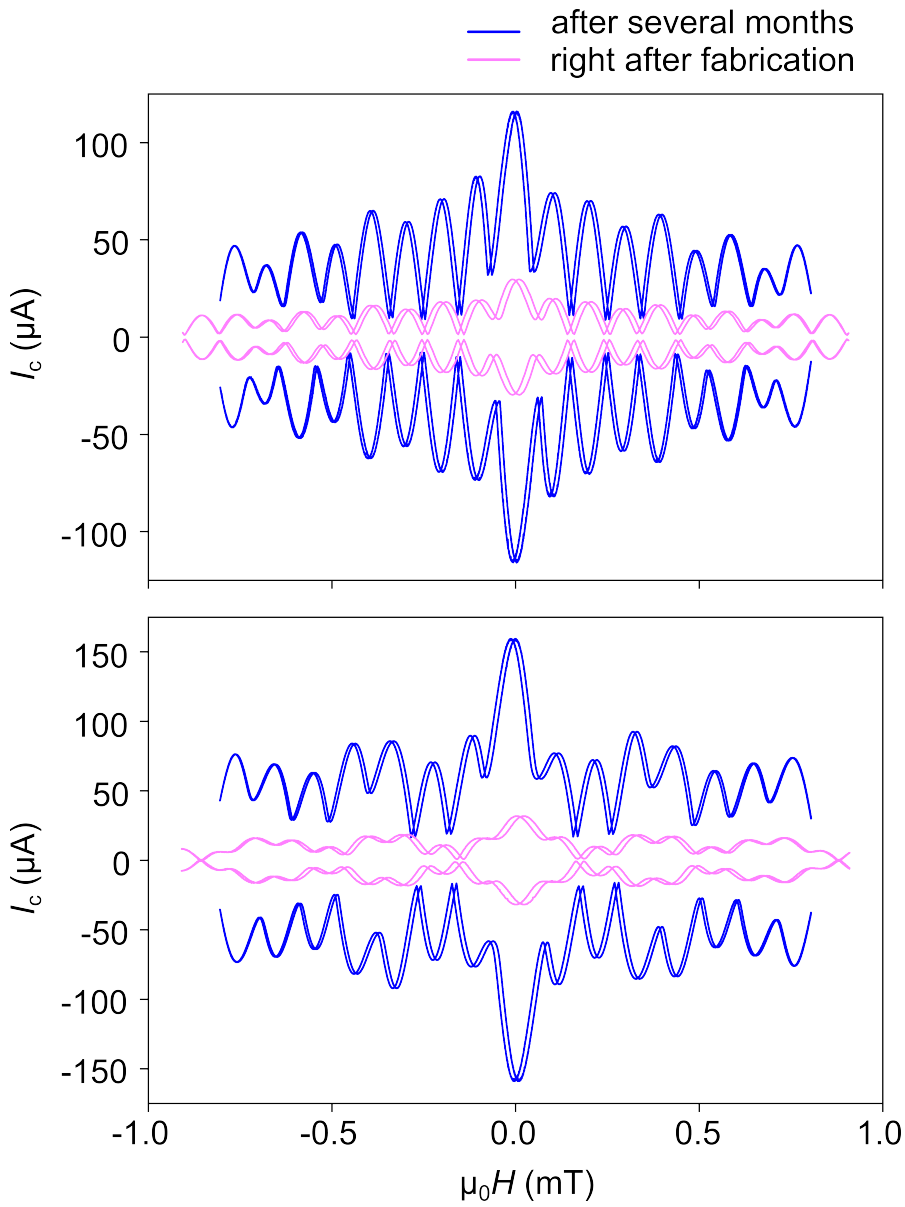

Figure 6.10: Temporal evolution of $I_c(H)$ of the two Josephson junctions shown in Figure 6.7. While the shape of the I_c oscillations remains consistent over time, there is an overall increase in I_c by about a factor of five applies also for the small magnetic fields under which the Josephson junctions were characterized after a span of several months. The characterizations were conducted by Martin Hack. Reproduced under terms of the CC-BY license.[89]

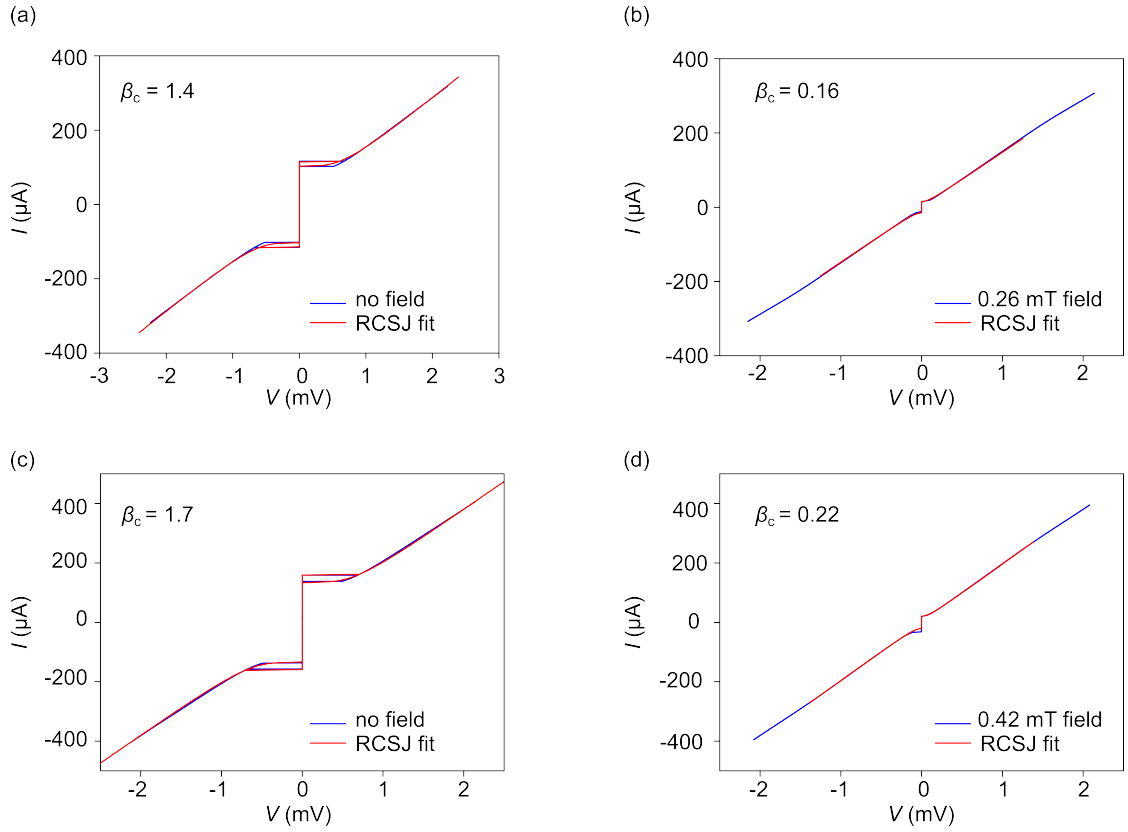

Figure 6.11: Electric-transport characteristics of the two Josephson junctions shown in Figure 6.6. The current (I) vs voltage (V) measurements are compared to RCSJ fits to determine β_c of the Josephson junctions. (a) and (b) show the I-V characteristics of the junction in Figure 6.6 a at external fields of 0 and 0.26 mT, respectively. The comparison with the fit yield β_c values of 1.4 and 0.16, respectively. (c) and (d) display the I-V characteristics of the junction shown in Figure. 3b at external fields of 0 and 0.42 mT, respectively, with corresponding β_c of 1.7 and 0.22. The calculations were conducted by Reinhold Kleiner.

6.6 Conclusion and outlook

In summary, the process described in this chapter employs membranes of bicrystalline films, which are fabricated through thin-film growth techniques and then transferred onto chosen substrates. This technique minimizes the need for bicrystalline substrates to grow bicrystal Josephson junctions, and it enables the growth of such junctions on bulk substrates of choice, which are only coated with a ∼10-nm-thick bicrystalline layer suitable for epitaxial growth. Furthermore, this technology offers the potential to (i) fabricate further vector substrates, including tricrystalline or polycrystalline substrates, (ii) grow bicrystalline films of other, possibly non-superconducting materials, and (iii) deposit heterostructures that comprise single-crystalline films on top of bicrystal layers.

Chapter 7

Interface design beyond epitaxy: Oxide heterostructures comprising symmetry-forbidden interfaces

Epitaxial growth of thin-film heterostructures is typically considered the most effective method for achieving high-quality structural and electronic interfaces between three-dimensional materials. However, this technique is limited to materials with matching crystal symmetries and lattice constants. We introduce a new category of interfaces created using a membrane-based fabrication method that bypasses the need for epitaxial growth, thus overcoming these limitations. By utilizing the additional degrees of freedom this method provides, we demonstrate atomically clean interfaces between three-fold symmetric sapphire and four-fold symmetric $SrTiO_3$. Atomic-resolution imaging reveals structurally well-defined interfaces featuring a novel moiré-type reconstruction.

The work presented in this chapter has been published in Ref. [108]. The text I use in the following chapter has been taken largely from Ref. [108], with appropriate modifications. Scientific conceptualization of the project was led by H. Wang, V. Harbola, J. Mannhart, and P. A. van Aken. Planning of the experiment was conducted by V. Harbola, H. Wang. Sample fabrication was carried out by V. Harbola and me. Scanning Transmission Electron Microscopy measurements were conducted by H. Wang. Analysis of the data was implemented by V. Harbola, H. Wang. Writing was performed by V. Harbola, H. Wang, J. Mannhart, and P. A. van Aken. All authors contributed to the scientific discussion.

7.1 Introduction

Interfaces are essential for generating emergent electronic behaviors distinct from the adjacent materials. Interface-engineered devices like LEDs, solar cells, and transistors have revolutionized technology. Atomic-scale interface engineering is a vital research area[13, 116–118], leading to discoveries such as quantum Hall effects[1, 2], giant magnetoresistance[5], and interfacial superconductivity[119]. While epitaxial growth has been the primary method for fabricating high-quality 3D material interfaces between three-dimensional (3D) materials consisting of strongly bounded 3D lattices, it is limited to materials with compatible crystal symmetries and lattice parameters[30, 120, 121].

Mechanical stacking, a non-epitaxial method, has been successful for 2D materials, allowing for various twist angles and combinations of different materials[122]. This stacking method has led to groundbreaking discoveries[123, 124],including superconductivity, moiré excitons, interlayer magnetism, and moiré ferroelectricity.[125–131] The success of 2D material stacking suggests the potential for new processes to overcome epitaxial restrictions in 3D material interfaces. The roughness of 3D materials makes it challenging to stack them for effective macro-scale bonding.[122]

Recent advances in fabricating and transferring single-crystalline 3D material membranes[15, 16, 18, 19, 21, 24, 31, 132–137] have produced clean enough interfaces for electronic applications.[138] Twisting and stacking of these membranes have successfully formed moiré patterns[14, 105, 139, 140]. However, current technologies face limitations in creating atomically clean and sharp interfaces due to contamination during liquid processing of membrane fabrication.[28] Figure 7.1a shows a typical cross-sectional micrograph of an interface prepared with state-of-the-art methods, revealing a ∼1.5-nm-thick contamination layer that impedes direct and uninterrupted contact between membranes and partner layers.

By extending current technologies, this work shows atomically clean and structurally sharp interfaces between 3D materials can be achieved, demonstrated with the $SrTiO_3$-sapphire interface that are epitaxially disallowed due to the crystal lattice symmetries (cubic and hexagonal).

7.2 Sharp heterointerface between $SrTiO_3$–sapphire heterojunctions

To form sharp and high-quality epitaxial interfaces, it is essential to use singly terminated substrates as the foundation for heterostructures. This principle also applies to membrane stacking, where a three-step process is designed to achieve atomically clean interfaces. The first step is to create a well-terminated substrate. The second step involves weakly binding the membrane to the substrate by transferring it to a substrate maintained at a stable elevated temperature. The third step is a high-temperature post-annealing in O_2. Similar heating methods have been used previously to enhance interfaces during membrane stacking [14]. In our process, we use annealing to induce bonding at the interface.

To fabricate the desired interfaces, Al-terminated step-and-terrace surfaces of (0001) sapphire crystals were prepared by thermally annealing the crystals at 1615 °C in an ultrahigh vacuum (UHV) environment ($<2\times10^{-8}$ mbar). This was achieved using a CO_2 laser emitting light at a wavelength of approximately 10 μm. Subsequently, [001]-oriented, 30-nm-thick $SrTiO_3$ membranes were fabricated from a [001]-oriented $SrTiO_3$ substrate. Following this, the membranes were then manually transferred to the freshly prepared sapphire surface, which was maintained at 80 °C. The samples were then thermally annealed at 1000 °C for 200 seconds in 0.1 mbar O_2, using CO_2 laser irradiation in a UHV chamber with precisely controlled temperature ramps. Chapter 3 provides additional fabrication details and images. The optimal annealing temperature was determined to be 90% of the highest recorded $SrTiO_3$–sapphire dewetting temperature [34, 35]. The chosen annealing process aimed to minimize interface energy through cation intermixing or bonding, leading to an incommensurate structural interface reconstruction. This reconstruction would be compatible with an atomically clean interface structure. The manual transfer of the membranes introduces some level of uncertainty into controlling the twist angle during the manufacturing process. However, following fabrication, the twist angle can be accurately measured using the electron microscope by noting the difference in tilt required to align with the [100] zone axis of $SrTiO_3$ and the [1-100] zone axis of Al_2O_3. All samples were found to be electrically insulating.

The chemical compositions and microstructures of the interfaces were analyzed using cross-sectional views obtained by high-annular dark-field scanning transmission electron microscopy (HAADF-STEM) imaging, coupled with electron energy loss spectroscopy (EELS) done by the StEM group of MPI-FKF. Large-area STEM imaging reveals a pristine, straight, and sharp interface between $SrTiO_3$ and sapphire. Throughout the sample, which spans several micrometers, the interface is free of impurities or holes, as shown in Figures 7.1. The uniformity on both sides of the interface, along with the stark chemical contrast displayed in the EELS maps (Figure 7.2), demonstrates a nominally perfect attachment of $SrTiO_3$ to sapphire. This attachment is devoid of voids, interlayer contamination, or buckling.

7.3 Atomic structure and chemistry at the interface

The inherent disparities in the crystal structures of $SrTiO_3$ and sapphire present challenges in simultaneously imaging both structures in a single projection at the atomic level. Consequently, atomic-resolution annular bright field (ABF) and HAADF-STEM imaging were performed along $SrTiO_3$ [100] and Al_2O_3 [1-100] directions to capture all

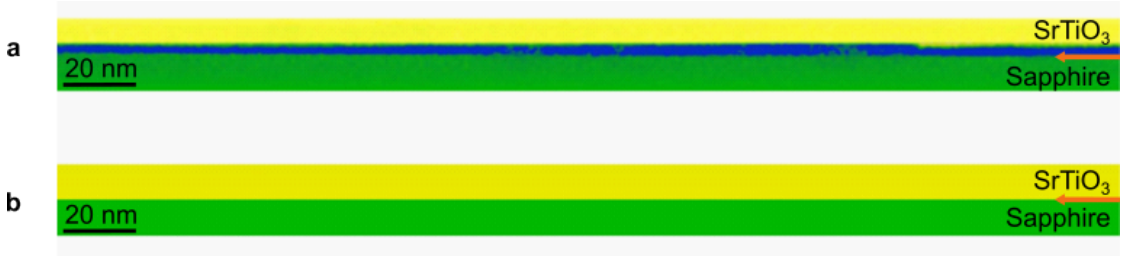

Figure 7.1: Cross-sectional large-area HAADF-STEM images of $SrTiO_3$–sapphire heterojunctions. Sample a, prepared using the standard method, exhibits an approximately 1.5-nm-thick contamination layer (blue) at the interface. In contrast, Sample b, prepared with the newly introduced method here, displays a clean interface between the $SrTiO_3$ and the sapphire. The images present raw data with a color scale indicating brightness directly. Arrows indicate the nominal interface between the sapphire and the $SrTiO_3$. Micrographs were taken by Hongguang Wang. Reproduced under terms of the CC-BY license.[108]

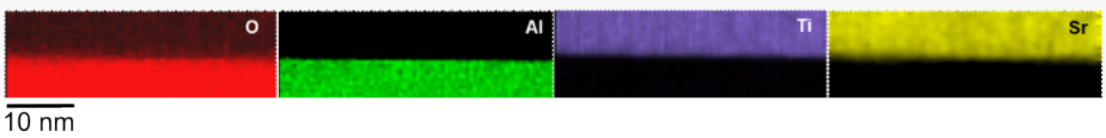

Figure 7.2: STEM-EELS maps of the constituent elements O, Al, Ti, and Sr, measured at the interface of the sample in Figures 7.1b. Micrographs were taken by Hongguang Wang.

constituent elements simultaneously, as illustrated in Figures 7.3 and 7.4. These images unveil a ∼3.5° twist angle between the two primary axes of $SrTiO_3$ and sapphire. They show surprisingly well-ordered atomic lattices at the heterojunction and reveal an exceptionally clean interface.

The ABF images, especially those in the [100] orientation of $SrTiO_3$, unveil an intriguing aspect—an apparent 2-Å-wide intensity dip between $SrTiO_3$ and sapphire, depicted in Figures 7.4a and b. This dark band, reminiscent of a gap, introduces an additional level of complexity to our comprehension of the interface, as elaborated below.

EELS maps of the heterojunction, taken along both orientations, reveal a compositionally sharp interface between $SrTiO_3$ and sapphire within the experimental resolution, as shown in Figures 7.4c, 7.5, and 7.6. These maps confirm that the first cation layer of $SrTiO_3$ at the interface is composed of Sr, while the uppermost cation layer of the sapphire surface consists of Al. Notably, there is no evidence of cation intermixing on either side of the interface.

The electronic structure modulations across the interface were studied by the StEM group using high-resolution STEM-EELS. Atomically resolved spectra with 0.6 eV resolution were used to probe the electronic states (Figure 7.7). The EELS spectra of the Ti-$L_{2,3}$ and O-K edges at each atomic layer revealed changes in the fine structure near the interface. Specifically, upon approaching the interface from the $SrTiO_3$ side, Ti-$L_{2,3}$ peaks shifted to lower energy and there was enhanced filling between the e_g and t_{2g} peaks, especially at the first $SrTiO_3$ layer adjacent to the interface (Figure 7.7b). In contrast, the intensity of the O-K edge pre-peak, which represents the filling of Ti $3d$ orbitals,[141] declined at the interface (Figure 7.7c). These findings indicate a reduction from Ti^{4+} to Ti^{3+} and significant changes in the orbital bonding environment at the first $SrTiO_3$ layer adjacent to the interface.[142] The Ti valence state in the first

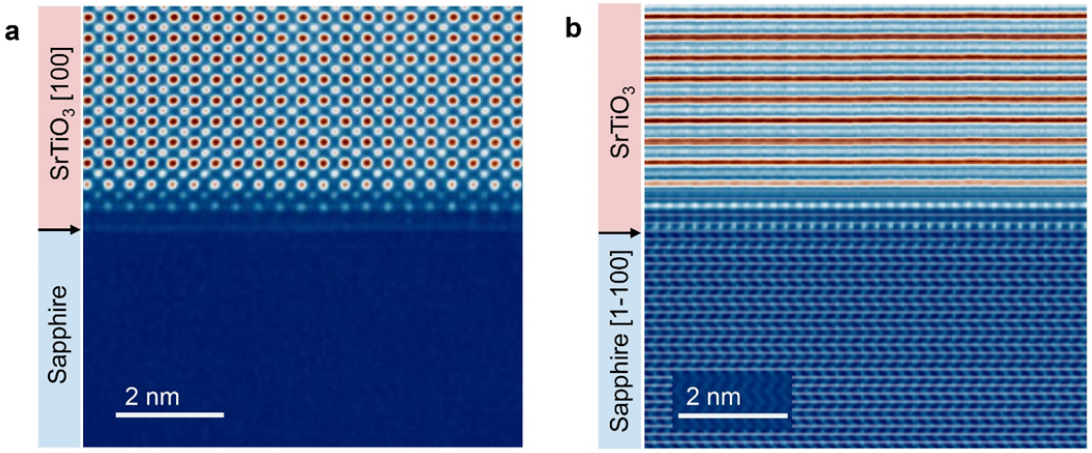

Figure 7.3: HAADF-STEM cross-sectional images of $SrTiO_3$–sapphire heterojunctions are shown, viewed along (a) $SrTiO_3$ [100] and (b) sapphire [1-100]. The arrows indicate the nominal interface between the sapphire and the $SrTiO_3$. Micrographs were taken by Hongguang Wang. Reproduced under terms of the CC-BY license.[108]

$SrTiO_3$ layer was quantified to be 3.60 ± 0.15. As a result, electronic charge accumulates, potentially due to oxygen defects. Weak Ti-$L_{2,3}$ signals across the interface were due to beam broadening. In addition, the disappearance of peak (d) in the O 1*s* to O 2*p* which is hybridized with Ti 4sp transition suggest a deviation of the Ti-O coordinate environment from TiO octahedral coordination.[143] Al-$L_{2,3}$ edges, corresponding to the electron excitation from the Al-2p to Al-3s orbitals,[144] showed that the threshold energy decreased by approximately 1.0 eV and the reduced L_3/L_2 ratio (Figure 7.7d), indicating an altered Al coordination symmetry and a reduced band gap,[145] potentially explaining the electronic charge accumulation at the interface.

7.4 Reconstruction of the atomic and electronic structures at the interface

An intricate lattice distortion is observed at the $SrTiO_3$–sapphire interface, revealing something quite remarkable. All ionic planes align with their expected positions except for the first two monolayers of $SrTiO_3$, which deviate from this pattern. Viewed in a STEM cross-section along the sapphire [1-100] direction (Figure 7.4b), the bilayer exhibits a remarkable alignment. The Sr columns in the $SrTiO_3$ layer align parallel to the Al columns in the sapphire in the region of the intensity minimum. This alignment persists despite a ∼3.5° twist angle between the $SrTiO_3$ [100] direction and the sapphire [1-100] direction. The pole figures in Figures 7.8 and 7.9, taken from a sister sample with a 4° twist, clearly capture this twist.

In the SrO layer that bonds to the top Al layer of the sapphire, the Sr ions shift toward the nearest Al ion to minimize the Coulomb energy. This relaxation causes a slight wiggling within the Sr columns (Figure 7.10). This distinct atomic reconstruction of the $SrTiO_3$ lattice at the interface provides evidence of ionic bonding between $SrTiO_3$ and sapphire. In contrast, the Al columns in the sapphire exhibit much less distortion, as depicted in Figure 7.4b, confirming the strong bonding within the sapphire crystals. Consequently, the ionic rearrangement primarily occurs within the first SrO plane of the $SrTiO_3$, with the second SrO plane already nominally aligned along the [001] axis of the

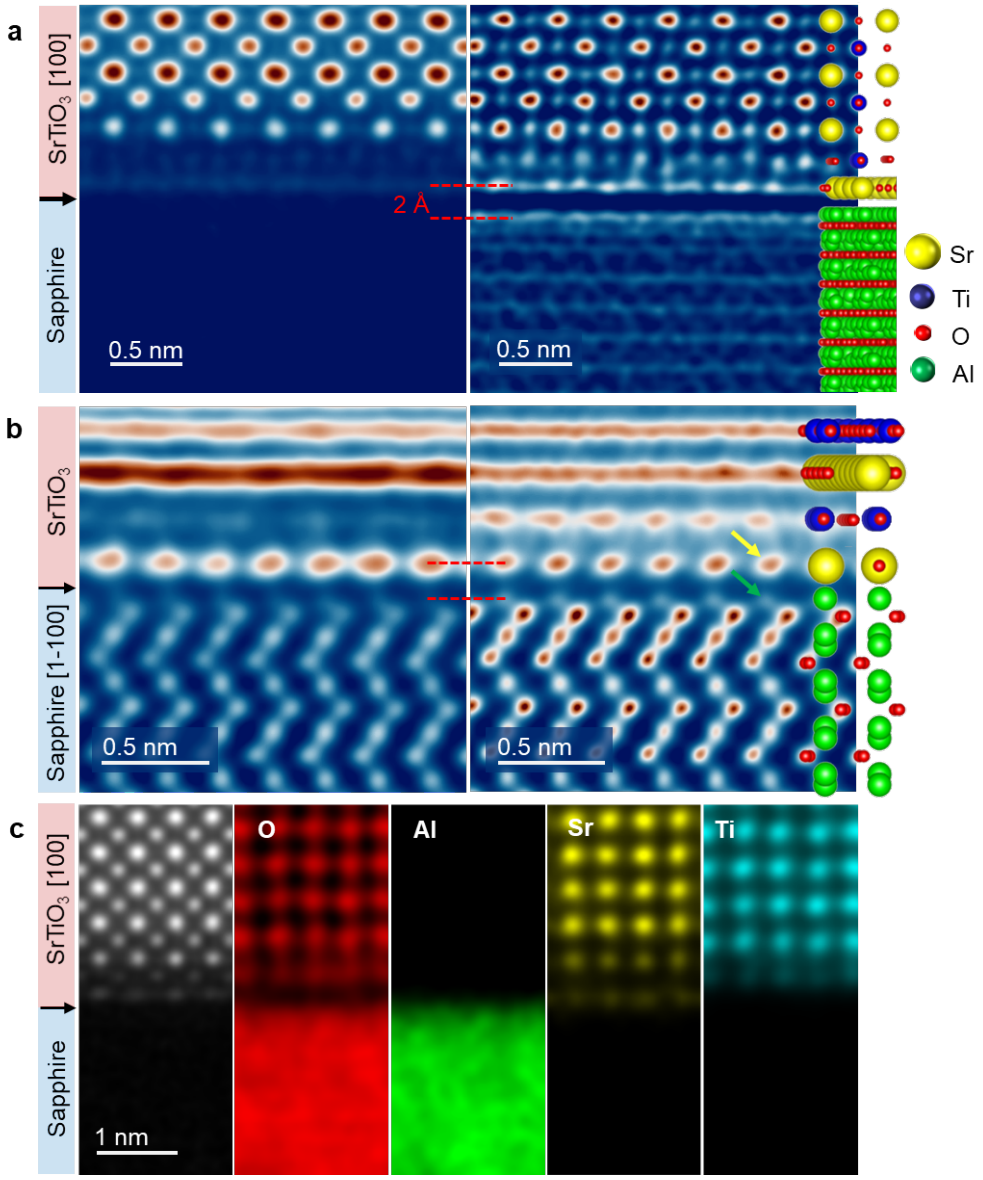

Figure 7.4: Atomic-resolution STEM images of the $SrTiO_3$–sapphire interface, viewed along the (a) $SrTiO_3$ [100] and (b) sapphire [1-100] directions. The left and right panels display HAADF and inverted ABF images, respectively. Arrows on the far left indicate the interface. The right panel in (a) reveals a dark band, suggesting a gap of approximately 2 Åbetween the top Al layer of the sapphire and the bottom Sr layer of the $SrTiO_3$, as discussed in the text. In (b), the yellow arrow marks a Sr column in the bottom layer of the $SrTiO_3$, which aligns parallel to the Al column at the top of the sapphire (green arrow). (c) presents atomic-resolution STEM-EELS maps of the constituent elements O, Al, Sr, and Ti, along with their composite maps for an interfacial cross section. Micrographs were taken by Hongguang Wang. Reproduced under terms of the CC-BY license.[108]

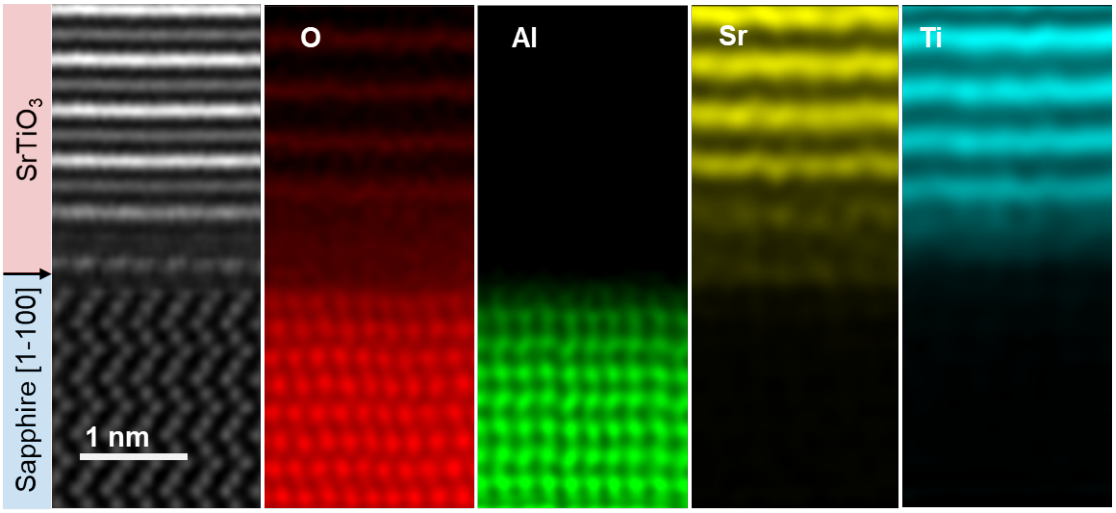

Figure 7.5: Atomic-resolution STEM-EELS maps of the cross-section of the sample discussed in this chapter, showing the constituent elements O, Al, Sr, and Ti along the Al_2O_3 [1-100] direction. Micrographs were taken by Hongguang Wang.

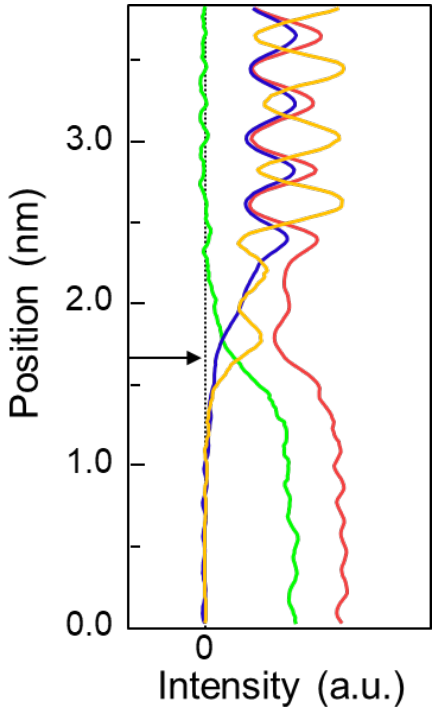

Figure 7.6: EELS signal profiles from a sample cross section covering the interface. The colored curves represent the EELS signals of O (red), Al (green), Sr (yellow), and Ti (blue). The interface is indicated by the black horizontal arrow. Profiles were made by Hongguang Wang.

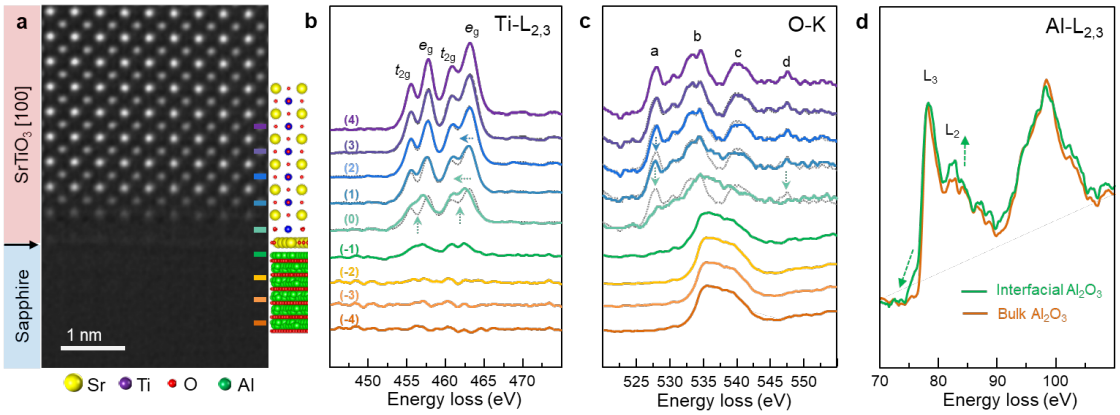

Figure 7.7: Atomic-scale analysis of the electronic structure at a $SrTiO_3$/sapphire heterojunction interface. (a) The HAADF-STEM image shows the $SrTiO_3$-sapphire interface, with a schematic of the sample structure on the right. The black arrow points to the interface, and the colored lines denote the atomic layers where EELS spectra were obtained. (b) EELS spectra of the Ti-$L_{2,3}$ edges at various atomic planes across the interface reveal a clear red-shift of the Ti-$L_{2,3}$ peaks and the filling between the e_g and t_{2g} peaks at the first $SrTiO_3$ layer adjacent to the interface, as indicated by the horizontal and vertical arrows, compared with the bulk $SrTiO_3$ Ti-$L_{2,3}$ spectrum (black dotted lines) (c) EELS spectra of the O-K edge, compared with the bulk $SrTiO_3$ O-K edge spectrum (black dotted lines), show a gradual decrease in the intensity of peak a approaching the interface and the disappearance of peak d at the first $SrTiO_3$ layer next to the interface. (d) EELS spectra of the Al-$L_{2,3}$ edges in bulk Al_2O_3 and near the interface, indicating altered local Al-O configurations and electronic structure near the interface, indicated by the reduced threshold energy of the L_3 edge and the L_3/L_2 ratio. This image was made by Hongguang Wang. Image source: Ref. [108]

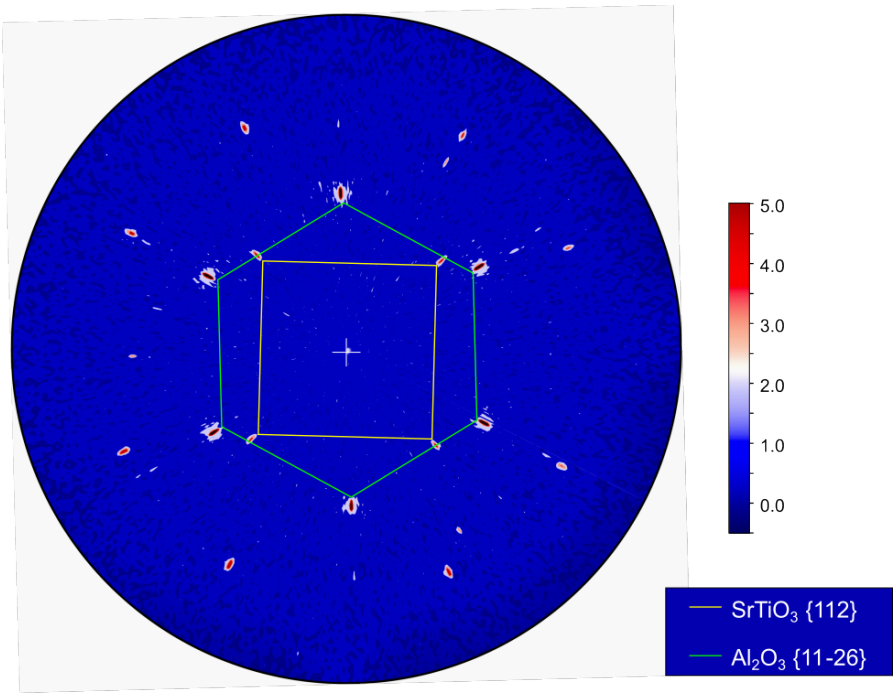

Figure 7.8: An X-ray pole figure of a $SrTiO_3$–sapphire sample with an ∼4° twist between the main crystal lattices is shown. The figure distinctly displays reflection peaks from both the hexagonal lattice of the sapphire and the square lattice of the $SrTiO_3$. Additional details can be found in Figure 7.9. Reproduced under terms of the CC-BY license.[108]

$SrTiO_3$ bulk. The spatial arrangement of Sr and oxygen ions at the interface is governed by the non-commensurate moiré pattern created by the overlapping crystal lattices of $SrTiO_3$ and sapphire, which have different lattice constants and symmetries, as shown in Figure 7.11. This, coupled with the absence of mirror symmetry at the interface plane, results in a twist within the first unit cell of $SrTiO_3$ around the interface normal, leading to a chiral crystal structure in the first $SrTiO_3$ layer.

Moreover, HAADF and low-angle annular dark-field (LAADF) images show an enhanced LAADF signal in the first two $SrTiO_3$ unit cells, suggesting local structural disorder or strain-induced electron beam dechanneling[146–148] (Figure 7.12a, b, c). 2D maps of the IP and OOP lattice parameters in a 7-uc x 7-uc region (the square region of Figure 7.12a) reveal an evidently elevated OOP lattice parameter in the $SrTiO_3$ layer adjacent to the first $SrTiO_3$ layer near the interface and unchanged IP lattice (Figure 7.12d). This layer shows a 2.8% OOP tensile strain and enhanced tetragonality of 1.03, resulting in a polar $SrTiO_3$ structure with a 20 ± 4 pm Ti atomic displacement[149] (Figure 7.12d bottom panel, e). This polarization, which calculated to be $50 \pm 10\,\mu C\ cm^{-2}$, leads to a local screening charge density of $0.47 \pm 0.09\,e^-/uc$ in the first $SrTiO_3$ layer adjacent to the interface, matching the electronic charge observed in the EELS analysis (Figure 7.7b and c).

Consistent with the clean and sharply defined microstructure of the interface, the X-ray diffraction (XRD) pole figures are remarkable. They display both the three-fold symmetry of the sapphire substrate and the four-fold symmetry of the $SrTiO_3$ layer within a single diffraction pattern, as illustrated in Figure 7.8 and Figure 7.9. Such heterostructures with these pole figures are not possible through epitaxial growth, as epitaxial growth must preserve the inherent in-plane symmetry across the interface.

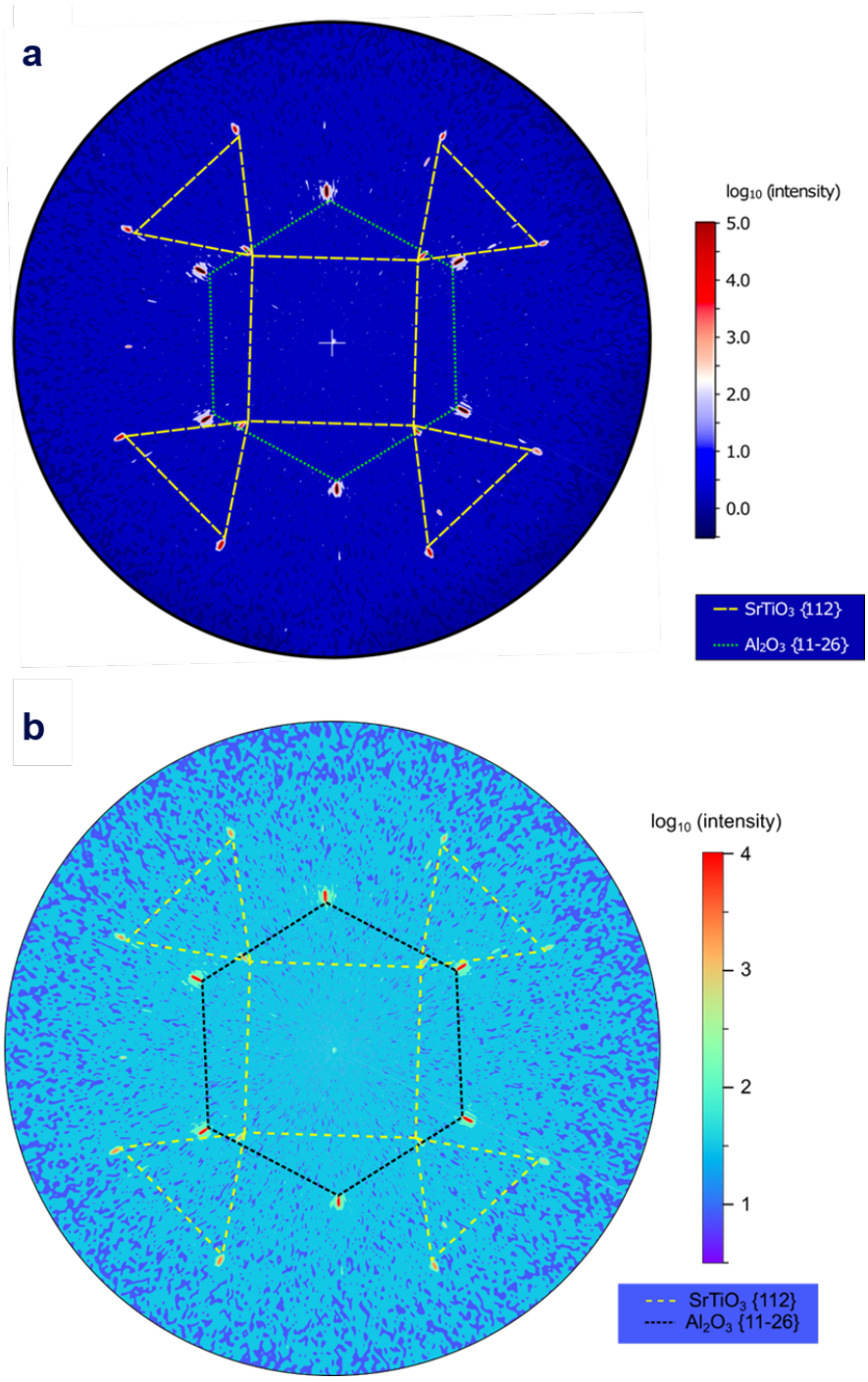

Figure 7.9: (a) A fully annotated pole figure of the data shown in Figure 7.8, identifying and marking the complete family of $SrTiO_3$ {112} planes. The 12 peaks from the {112} family are clearly visible, highlighting the 4-fold symmetry of the $SrTiO_3$. (b) This data is identical to that in Figure 7.8 but the color scale has been chosen to make the background more prominent. This image was made by Varun Harbola. Reproduced under terms of the CC-BY license.[108]

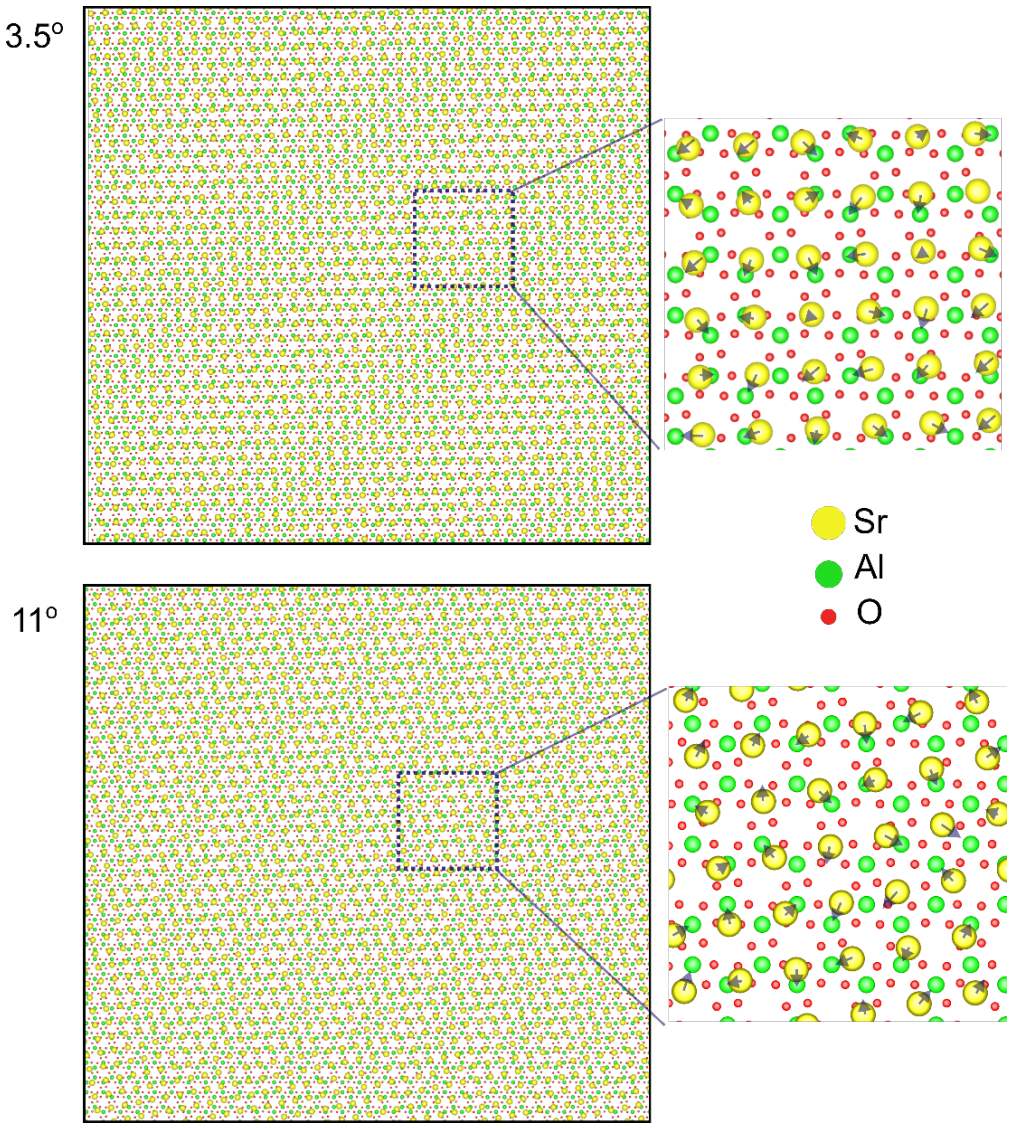

Figure 7.10: The moiré pattern arising from positioning the (001) Sr-O lattice of $SrTiO_3$ atop a singly terminated sapphire lattice with an in-plane twist angle of 3.5° and 11° between the $SrTiO_3$ [100] and the Al_2O_3 [1-100] axes. The arrows in the magnified view on the right illustrate the local shifts required for Sr ions to approach their neighboring Al ions. At this local scale, these shifts appear spatially disordered, giving an impression of randomness. However, on the larger scale of the moiré pattern formed by the superposition of $SrTiO_3$ and Al_2O_3, the shifts exhibit the quasi-periodicity characteristic of the moiré pattern. This image was made by Varun Harbola.

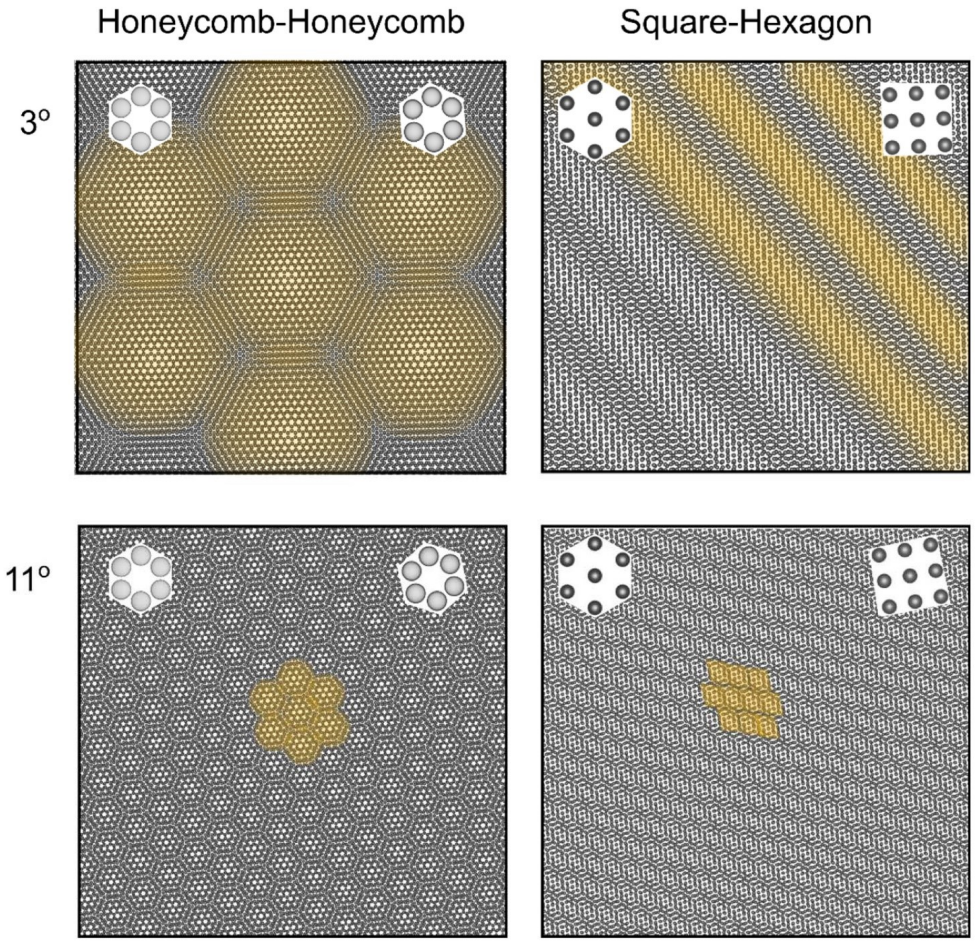

Figure 7.11: Moiré patterns resulting from the overlay of two identical hexagonal lattices (left) and a hexagonal lattice with a square lattice (right). The twist angles between the main axes of the lattices are 3° (top) and 11° (bottom) in both scenarios. Yellow shading has been added to emphasize the moiré structures. While the hexagonal–hexagonal moiré lattices exhibit the well-known repetitive six-fold pattern, the superposition of hexagonal and square lattices creates quasi-periodic stripe-like patterns. Reproduced under terms of the CC-BY license.[108]

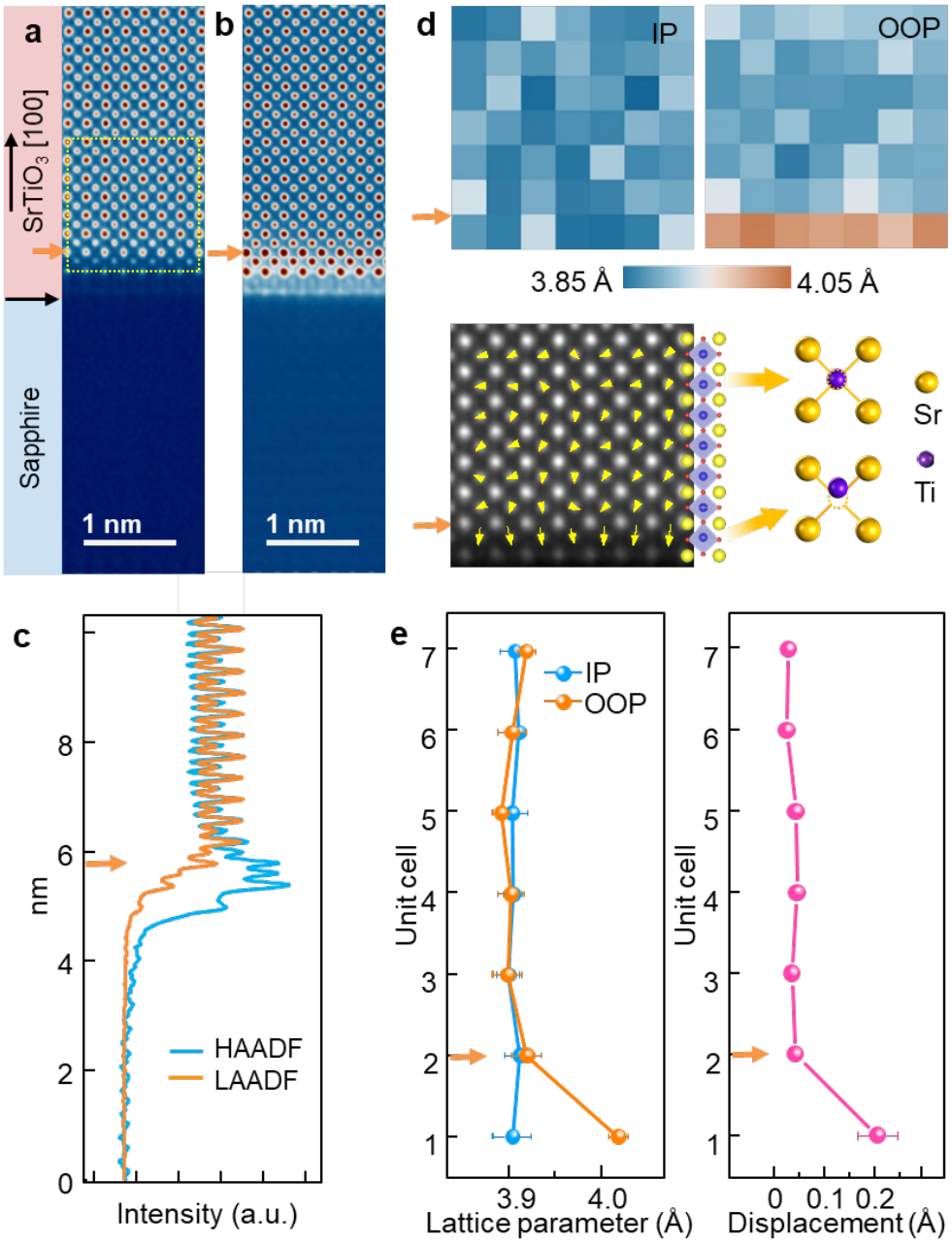

Figure 7.12: Local structural distortion and polarity at the interface. (a)-(c) Representative atomic-resolution images of the interface are observed in HAADF (a) and LAADF (b) modes along the $SrTiO_3$ [100] direction, revealing a notable enhancement of the LAADF signal intensity (c). The black arrow indicates the out-of-plane direction. The vertical dark arrow specifies the out-of-plane (OOP) direction, while the orange arrow highlights the second $SrTiO_3$ layer adjacent to the interface. (d) Maps of the measured lattice constant are shown along the in-plane (IP) direction (d, top-left panel) and the OOP direction (d, top-right panel), along with an atomic displacement map (d, bottom panel) of the yellow-marked square regions in (a). (e) Laterally averaged profiles of lattice parameters and displacements measured along the out-of-plane direction illustrate an evident lattice expansion and polarization in the second $SrTiO_3$ layer next to the interface. This image was made by Hongguang Wang.

7.5 Conclusion and outlook

This study demonstrates a method to fabricate atomically sharp interfaces between materials with different lattice symmetries, overcoming the constraints of conventional epitaxial growth techniques. The process involves three key steps: (a) epitaxial growth and lift-off technique to obtain freestanding oxide membranes, (b) high-quality single-terminated surfaces achieved through meticulous substrate preparation, and (c) high-temperature post-deposition annealing. $SrTiO_3$–sapphire heterojunctions have been used as a case study to explore interfaces between materials with cubic and hexagonal symmetries. Atomic-resolution STEM and EELS analyses revealed these interfaces possess exceptional structural homogeneity, cleanness, and atomic sharpness. Surprisingly, they exhibit a unique structural configuration. The Sr ions in the Sr-O plane near the interface shift towards the closest Al neighbors, causing local deformation of the moiré lattice created by the square and hexagonal crystal lattices. This shift introduces chirality into the $SrTiO_3$ layer at the interface. The quasi-crystalline reconstruction of interfacial cations allows for incoherent lattice distortion on the bulk lattice scale, thus enabling the observed lattice relaxation within a single monolayer.

The preparation process described here eliminates the stringent requirement for epitaxial growth, which typically necessitates matching crystal lattice symmetries for high-quality interfaces between 3D materials. Additionally, the constraint of fitting lattice constants is rendered obsolete. However, not all potential material combinations are suitable for these interfaces, as other constraints related to epitaxial growth—such as chemical compatibility, matching thermal expansion, and preventing interdiffusion at fabrication temperatures—still apply.

The moiré-type structural rearrangement of ionic positions at interfaces between ionic crystals, as reported here, has been achieved by combining crystal lattices with three-fold and four-fold symmetries. It's anticipated that similar phenomena will also occur when crystals with other symmetries are joined, provided that strong bonding is established across the interfaces. Due to mismatched symmetries, interfaces formed in this manner will produce relaxed thin films with saturated bonds on well-defined surfaces, instead of extended defects like edge dislocations. The ability to connect lattices with different symmetries and lattice constants opens up a highly promising new phase space for creating innovative electron systems with exceptional properties at the interfaces between 3D materials. Looking ahead, the unequal symmetries of the materials at these interfaces promise novel electronic and magnetic behaviors, including new forms of 2D electron systems, multiferroicity, topological phenomena, and symmetry-induced frustration that could affect their properties. Furthermore, the ability to select membrane–substrate twists introduces a new realm of potential moiré patterns and related phenomena, as illustrated in Figure 7.11. Additionally, novel transport phenomena, such as current flow across Josephson junctions and distinct electronic behaviors within superlattices formed by stacking these bilayers, are anticipated to emerge as exciting avenues for future exploration.

Chapter 8

Summary, conclusion, and outlook

Thin solid films play a vital role in numerous device applications and are essential for research across various fields. Significant advancements have been made over time in the production of these high-quality films, yet challenges remain. A key limitation in thin film deposition is the need to match the crystalline structure and lattice constants of the films with those of the substrates. Furthermore, the rigid attachment of solid films to their bulk substrates restricts their flexibility, limiting their application in more adaptable technologies.

The membrane technique has been recently developed, allowing oxide films to be separated from their bulk substrates. This method enables the film fabrication to be more flexible and adaptable to various applications. The core aim of this thesis is to utilize this membrane technique to overcome the restrictions of conventional thin film epitaxy, opening up new possibilities for film design and functionality. The initial focus of my research was the fabrication of oxide membranes of different materials. Given the fragile nature of these membranes, considerable attention has been paid to optimizing deposition conditions, selecting appropriate buffer layers, and tuning buffer layer thickness. These efforts have made it possible to transfer large ($4.5 \times 4.5\,\mathrm{mm}^2$) and intact membrane areas, an important step forward in advancing the technique.

The primary work carried out is presented in chapters 4 to 7. In chapter 4, a breakthrough method for fabricating nanocrystalline structures is presented, leveraging the relatively week bonding of oxide membranes to their substrates. When $SrTiO_3$ or $LaAlO_3$ membranes are transferred onto thermally prepared sapphire substrates and annealed at about half their melting temperatures, they self-assemble into nanocrystals, nanowires, and nanovoids. Transmission electron microscopy reveals these nanostructures' high crystallinity, uniform element distribution, and defect-free structures with well-defined facets. Nanocrystals with size down to 100 nm laterally and nanowires with aspect ratios over 10 have been achieved. This method surpasses traditional techniques like electron beam lithography and ion milling to fabricate nanoparticles, offering enhanced quality and greater opportunities for applications in optics, catalysis, and nanoelectronics. An analytical model developed during this research provides insight into the interface energy between the membrane and substrate, offering predictive control over nanostructure formation. Further research is proposed to explore pre-templating techniques on membranes or substrates before processing to gain greater control over the self-assembly process. This enhanced control could lead to the fabrication of more complex and functional nanostructures with numerous potential applications.

Another advancement achieved is the development of the vector substrates concept, a novel approach to substrates. This approach recognizes that only a thin surface layer is essential for film growth. The vector-substrate technique aims at utilizing this surface layer while minimizing the bulk's impact on cost and physical properties. By transferring a membrane-like template layer from a reusable parent substrate onto a separate carrier, this method allows independent optimization of both components. Testing this concept, vector substrates with sapphire carriers and $SrTiO_3$ membranes were fabricated and successfully used for the growth of high-quality epitaxial $La_{0.67}Sr_{0.33}MnO_3$ films, which avoided common artifacts generated by the use of conventional $SrTiO_3$ substrates. While initial studies produced substrates up to $4.5 \times 4.5\,mm^2$, scaling this method to larger surface areas and automating the process is predicted to make it commercially viable. Despite this, the currently available sizes already meet many research needs. Vector substrates provide a promising alternative to conventional methods, enabling optimized substrate fabrication without single-crystal growth.

One of the interesting cases for the use of vector substrate is when the substrate is costly or difficult to acquire, as is the case e.g. for bicrystal substrates. Based on the development of vector substrate, chapter 6 tackles the challenge by using bicrystalline membranes. This method eliminates the need for bicrystalline substrates to grow bicrystal Josephson junctions, allowing them to be grown on bulk substrates of choice which are coated with just 10-nm-thick bicrystalline membranes. The viability of this technique is demonstrated by fabricating high-quality, 24° $YBa_2Cu_3O_{7-x}$ bicrystalline Josephson junctions on bulk single crystalline sapphire substrates coated with bicrystalline $SrTiO_3$ membrane. Additionally, this novel concept opens the door for creating tricrystalline or polycrystalline substrates, for the growth of bicrystalline films from various materials, and for depositing heterostructures that comprise single-crystalline films on top of bicrystal layers.

A surprising result achieved in the context of this thesis is the realization of a novel method for creating atomically sharp interfaces between materials with different lattice symmetries, overcoming one of the primary limitations of conventional epitaxy. The process involves three steps: (a) epitaxial growth and lift-off to obtain freestanding oxide membranes, (b) precise substrate preparation for single-terminated surfaces, and (c) high-temperature post-annealing. Using $SrTiO_3$–sapphire heterojunctions as a case study, atomic-resolution STEM and EELS analyses reveal exceptional interface quality with a unique structural configuration. Sr ions near the interface shift towards Al neighbors, introducing chirality and enabling lattice relaxation within a single monolayer. This method bypasses the need for matching lattice symmetries or constants in epitaxial growth, though chemical compatibility, thermal expansion, and interdiffusion constraints remain. The ability to join materials with different symmetries opens up opportunities for creating innovative 2D electron systems, multiferroics, and topological phenomena. Future possibilities include investigating moiré patterns, novel transport properties, and unique behaviors in Josephson junctions and superlattices created by stacking bilayers.

Over the past decade, the field of oxide membranes has taken remarkable steps forward, enabling the fabrication of a diverse range of oxide materials (Figure 8.1) and contributing to important breakthroughs. These successes underline the promising character of the development in this area. Through control of strain, texture, and composition, oxide membranes can be engineered, unlocking a remarkable range of tunable properties.[15, 17, 29, 30] This approach has also led to the investigating of elastic limits of oxide films[29, 31] and facilitated the heterointegration of devices,[19] paving the way for novel applications. With these expanded degrees of freedom, the field now

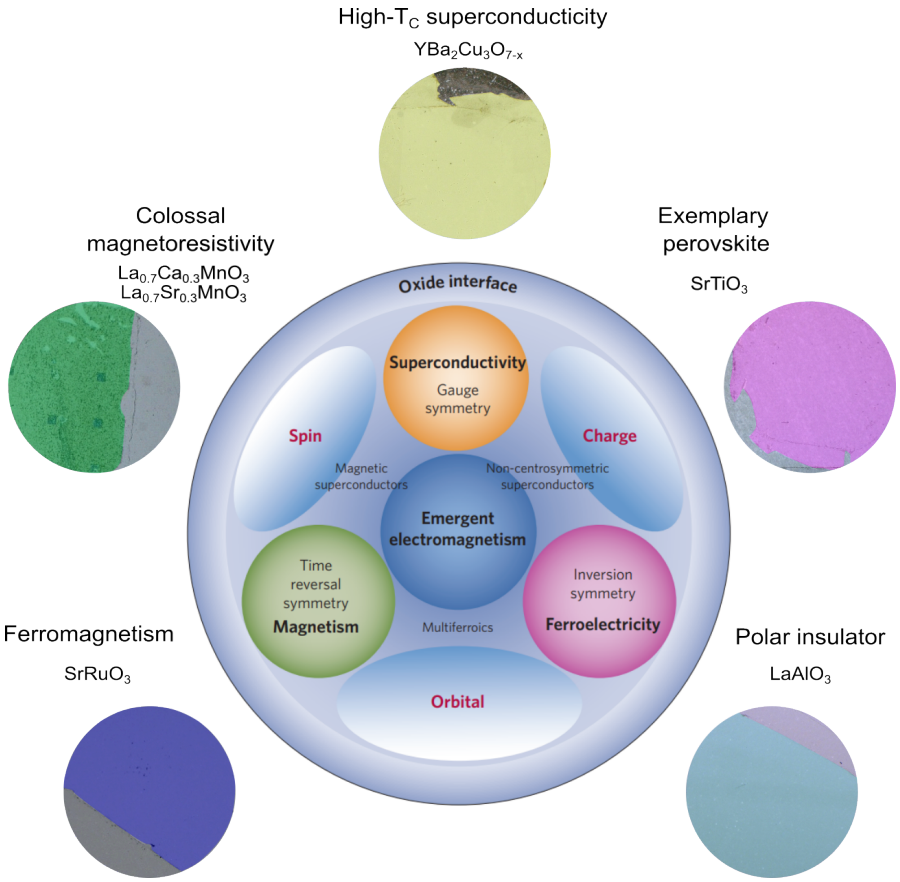

Figure 8.1: Fabricated membranes made from diverse materials with different properties highlight the potential of membrane technology and offer a wide range of options for different applications. The figure is partially based on the Figure 1 of Ref. [13], with permission from Springer Nature.

holds possibilities that were previously unimaginable, yet numerous areas remain unexplored. This research presents new pathways that were once out of reach, including innovative techniques for fabricating nanocrystals of unprecedented quality and creating custom substrates. The ability to combine distinct materials with atomically clean interfaces provides a valuable framework for further experimentation, allowing researchers to customize and expand material combinations. These findings highlight the extensive potential that oxide membranes bring to the table and suggest promising directions for future innovations in materials science.

Commercial application of oxide membranes is likely not feasible in a short term due to the need for further optimization in fabrication, release, and transfer processes. This study on membranes initially started with small-area transfers, and required considerable optimization to achieve a transfer area of 4.5 x 4.5 mm^2—a meaningful milestone. However, further scaling up remains crucial and will likely progress gradually. For further commercial applications and large-area transfers, accelerating the dissolving process is essential. Additionally, automating the process will be key to ensuring consistent, high-quality results. Freestanding oxide membranes exhibit unique properties, offering significant potential for new discoveries. This makes them both a compelling and challenging subject for ongoing research.

Freestanding oxide membranes are anticipated to significantly impact both fundamental materials science and practical applications, opening a vast array of new possibilities. It is expected that techniques developed for oxide membranes can be extended to further material systems, such as nitrides, carbides, and potentially many more, unlocking new functionalities and uses. A particularly exciting avenue in fundamental studies is the potential for heterointegration, where different materials, including combinations of 2D and 3D materials, are integrated in innovative ways. This approach may give rise to emergent phenomena in materials science, potentially overcoming the limitations of Moore's law as it nears saturation. Additionally, the high-quality nanostructures with well-defined facets discovered in this study hold promising potential for research in catalysis, optics, and quantum computing, among other fields. Using templated membranes or substrates could enable more precise control over their quality and size.

Looking further into the future, freestanding oxide membranes offer exceptional adaptability to meet the growing demand for versatile materials essential for next-generation technologies. For example, flexible electronics, such as displays, sensors, and wearable devices, require adaptable materials that support more user-friendly, human-centered designs. This flexibility opens new ways to rethink our everyday interactions with technology. Additionally, as oxide membranes are scaled down in both size and weight compare to their bulk, these membranes could power a new wave of advancements in lightweight aerospace components. The nanocrystals with superb quality also holds transformative potential across fields like efficient solar cells, advanced sensors, and sustainable energy solutions.

The research presented in this thesis offers a glimpse into a transformative future for materials science, where oxides play a crucial role. As research advances, these techniques hold the potential to make a profound impact across various technological fields, opening doors to the next generation of innovations in electronics, energy, and more.

Bibliography

1. Klitzing, K. v., Dorda, G. & Pepper, M. New method for high-accuracy determination of the fine-structure constant based on quantized Hall resistance. *Physical review letters* **45,** 494 (1980).
2. Tsukazaki, A., Ohtomo, A., Kita, T., Ohno, Y., Ohno, H. & Kawasaki, M. Quantum Hall Effect in Polar Oxide Heterostructures. *Science* **315,** 1388–1391 (2007).
3. Pohl, U. W. *Epitaxy of semiconductors* (Springer, 2020).
4. Nakamura, S., Mukai, T. & Senoh, M. Candela-class high-brightness InGaN/AlGaN double-heterostructure blue-light-emitting diodes. *Applied Physics Letters* **64,** 1687–1689 (1994).
5. Binasch, G., Grünberg, P., Saurenbach, F. & Zinn, W. Enhanced magnetoresistance in layered magnetic structures with antiferromagnetic interlayer exchange. *Physical review B* **39,** 4828 (1989).
6. Maekawa, S., Tohyama, T., Barnes, S. E., Ishihara, S., Koshibae, W. & Khaliullin, G. *Physics of transition metal oxides* (Springer Science & Business Media, 2013).
7. Imada, M., Fujimori, A. & Tokura, Y. Metal-insulator transitions. *Reviews of Modern Physics* **70,** 1039 (1998).
8. Rizwan, M., Gul, S., Iqbal, T., Mushtaq, U., Farooq, M. H., Farman, M., Bibi, R. & Ijaz, M. A review on perovskite lanthanum aluminate ($LaAlO_3$), its properties and applications. *Materials Research Express* **6,** 112001 (2019).
9. Tsymbal, E. Y., Dagotto, E. R., Eom, C.-B. & Ramesh, R. *Multifunctional oxide heterostructures* (OUP Oxford, 2012).
10. Ohtomo, A & Hwang, H. A high-mobility electron gas at the $LaAlO_3/SrTiO_3$ heterointerface. *Nature* **427,** 423–426 (2004).
11. Li, L., Richter, C., Mannhart, J. & Ashoori, R. C. Coexistence of magnetic order and two-dimensional superconductivity at $LaAlO_3/SrTiO_3$ interfaces. *Nature physics* **7,** 762–766 (2011).
12. Fu, D. & Itoh, M. in *Ferroelectrics* (ed Lallart, M.) chap. 20 (IntechOpen, Rijeka, 2011).
13. Hwang, H. Y., Iwasa, Y., Kawasaki, M., Keimer, B., Nagaosa, N. & Tokura, Y. Emergent phenomena at oxide interfaces. *Nature materials* **11,** 103–113 (2012).
14. Li, Y. *et al.* Stacking and twisting of freestanding complex oxide thin films. *Advanced materials* **34,** 2203187 (2022).
15. Xu, R. *et al.* Strain-induced room-temperature ferroelectricity in $SrTiO_3$ membranes. *Nature communications* **11,** 3141 (2020).
16. Dong, G. *et al.* Periodic wrinkle-patterned single-crystalline ferroelectric oxide membranes with enhanced piezoelectricity. *Advanced materials* **32,** 2004477 (2020).
17. Pesquera, D., Fernández, A., Khestanova, E. & Martin, L. W. Freestanding complex-oxide membranes. *Journal of Physics: Condensed Matter* **34,** 383001 (2022).
18. Lu, D., Baek, D. J., Hong, S. S., Kourkoutis, L. F., Hikita, Y. & Hwang, H. Y. Synthesis of freestanding single-crystal perovskite films and heterostructures by etching of sacrificial water-soluble layers. *Nature materials* **15,** 1255–1260 (2016).

19. Kum, H. S. *et al.* Heterogeneous integration of single-crystalline complex-oxide membranes. *Nature* **578,** 75–81 (2020).
20. Dahm, R. T. *et al.* Size-controlled spalling of $LaAlO_3/SrTiO_3$ micromembranes. *ACS applied materials & interfaces* **13,** 12341–12346 (2021).
21. Ji, D. *et al.* Freestanding crystalline oxide perovskites down to the monolayer limit. *Nature* **570,** 87–90 (2019).
22. Yun, S., le Cozannet, T. E., Christoffersen, C. H., Brand, E., Jespersen, T. S. & Pryds, N. Strain Engineering: Perfecting Freestanding Perovskite Oxide Fabrication. *Small* **20,** 2310782 (2024).
23. Pesquera, D. *et al.* Large magnetoelectric coupling in multiferroic oxide heterostructures assembled via epitaxial lift-off. *Nature Communications* **11,** 3190 (2020).
24. Eom, K. *et al.* Electronically reconfigurable complex oxide heterostructure freestanding membranes. *Science Advances* **7,** eabh1284 (2021).
25. Bakaul, S. R. *et al.* Single crystal functional oxides on silicon. *Nature communications* **7,** 10547 (2016).
26. Bakaul, S. R., Serrao, C. R., Lee, O., Lu, Z., Yadav, A., Carraro, C., Maboudian, R., Ramesh, R. & Salahuddin, S. High Speed Epitaxial Perovskite Memory on Flexible Substrates. *Advanced Materials* **29,** 1605699 (2017).
27. Schlom, D. G., Chen, L.-Q., Pan, X., Schmehl, A. & Zurbuchen, M. A. A thin film approach to engineering functionality into oxides. *Journal of the American Ceramic Society* **91,** 2429–2454 (2008).
28. Chiabrera, F. M. *et al.* Freestanding perovskite oxide films: Synthesis, challenges, and properties. *Annalen der Physik* **534,** 2200084 (2022).
29. Dong, G. *et al.* Super-elastic ferroelectric single-crystal membrane with continuous electric dipole rotation. *Science* **366,** 475–479 (2019).
30. Hong, S. S. *et al.* Extreme tensile strain states in $La_{0.7}Ca_{0.3}MnO_3$ membranes. *Science* **368,** 71–76 (2020).
31. Harbola, V., Crossley, S., Hong, S. S., Lu, D., Birkholzer, Y. A., Hikita, Y. & Hwang, H. Y. Strain gradient elasticity in $SrTiO_3$ membranes: bending versus stretching. *Nano letters* **21,** 2470–2475 (2021).
32. Sun, H. *et al.* Chemically specific termination control of oxide interfaces via layer-by-layer mean inner potential engineering. *Nature communications* **9,** 2965 (2018).
33. Stan, C. V., Beavers, C. M., Kunz, M. & Tamura, N. X-ray diffraction under extreme conditions at the Advanced Light Source. *Quantum Beam Science* **2,** 4 (2018).
34. Harbola, V., Wu, Y.-J., Hensling, F. V., Wang, H., van Aken, P. A. & Mannhart, J. Vector Substrates: Idea, Design, and Realization. *Advanced Functional Materials* **34,** 2306289 (2024).
35. Harbola, V., Wu, Y.-J., Wang, H., Smink, S., Parks, S. C., van Aken, P. A. & Mannhart, J. Self-Assembly of Nanocrystalline Structures from Freestanding Oxide Membranes. *Advanced materials* **35,** 2210989 (2023).
36. Vajtai, R. *Springer handbook of nanomaterials* (Springer Science & Business Media, 2013).
37. Montanarella, F. & Kovalenko, M. V. Three millennia of nanocrystals. *ACS nano* **16,** 5085–5102 (2022).
38. Lu, W. & Lieber, C. M. Nanoelectronics from the bottom up. *Nature materials* **6,** 841–850 (2007).
39. Talapin, D. V., Lee, J.-S., Kovalenko, M. V. & Shevchenko, E. V. Prospects of colloidal nanocrystals for electronic and optoelectronic applications. *Chemical reviews* **110,** 389–458 (2010).

40. Sattler, K. D. *Handbook of nanophysics: nanoelectronics and nanophotonics* (CRC press, 2010).
41. Ariga, K., Hill, J. P., Lee, M. V., Vinu, A., Charvet, R. & Acharya, S. Challenges and breakthroughs in recent research on self-assembly. *Science and technology of advanced materials* **9,** 014109 (2008).
42. Thompson, C. V. Solid-state dewetting of thin films. *Annual Review of Materials Research* **42,** 399–434 (2012).
43. Ye, J. & Thompson, C. V. Templated Solid-State Dewetting to Controllably Produce Complex Patterns. *Advanced Materials* **13,** 1567–1571 (2011).
44. Ye, J., Zuev, D. & Makarov, S. Dewetting mechanisms and their exploitation for the large-scale fabrication of advanced nanophotonic systems. *International Materials Reviews* **64,** 439–477 (2019).
45. Leroy, F., Cheynis, F, Almadori, Y, Curiotto, S, Trautmann, M, Barbé, J., Müller, P, *et al.* How to control solid state dewetting: A short review. *Surface Science Reports* **71,** 391–409 (2016).
46. Nuryadi, R, Ishikawa, Y & Tabe, M. Formation and ordering of self-assembled Si islands by ultrahigh vacuum annealing of ultrathin bonded silicon-on-insulator structure. *Applied surface science* **159,** 121–126 (2000).
47. Fan, Y., Nuryadi, R., Burhanudin, Z. A. & Tabe, M. Thermal agglomeration of ultrathin silicon-on-insulator layers: Crystalline orientation dependence. *Japanese journal of applied physics* **47,** 1461 (2008).
48. Coll, M, Gazquez, J, Pomar, A, Puig, T, Sandiumenge, F & Obradors, X. Stress-induced spontaneous dewetting of heteroepitaxial $YBa_2Cu_3O_7$ thin films. *Physical Review B—Condensed Matter and Materials Physics* **73,** 075420 (2006).
49. Ye, J. & Thompson, C. V. Mechanisms of complex morphological evolution during solid-state dewetting of single-crystal nickel thin films. *Applied Physics Letters* **97,** 071904 (2010).
50. Ye, J. & Thompson, C. V. Anisotropic edge retraction and hole growth during solid-state dewetting of single crystal nickel thin films. *Acta materialia* **59,** 582–589 (2011).
51. Hyun Kim, G., Zucker, R. V., Ye, J., Craig Carter, W & Thompson, C. V. Quantitative analysis of anisotropic edge retraction by solid-state dewetting of thin single crystal films. *Journal of Applied Physics* **113,** 043512 (2013).
52. Ye, J. Fabrication of ordered arrays of micro-and nanoscale features with control over their shape and size via templated solid-state dewetting. *Scientific reports* **5,** 9823 (2015).
53. Zucker, R. V., Kim, G. H., Ye, J., Carter, W. C. & Thompson, C. V. The mechanism of corner instabilities in single-crystal thin films during dewetting. *Journal of Applied Physics* **119,** 125306 (2016).
54. Burhanudin, Z. A., Nuryadi, R., Ishikawa, Y., Tabe, M. & Ono, Y. Thermally-induced formation of Si wire array on an ultrathin (111) silicon-on-insulator substrate. *Applied Physics Letters* **87,** 121905 (2005).
55. Aouassa, M., Favre, L., Ronda, A, Maaref, H & Berbezier, I. The kinetics of dewetting ultra-thin Si layers from silicon dioxide. *New Journal of Physics* **14,** 063038 (2012).
56. Jiran, E & Thompson, C. Capillary instabilities in thin films. *Journal of electronic materials* **19,** 1153–1160 (1990).
57. Nie, J., Yamasaki, H & Mawatari, Y. Self-assembled growth of CeO_2 nanostructures on sapphire. *Physical Review B—Condensed Matter and Materials Physics* **70,** 195421 (2004).

58. Lüders, U, Sánchez, F & Fontcuberta, J. Self-organized structures in $CoCr_2O_4$ (001) thin films: Tunable growth from pyramidal clusters to a {111} fully faceted surface. *Physical Review B—Condensed Matter and Materials Physics* **70,** 045403 (2004).
59. Kim, G. H. & Thompson, C. V. Effect of surface energy anisotropy on Rayleigh-like solid-state dewetting and nanowire stability. *Acta Materialia* **84,** 190–201 (2015).
60. Gadkari, P., Warren, A., Todi, R., Petrova, R. & Coffey, K. Comparison of the agglomeration behavior of thin metallic films on SiO_2. *Journal of Vacuum Science & Technology A* **23,** 1152–1161 (2005).
61. Mizsei, J & Lantto, V. In situ AFM, XRD and resistivity studies of the agglomeration of sputtered silver nanolayers. *Journal of Nanoparticle Research* **3,** 271–278 (2001).
62. Eglitis, R. & Vanderbilt, D. First-principles calculations of atomic and electronic structure of $SrTiO_3$(001) and (011) surfaces. *Physical Review B—Condensed Matter and Materials Physics* **77,** 195408 (2008).
63. Navrotsky, A., Ma, C., Lilova, K. & Birkner, N. Nanophase transition metal oxides show large thermodynamically driven shifts in oxidation-reduction equilibria. *science* **330,** 199–201 (2010).
64. Messmer, C & Bilello, J. The surface energy of Si, GaAs, and GaP. *Journal of Applied Physics* **52,** 4623–4629 (1981).
65. Randolph, S., Fowlkes, J., Melechko, A., Klein, K., Meyer, H., Simpson, M. & Rack, P. Controlling thin film structure for the dewetting of catalyst nanoparticle arrays for subsequent carbon nanofiber growth. *Nanotechnology* **18,** 465304 (2007).
66. Altomare, M., Nguyen, N. T. & Schmuki, P. Templated dewetting: designing entirely self-organized platforms for photocatalysis. *Chemical science* **7,** 6865–6886 (2016).
67. Bollani, M. *et al.* Templated dewetting of single-crystal sub-millimeter-long nanowires and on-chip silicon circuits. *Nature communications* **10,** 5632 (2019).
68. McKee, R. A., Walker, F. & Chisholm, M. Crystalline oxides on silicon: the first five monolayers. *Physical Review Letters* **81,** 3014 (1998).
69. Liu, B. *et al.* Epitaxial La-doped $SrTiO_3$ on silicon: A conductive template for epitaxial ferroelectrics on silicon. *Applied physics letters* **80,** 4801–4803 (2002).
70. Dubourdieu, C. *et al.* Switching of ferroelectric polarization in epitaxial $BaTiO_3$ films on silicon without a conducting bottom electrode. *Nature nanotechnology* **8,** 748 (2013).
71. McDaniel, M. D., Ngo, T. Q., Hu, S., Posadas, A., Demkov, A. A. & Ekerdt, J. G. Atomic layer deposition of perovskite oxides and their epitaxial integration with Si, Ge, and other semiconductors. *Applied Physics Reviews* **2,** 041301 (2015).
72. Mannix, A. J. *et al.* Robotic four-dimensional pixel assembly of van der Waals solids. *Nature nanotechnology* **17,** 361–366 (2022).
73. Wang, J. *et al.* Refreshment of $SrTiO_3$ Substrate for Layer Peeling-off using Sacrificial $Sr_3Al_2O_6$. *Advanced Materials Interfaces* **10,** 2202111 (2023).
74. Lee, D. K., Park, Y., Sim, H., Park, J., Kim, Y., Kim, G.-Y., Eom, C.-B., Choi, S.-Y. & Son, J. Heterogeneous integration of single-crystalline rutile nanomembranes with steep phase transition on silicon substrates. *Nature communications* **12,** 5019 (2021).
75. Braun, W., Jaeger, M., Laskin, G., Ngabonziza, P., Voesch, W., Wittlich, P. & Mannhart, J. In situ thermal preparation of oxide surfaces. *APL Materials* **8,** 071112 (2020).

76. Zhang, B., Yun, C. & MacManus-Driscoll, J. L. High yield transfer of clean large-area epitaxial oxide thin films. *Nano-Micro Letters* **13,** 1–14 (2021).
77. Egilmez, M, Saber, M., Fan, I, Chow, K. & Jung, J. Correlation of structural phase transition and electrical transport properties of manganite films on $SrTiO_3$. *Physical Review B—Condensed Matter and Materials Physics* **78,** 172405 (2008).
78. Chopdekar, R. V., Arenholz, E. & Suzuki, Y. Orientation and thickness dependence of magnetization at the interfaces of highly spin-polarized manganite thin films. *Physical Review B—Condensed Matter and Materials Physics* **79,** 104417 (2009).
79. Fontcuberta, J., Skumryev, V., Laukhin, V., Granados, X. & Salje, E. K. Polar domain walls trigger magnetoelectric coupling. *Scientific reports* **5,** 13784 (2015).
80. Liao, Z., Jin, R., Plummer, E. & Zhang, J. Delicate competing electronic states in ultrathin manganite films. *Physical Review B* **95,** 085130 (2017).
81. Paudel, B., Zhang, B., Sharma, Y., Kang, K. T., Nakotte, H., Wang, H. & Chen, A. Anisotropic domains and antiferrodistortive-transition controlled magnetization in epitaxial manganite films on vicinal $SrTiO_3$ substrates. *Applied Physics Letters* **117,** 081903 (2020).
82. Ziese, M., Vrejoiu, I., Setzer, A., Lotnyk, A. & Hesse, D. Coupled magnetic and structural transitions in $La_{0.7}Sr_{0.3}MnO_3$ films on $SrTiO_3$. *New Journal of Physics* **10,** 063024 (2008).
83. Slonczewski, J. & Thomas, H. Interaction of elastic strain with the structural transition of strontium titanate. *Physical Review B* **1,** 3599 (1970).
84. He, F., Wells, B., Shapiro, S., Zimmermann, M. v., Clark, A & Xi, X. Anomalous phase transition in strained $SrTiO_3$ thin films. *Applied physics letters* **83,** 123–125 (2003).
85. Loetzsch, R, Lübcke, A, Uschmann, I, Förster, E, Große, V, Thuerk, M, Koettig, T, Schmidl, F & Seidel, P. The cubic to tetragonal phase transition in $SrTiO_3$ single crystals near its surface under internal and external strains. *Applied Physics Letters* **96** (2010).
86. Song, J. H., Susaki, T. & Hwang, H. Y. Enhanced thermodynamic stability of epitaxial oxide thin films. *Advanced materials* **20,** 2528–2532 (2008).
87. Mottaghi, N, Seehra, M., Trappen, R, Kumari, S, Huang, C.-Y., Yousefi, S, Cabrera, G., Romero, A. & Holcomb, M. Insights into the magnetic dead layer in $La_{0.7}Sr_{0.3}MnO_3$ thin films from temperature, magnetic field and thickness dependence of their magnetization. *AIP Advances* **8,** 056319 (2018).
88. Kumari, S., Mottaghi, N., Huang, C.-Y., Trappen, R., Bhandari, G., Yousefi, S., Cabrera, G., Seehra, M. S. & Holcomb, M. B. Effects of oxygen modification on the structural and magnetic properties of highly epitaxial $La_{0.7}Sr_{0.3}MnO_3$ (LSMO) thin films. *Scientific Reports* **10,** 3659 (2020).
89. Wu, Y.-J., Hack, M., Wurster, K., Koch, S., Kleiner, R., Koelle, D., Mannhart, J. & Harbola, V. Vector substrate-based Josephson junctions. *Applied Physics Letters* **125,** 032601 (2024).
90. Dimos, D, Chaudhari, P & Mannhart, J. Superconducting transport properties of grain boundaries in $YBa_2Cu_3O_7$ bicrystals. *Physical Review B* **41,** 4038 (1990).
91. Hilgenkamp, H. & Mannhart, J. Grain boundaries in high-T_c superconductors. *Reviews of Modern Physics* **74,** 485 (2002).
92. Tafuri, F. *et al.* Recent achievements on the physics of high-T_c superconductor Josephson junctions: background, perspectives and inspiration. *Journal of superconductivity and novel magnetism* **26,** 21–41 (2013).
93. Kleiner, R. & Buckel, W. *Superconductivity: an introduction* (John Wiley & Sons, 2015).

94. Koelle, D, Kleiner, R, Ludwig, F, Dantsker, E & Clarke, J. High-transition-temperature superconducting quantum interference devices. *Reviews of Modern Physics* **71,** 631 (1999).
95. Mannhart, J. & Chaudhari, P. High-T_c bicrystal grain boundaries. *Physics today* **54,** 48–53 (2001).
96. José Martínez-Pérez, M. & Koelle, D. NanoSQUIDs: Basics & recent advances. *Physical Sciences Reviews* **2,** 20175001 (2017).
97. Tsuei, C., Kirtley, J. R., Chi, C., Yu-Jahnes, L. S., Gupta, A, Shaw, T, Sun, J. & Ketchen, M. Pairing Symmetry and Flux Quantization in a Tricrystal Superconducting Ring of $YBa_2Cu_3O_{7-\delta}$. *Physical Review Letters* **73,** 593 (1994).
98. Hilgenkamp, H., Mannhart, J. & Mayer, B. Implications of d x_2- y_2 symmetry and faceting for the transport properties of grain boundaries in high-T_c superconductors. *Physical Review B* **53,** 14586 (1996).
99. Palau, A, Puig, T, Obradors, X, Feenstra, R. & Gapud, A. A. Correlation between grain and grain-boundary critical current densities in ex situ coated conductors with variable $YBa_2Cu_3O_{7-\delta}$ layer thickness. *Applied physics letters* **88,** 122502 (2006).
100. MacManus-Driscoll, J. L. & Wimbush, S. C. Processing and application of high-temperature superconducting coated conductors. *Nature Reviews Materials* **6,** 587–604 (2021).
101. Stornaiuolo, D., Papari, G, Cennamo, N., Carillo, F., Longobardi, L, Massarotti, D., Barone, A & Tafuri, F. High quality factor HTS Josephson junctions on low loss substrates. *Superconductor Science and Technology* **24,** 045008 (2011).
102. Paskiewicz, D. M., Sichel-Tissot, R., Karapetrova, E., Stan, L. & Fong, D. D. Single-crystalline $SrRuO_3$ nanomembranes: a platform for flexible oxide electronics. *Nano letters* **16,** 534–542 (2016).
103. Singh, P., Swartz, A., Lu, D., Hong, S. S., Lee, K., Marshall, A. F., Nishio, K., Hikita, Y. & Hwang, H. Y. Large-area crystalline $BaSnO_3$ membranes with high electron mobilities. *ACS Applied Electronic Materials* **1,** 1269–1274 (2019).
104. Huang, J.-K. *et al.* High-κ perovskite membranes as insulators for two-dimensional transistors. *Nature* **605,** 262–267 (2022).
105. Sánchez-Santolino, G *et al.* A 2D ferroelectric vortex pattern in twisted $BaTiO_3$ freestanding layers. *Nature* **626,** 529–534 (2024).
106. Li, H. *et al.* Transition Metal-Oxide Nanomembranes Assembly by Direct Heteroepitaxial Growth. *Advanced Functional Materials* **34,** 2313236 (2024).
107. Carlson, A., Bowen, A. M., Huang, Y., Nuzzo, R. G. & Rogers, J. A. Transfer printing techniques for materials assembly and micro/nanodevice fabrication. *Advanced Materials* **24,** 5284–5318 (2012).
108. Wang, H., Harbola, V., Wu, Y.-J., van Aken, P. A. & Mannhart, J. Interface Design Beyond Epitaxy: Oxide Heterostructures Comprising Symmetry-forbidden Interfaces. *Advanced Materials* **36,** 2405065 (2024).
109. Dijkkamp, D, Venkatesan, T, Wu, X., Shaheen, S., Jisrawi, N, Min-Lee, Y., McLean, W. & Croft, M. Preparation of Y-Ba-Cu oxide superconductor thin films using pulsed laser evaporation from high T_c bulk material. *Applied Physics Letters* **51,** 619–621 (1987).
110. Stewart, W. Current-voltage characteristics of Josephson junctions. *Applied physics letters* **12,** 277–280 (1968).
111. McCumber, D. Effect of ac impedance on dc voltage-current characteristics of superconductor weak-link junctions. *Journal of Applied Physics* **39,** 3113–3118 (1968).

112. Vale, L. R., Ono, R. H., Talvacchio, J, Forrester, M., Hunt, B., Dilorio, M., Yang, K.-Y. & Yoshizumi, S. Long term stability of YBCO-based Josephson junctions. *IEEE transactions on applied superconductivity* **9,** 3382–3385 (1999).
113. Klushin, A., Golubov, A., Prusseit, W. & Kohlstedt, H. Comparative study of shunted bicrystal Josephson junctions. *Journal of Low Temperature Physics* **106,** 265–269 (1997).
114. Nagel, J *et al.* Resistively shunted $YBa_2Cu_3O_7$ grain boundary junctions and low-noise SQUIDs patterned by a focused ion beam down to 80 nm linewidth. *Superconductor Science and Technology* **24,** 015015 (2010).
115. Müller, B, Karrer, M, Limberger, F, Becker, M, Schröppel, B, Burkhardt, C., Kleiner, R, Goldobin, E & Koelle, D. Josephson junctions and squids created by focused helium-ion-beam irradiation of $YBa_2Cu_3O_7$. *Physical Review Applied* **11,** 044082 (2019).
116. Mannhart, J. & Schlom, D. G. Oxide interfaces—an opportunity for electronics. *Science* **327,** 1607–1611 (2010).
117. Chakhalian, J, Freeland, J., Habermeier, H.-U., Cristiani, G, Khaliullin, G, Van Veenendaal, M & Keimer, B. Orbital reconstruction and covalent bonding at an oxide interface. *Science* **318,** 1114–1117 (2007).
118. Goodge, B. H., Geisler, B., Lee, K., Osada, M., Wang, B. Y., Li, D., Hwang, H. Y., Pentcheva, R. & Kourkoutis, L. F. Resolving the polar interface of infinite-layer nickelate thin films. *Nature materials* **22,** 466–473 (2023).
119. Richter, C. *et al.* Interface superconductor with gap behaviour like a high-temperature superconductor. *Nature* **502,** 528–531 (2013).
120. Boschker, H. & Mannhart, J. Quantum-matter heterostructures. *Annual Review of Condensed Matter Physics* **8,** 145–164 (2017).
121. Zubko, P., Gariglio, S., Gabay, M., Ghosez, P. & Triscone, J.-M. Interface physics in complex oxide heterostructures. *Annual Review of Condensed Matter Physics* **2,** 141–165 (2011).
122. Liu, Y., Huang, Y. & Duan, X. Van der Waals integration before and beyond two-dimensional materials. *Nature* **567,** 323–333 (2019).
123. Cao, Y., Fatemi, V., Fang, S., Watanabe, K., Taniguchi, T., Kaxiras, E. & Jarillo-Herrero, P. Unconventional superconductivity in magic-angle graphene superlattices. *Nature* **556,** 43–50 (2018).
124. Novoselov, K. S., Mishchenko, A., Carvalho, A. & Castro Neto, A. 2D materials and van der Waals heterostructures. *Science* **353,** aac9439 (2016).
125. Behura, S. K., Miranda, A., Nayak, S., Johnson, K., Das, P. & Pradhan, N. R. Moiré physics in twisted van der Waals heterostructures of 2D materials. *Emergent Materials* **4,** 813–826 (2021).
126. Andrei, E. Y., Efetov, D. K., Jarillo-Herrero, P., MacDonald, A. H., Mak, K. F., Senthil, T, Tutuc, E., Yazdani, A. & Young, A. F. The marvels of moiré materials. *Nature Reviews Materials* **6,** 201–206 (2021).
127. Lu, X. *et al.* Superconductors, orbital magnets and correlated states in magic-angle bilayer graphene. *Nature* **574,** 653–657 (2019).
128. Sharpe, A. L., Fox, E. J., Barnard, A. W., Finney, J., Watanabe, K., Taniguchi, T., Kastner, M. & Goldhaber-Gordon, D. Emergent ferromagnetism near three-quarters filling in twisted bilayer graphene. *Science* **365,** 605–608 (2019).
129. Weston, A. *et al.* Interfacial ferroelectricity in marginally twisted 2D semiconductors. *Nature nanotechnology* **17,** 390–395 (2022).
130. Yu, Y., Ma, L., Cai, P., Zhong, R., Ye, C., Shen, J., Gu, G. D., Chen, X. H. & Zhang, Y. High-temperature superconductivity in monolayer $Bi_2Sr_2CaCu_2O_{8+\delta}$. *Nature* **575,** 156–163 (2019).

131. Zhao, S. F. *et al.* Time-reversal symmetry breaking superconductivity between twisted cuprate superconductors. *Science* **382,** 1422–1427 (2023).
132. Zhang, J. *et al.* Super-tetragonal $Sr_4Al_2O_7$ as a sacrificial layer for high-integrity freestanding oxide membranes. *Science* **383,** 388–394 (2024).
133. Han, L., Dong, G., Liu, M. & Nie, Y. Freestanding perovskite oxide membranes: a new playground for novel ferroic properties and applications. *Advanced Functional Materials* **34,** 2309543 (2024).
134. Lu, Q. *et al.* Engineering magnetic anisotropy and emergent multidirectional soft ferromagnetism in ultrathin freestanding $LaMnO_3$ films. *ACS nano* **16,** 7580–7588 (2022).
135. Nian, L. *et al.* $Sr_4Al_2O_7$: A new sacrificial layer with high water dissolution rate for the synthesis of freestanding oxide membranes. *Advanced Materials* **36,** 2307682 (2024).
136. Yoon, H. *et al.* Freestanding epitaxial $SrTiO_3$ nanomembranes via remote epitaxy using hybrid molecular beam epitaxy. *Science Advances* **8,** eadd5328 (2022).
137. Xu, S. *et al.* Magnetoelectric coupling in multiferroics probed by optical second harmonic generation. *Nature communications* **14,** 2274 (2023).
138. Ji, J. *et al.* Heterogeneous integration of high-k complex-oxide gate dielectrics on wide band-gap high-electron-mobility transistors. *Communications Engineering* **3,** 15 (2024).
139. Pryds, N, Park, D.-S., Jespersen, T. & Yun, S. Twisted oxide membranes: A perspective. *APL Materials* **12,** 010901 (2024).
140. Shen, J., Dong, Z., Qi, M., Zhang, Y., Zhu, C., Wu, Z. & Li, D. Observation of moiré patterns in twisted stacks of bilayer perovskite oxide nanomembranes with various lattice symmetries. *ACS applied materials & interfaces* **14,** 50386–50392 (2022).
141. Nakagawa, N., Hwang, H. Y. & Muller, D. A. Why some interfaces cannot be sharp. *Nature materials* **5,** 204–209 (2006).
142. Ohtomo, A., Muller, D., Grazul, J. & Hwang, H. Y. Artificial charge-modulationin atomic-scale perovskite titanate superlattices. *nature* **419,** 378–380 (2002).
143. Tomita, K., Miyata, T., Olovsson, W. & Mizoguchi, T. Strong excitonic interactions in the oxygen K-edge of perovskite oxides. *Ultramicroscopy* **178,** 105–111 (2017).
144. Wei, J., Ogawa, T., Feng, B., Yokoi, T., Ishikawa, R., Kuwabara, A., Matsunaga, K., Shibata, N. & Ikuhara, Y. Direct measurement of electronic band structures at oxide grain boundaries. *Nano letters* **20,** 2530–2536 (2020).
145. Wu, M. *et al.* Engineering of atomic-scale flexoelectricity at grain boundaries. *Nature communications* **13,** 216 (2022).
146. Fitting, L, Thiel, S., Schmehl, A., Mannhart, J. & Muller, D. A. Subtleties in ADF imaging and spatially resolved EELS: A case study of low-angle twist boundaries in $SrTiO_3$. *Ultramicroscopy* **106,** 1053–1061 (2006).
147. Jennings, D., Ebert, J. N., Du, H., Ma, Q., Schafer, L.-A., Sebold, D., Mayer, J. & Rheinheimer, W. The formation of stacking faults in barium zirconate-type perovskites. *Chemistry of Materials* **35,** 8382–8396 (2023).
148. Muller, D., Kourkoutis, L. F., Murfitt, M., Song, J., Hwang, H., Silcox, J., Dellby, N. & Krivanek, O. Atomic-scale chemical imaging of composition and bonding by aberration-corrected microscopy. *Science* **319,** 1073–1076 (2008).
149. Abrahams, S., Kurtz, S. & Jamieson, P. Atomic displacement relationship to Curie temperature and spontaneous polarization in displacive ferroelectrics. *Physical Review* **172,** 551 (1968).